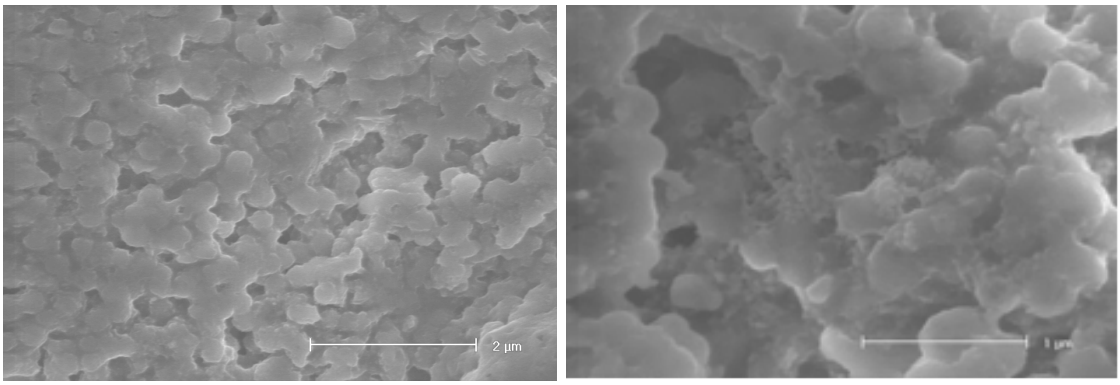

(a) (b)

Figure 3.22: SEM images of the CdTe NC assembly surface showing coagulations by organic ligands.

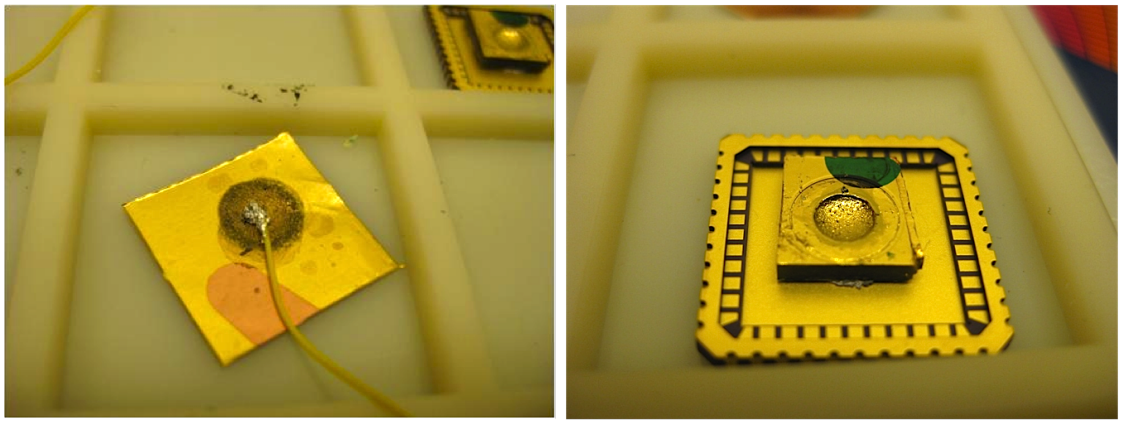

(a) (b)

Figure 3.23: PbSe NC assembly deposited by drop-casting method on (a) copper foil and (b) PCB based substrate. Noticeably, both samples were covered by a gold contact on the top of the assembly.

an SEM, as shown in Fig. 3.24. Fig. 3.24(a) and (b) shows features in the relatively low magnification, such as macroscopic crumbs, blobs and uneven surface features. Fig. 3.24(c) and (d) shows the surface morphology in the intermediate magnification, featuring internal cracks and surface textures on each lump, and Fig. 3.24(e) and (f) show coagulations of PbSe NCs consisting of lumps as shown in the previous cases; as in the CdTe case, the particles are enclosed by organic materials as desired and coagulated into nodules, as expected given the deposition procedure, though not ultimately desired in a uniform charge-transport device.

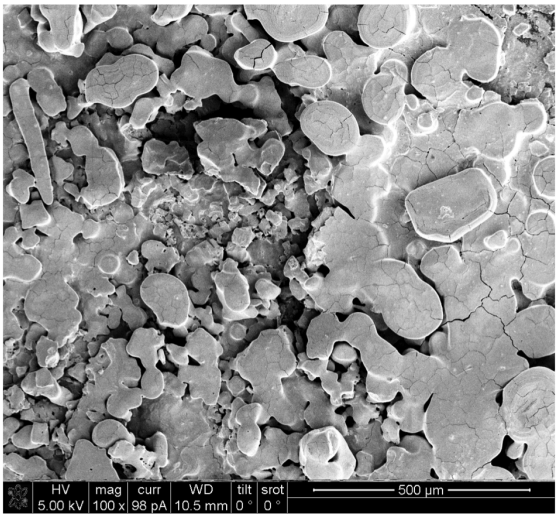
HV
5.00 kV
mag
100 x
curr
98 pA
WD
10.5 mm
tilt
0 °
srot
0 °
500 µm

(a)

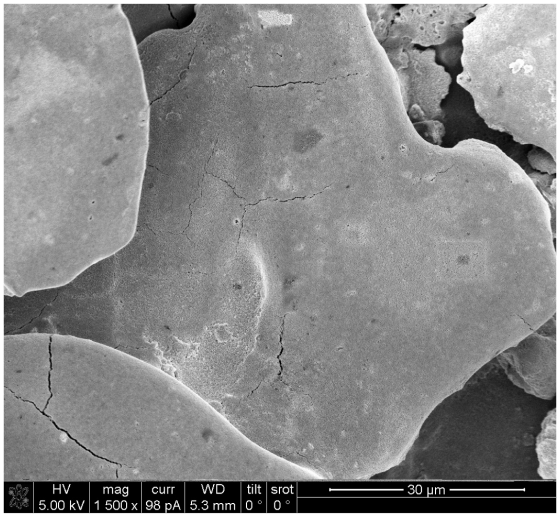
HV
5.00 kV
mag
1 500 x
curr
98 pA
WD
5.3 mm
tilt
0 °
srot
0 °
30 µm

(b)

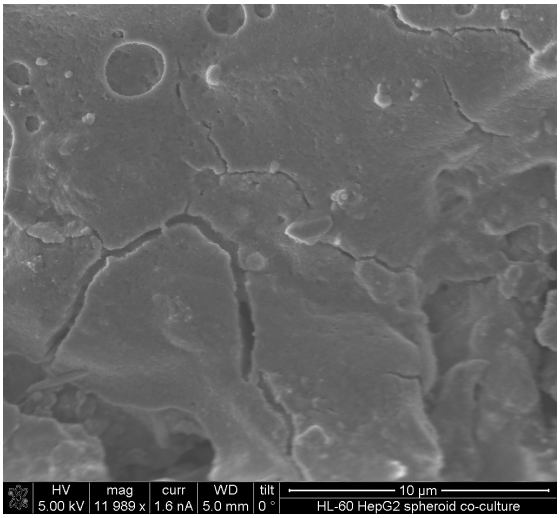
HV
5.00 kV
mag
11 989 x
curr
1.6 nA
WD
5.0 mm
tilt
0 °
10 µm
HL-60 HepG2 spheroid co-culture

(c)

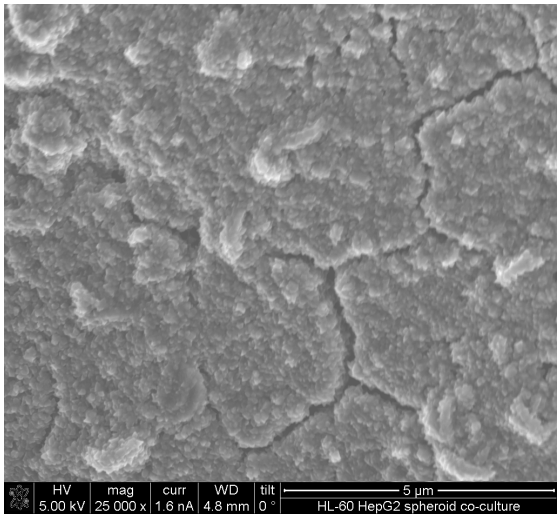
HV
5.00 kV
mag
25 000 x
curr
1.6 nA
WD
4.8 mm
tilt
0 °
5 µm
HL-60 HepG2 spheroid co-culture

(d)

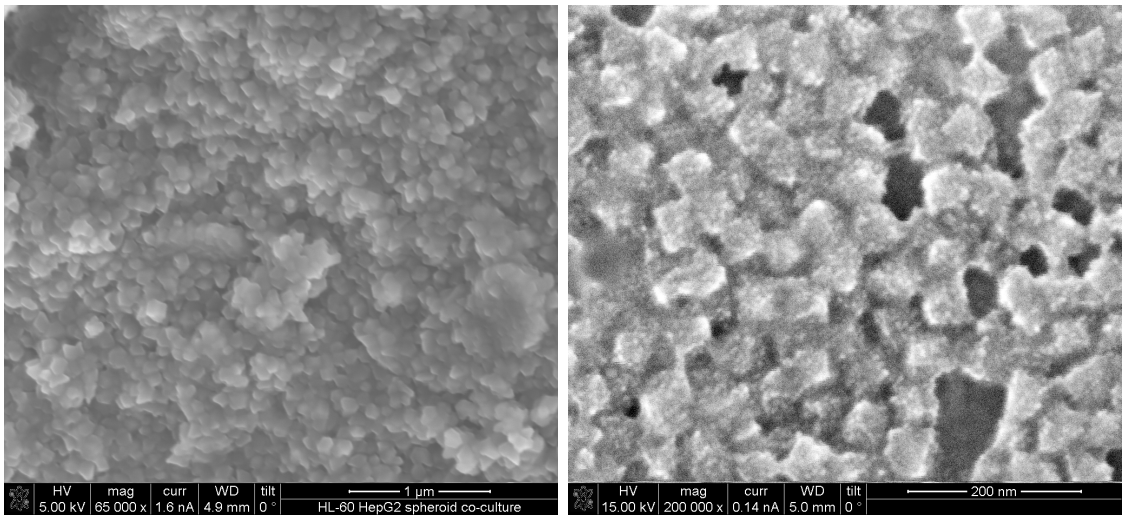

(e) (f)

Figure 3.24: SEM images of the PbSe NC assembly surface in (a), (b) low, (c), (d) intermediate and (e), (f) high magnification. The cracked and stacked dried mud-puddle look of the NC assembly at various scales.

Poor surface properties and internal cracks of the NC assembly can significantly hamper charge carrier transport by providing potential barriers and trapping sites as illustrated in Fig. 3.25. Cracks are usually formed due to the rapid evaporation of the volatile solvent: in these cases, we used chloroform. Note that the stacking fault propagates through the layers as the self-assembly preferentially adds to existing NCs. One may use less volatile solvents for NC particle dispersions in order to reduce the crack formation; however, this results in longer drying times which we avoided at this research stage in which a multitude of drop-casts are used in order to form a solid of sufficient thickness. Comparing Fig. 3.24(c) and (d), one can tell from the texture of the surface that an assembly composed of smaller NCs; Fig. 3.24(c) exhibits a much smoother surface morphology. Aside from the physics motivations, one other advantage of using small particle sizes is that the organic coagulation between domains of NCs is reduced and the assembly surface is smoother and thus more amenable to adhesion with an evaporated or sputtered metal contact. Note however, that large-scale domains and cracks remain for even the small samples.

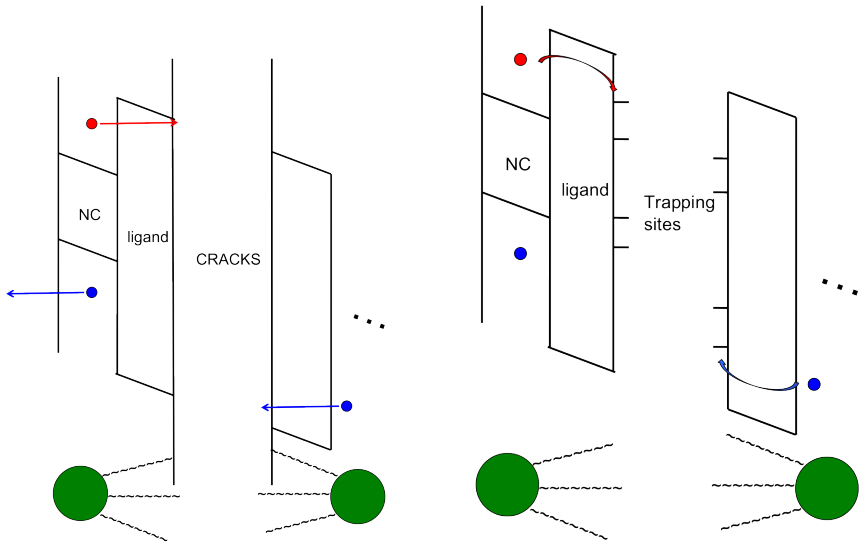

Figure 3.25: Illustration of charge carrier transport in the NC assembly, hampered by (a) excess ligands providing trapping sites and (b) cracks providing potential barriers for the carrier transport.

3.3.2 Layer-by-Layer Method

The LBL method is a well-known method for efficiently depositing NC colloidal dispersions into high quality and stable thin-film layers on the substrate, while preserving the distinctive optoelectrical and magnetic properties of the size-quantized states of the NCs. A broad definition of LBL would even include drop-casting repetitively in order to stack possibly-inconsistent layers each time; however, I will restrict the definition of LBL in this dissertation to mean the repetitive stacking of "consistent" layers of NC assembly, which involves a rinsing procedure between every repetition. In this dissertation, the LBL method is utilized mainly in the following two approaches: a) CdTe NC/PDDA bilayer assembly and b) PbS NC assembly with ligand exchange treatment with 1,2-Ethanedithiol (EDT) and hydrazine.

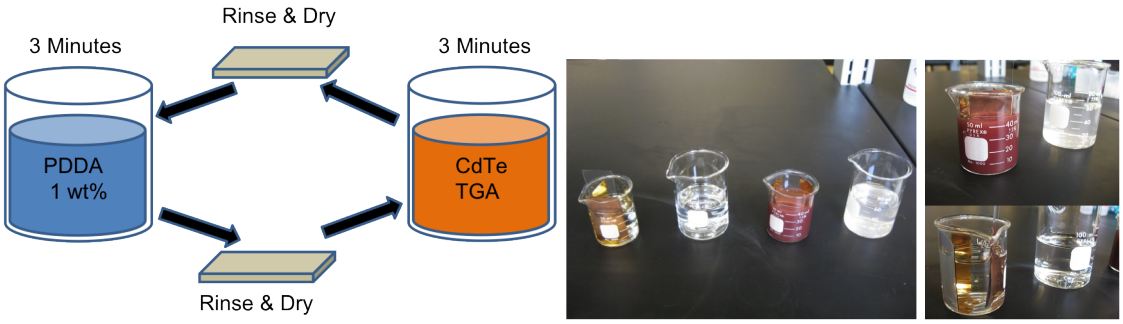

(a) (b)

Figure 3.26: SEM images of the PbSe NC assembly surface in (a) low magnification and (b) high magnification.

3.3.2.1 CdTe NC/PDDA Bi-layer Deposition

As previously mentioned (3.1.1.1), CdTe NCs exhibit slightly negative charges due to the –OH and –COOH ligands from the thioglycolic-acid (TGA) [88]. The LBL deposition of CdTe NC exploits the adsorbing nature of oppositely charged molecules. In this procedure, poly(diallyl dimethyl ammonium chloride) (PDDA), was induced as a polycation used for adsorbing nanoparticles, and the TGA-stabilized CdTe nanocrystal solution was spread on the PDDA layer and adsorbed. By an alternatively adsorbing procedure, a bilayer consisting of a polymer/nanocrystal composite was developed on metal-evaporated silicon or glass substrate by dip-coating and spin-casting, as schematically shown in Figs. 3.26 and 3.27, respectively.

Fig. 3.27(b) and (c) shows an example of the LBL method sample, on which alternating layers of CdTe NC and PDDA were spun-cast. The sample was based on a 4″ silicon wafer, on which Au was evaporated. The varying color reflects the non-uniform thickness deposited towards the outside of the wafer. A total of 30–58 bilayers of CdTe/PDDA composite layer were deposited on the substrate. If the uniform, inner-section of the assembly is diced and bounded by metallic electrodes, then 1×1 cm^2 detectors can be realized, as shown in Fig. 3.27(c).

In order to determine the thickness of the resulting NC assembly, the cross-section

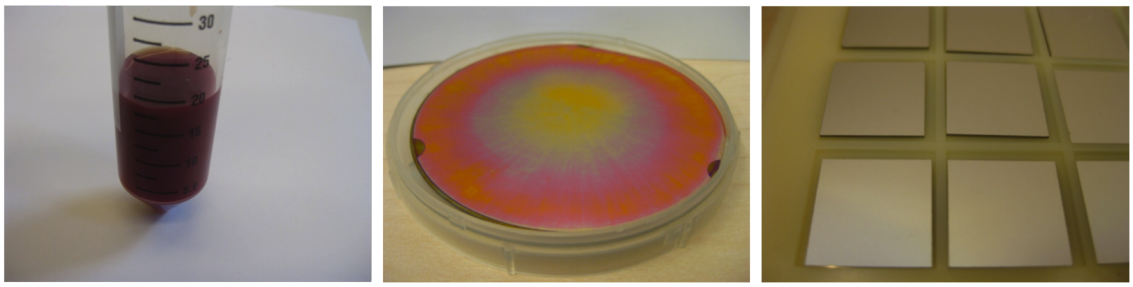

(a) (b) (c)

Figure 3.27: Schematic of LBL deposition of CdTe NC assembly by spin-casting: (a) CdTe NC dispersion stabilized with TGA, (b) CdTe NC assembly of 48 bilayers (CdTe NC/PDDA) deposited by spinning LBL method on gold-evaporated silicon wafer substrate. (c) 48 bilayer CdTe NC assembly samples sandwiched by gold and indium metal contact.

of the layer was examined by an SEM with auxiliary x-ray energy dispersive spectroscopy (EDS) to identify the constituent layers, an example of which is shown in Fig. 3.28. The CdTe NC/PDDA composite sample was formed on the aluminum evaporated silicon wafer, by repeating the spin-cast bilayer deposition procedure for 58 times. Note that the characteristic x-rays from Al_K, Si_K and Pt_L are similar in energy, but a careful examination of the various structures reveals that the layer is $\sim$250 nm thick (Fig. 3.29), achieved after 58 cycles of the LBL process was repeated.

Unfortunately, in order to stop the high-energy charged particles associated with ionizing radiation one desires a thickness of at least 10's of micrometers, as it was shown from the PENELOPE simulation (2.3.1), if not several centimeters, which requires repetitive and lengthy casting procedures; for instance, roughly 80 hours of aqueous layer-by-layer deposition is required to achieve 10's of micrometers thickness. This can be enabled by robotic dipping tools, but the quality is not highly controlled even in the automated process. For characterization studies, one can utilize sub-micrometer layers to evaluate the material.

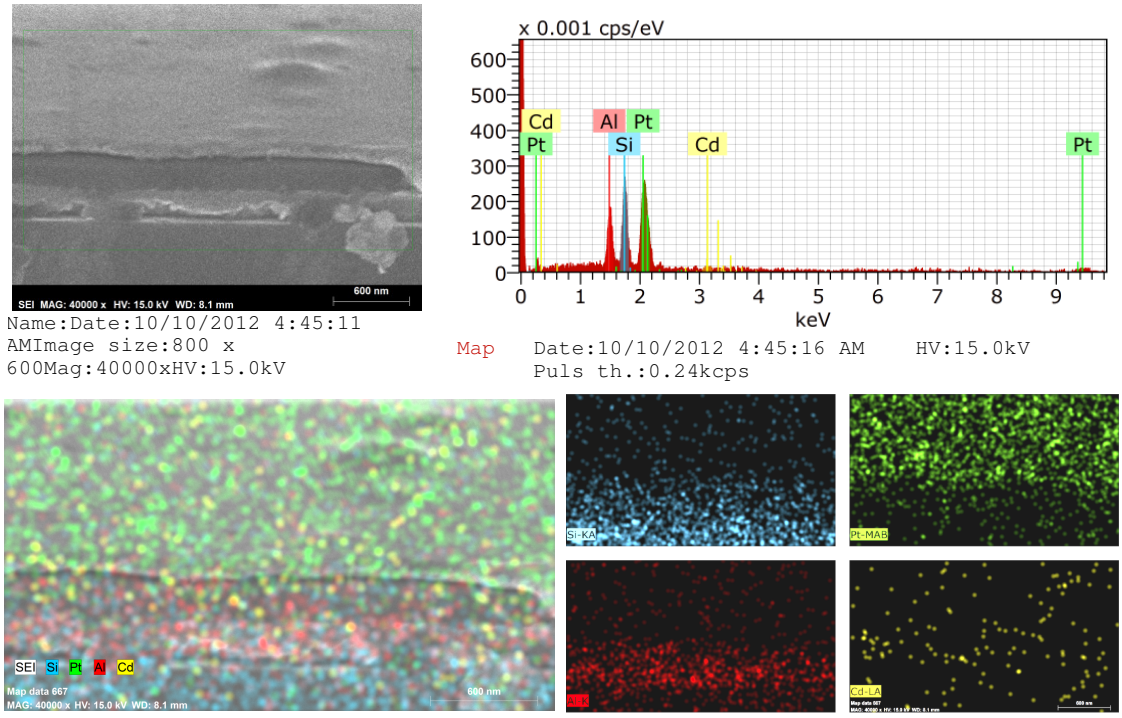

Figure 3.28: EDS analysis on the cross-sectional view of the LBL deposited CdTe NC assembly sandwiched between Al and Pt electrodes on silicon wafer.

3.3.2.2 Ligand Exchange Treatments on the NC Assembly

One option for accomplishing enhanced charge conductivity within the NC assembly is to replace the oleic groups with a more suitable coordinating molecule, in the form of either a conducting polymer or a molecule that is sufficiently small that hopping transport over the closer distance and mini-band formation result in de-localization of the charge wave-functions throughout the lattice, of which the former approach will be discussed later in the next section (3.3.3). Recently, there have been many studies reporting on the efficient charge collection behavior of lead salt NC-based photovoltaic devices with chemical treatment, notably EDT and hydrazine [11, 13, 18, 22, 23, 104, 105]. These chemical treatments are known to enhance the charge transport properties of the NC assembly by substituting the long chain OA ligands with shorter chain ligands, as shown in the schematic in Figs. 3.30 and 3.31. Therefore, high mobilities can be realized via charge delocalization.

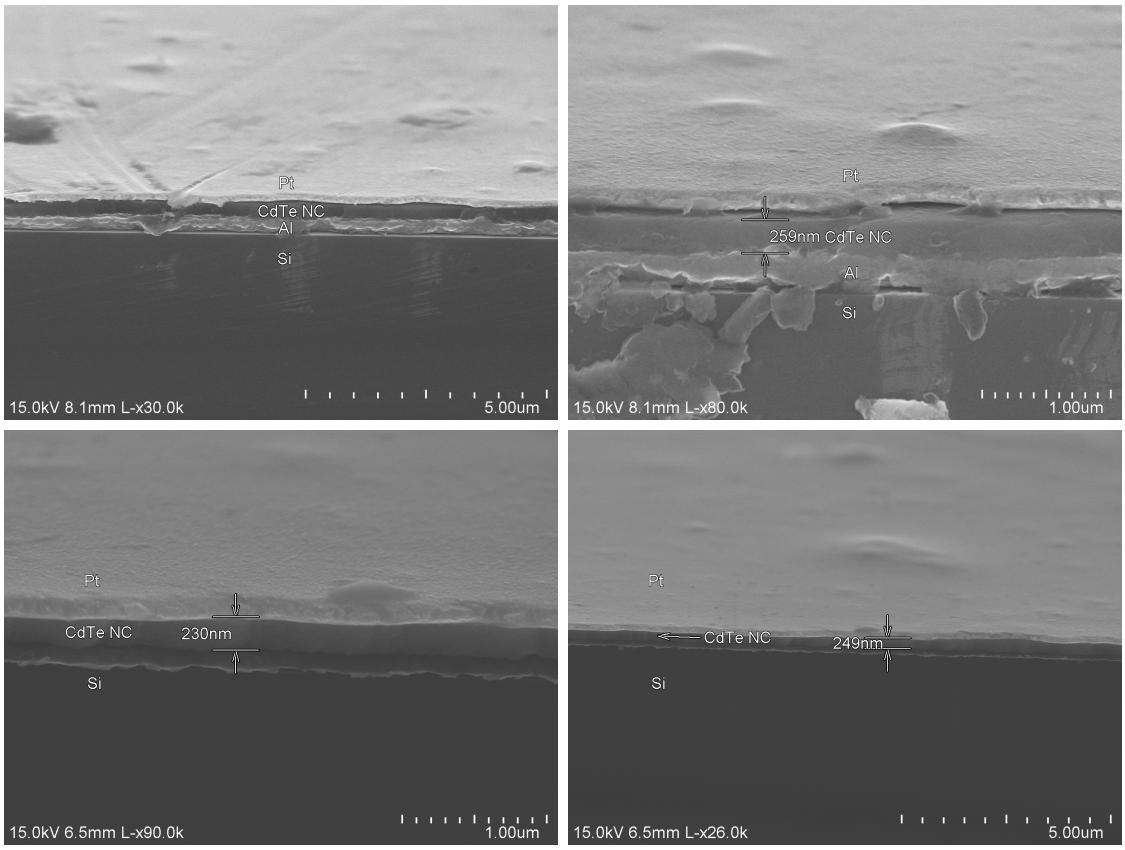

Figure 3.29: Cross-sectional view of the LBL deposited CdTe NC assembly sandwiched between Al and Pt electrodes on silicon wafer, investigated at various locations.

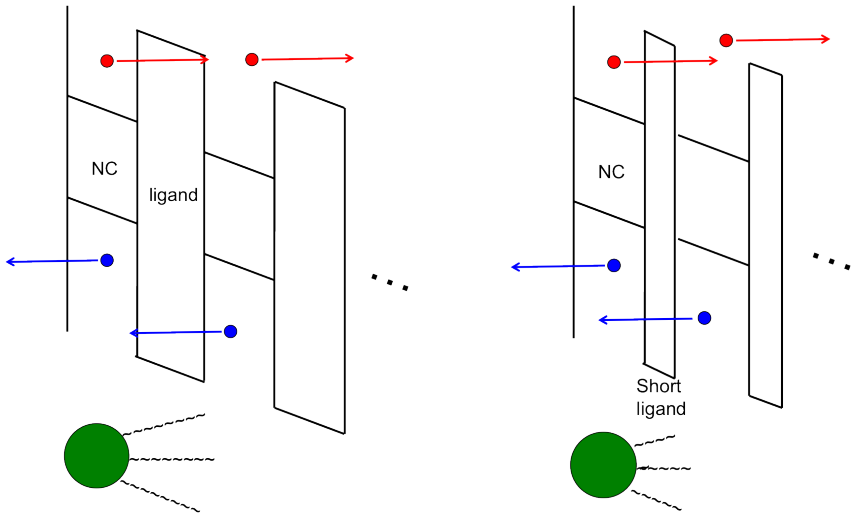

(a) (b)

Figure 3.30: Schematic of charge carrier transport enhancement in NC assemblies from (a) to (b), promoted by the capping-ligand exchange treatment.

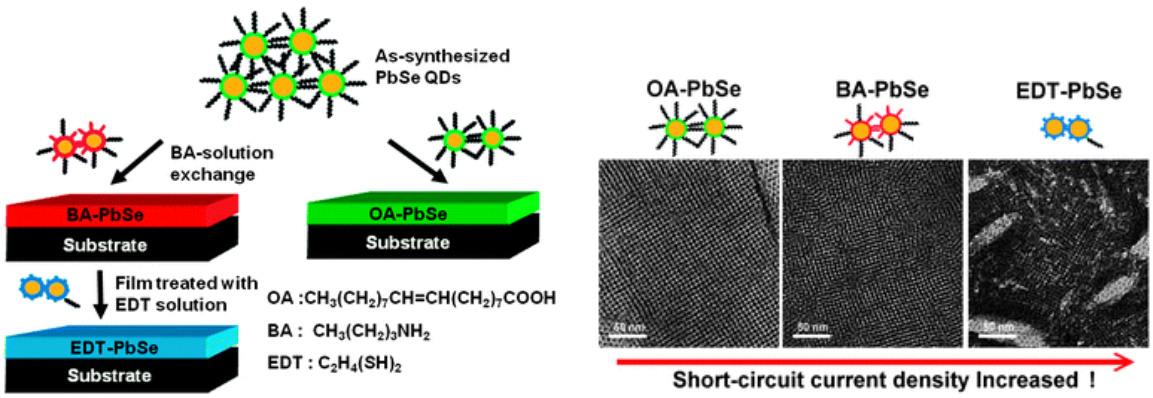

Figure 3.31: Schematic of fabricating PbSe NC assembly thin films incorporating various ligands – OA, BA and EDT [105].

EDT or hydrazine treatments are usually preceded by another ligand exchanging process inducing butylamine (BA) to remove a portion of the OA ligand first. The replacing mechanism was previously studied by J. J. Choi *et al.* and C.-Y. Kuo *et al.* [103, 105]. The colloidal NC dispersions as-synthesized (and purified) are re-dispersed in anhydrous BA solution (or mixed with the previous solvent if one wants to prevent abrupt change – this way, the amount of replacement as a result will be decreased) stirred vigorously for 48 h or more in a N_2-filled glove box. The ligand-exchanged NC dispersion then goes through another clean-up process: NCs are re-precipitated with polar solvent (namely, anhydrous isopropanol, acetone, or mixture of them), dried, and re-dispersed in anhydrous solvent (hexane, octane, toluene, or chloroform).

The ligand exchange treatments can be combined with dip-coating, drop, slide, and spin-cast processes to deposit a NC assembly layer by layer, without introducing interstitial conjugate polymers. After deposition of one NC layer of which the ligand was partially substituted with BA previously, one can treat the assembly with 0.1 M EDT or 1 M hydrazine dissolved in an immiscible solvent (acetonitrile and dichlorobenzene are popularly used), by dipping or spreading the solution on the assembly followed by a rinsing process. By repeating this procedure, one can develop chemically treated NC assemblies on the substrate layer by layer [102–104].

Even in this procedure, drop-cast samples often produce very poor quality films. Cracks becomes an even more serious problem when EDT treatments are performed and when large amounts of NCs are deposited – making thick assemblies by drop-casting. The reason is expected because the EDT process replaces the existing inter-particle ligands with shorter ones, leaving a void in the assembly as the solvent evaporates. Therefore, coagulations of NC assemblies will contract into non-uniform domains characterized by a number of cracks. Fig. 3.32 shows SEM images of a PbS NC assembly drop-cast 20 times, treated with 0.1 M EDT between each repetition. A number of cracks, crumbs and peel-offs can be observed, each with a dimension-scale of tens or hundreds of micrometers. In this configuration, *a priori*, it is very challenging to: a) make a good electrical contact with that region, and b) acquire consistent responses from the assembly over the macroscopic area as the I-V curves of the assembly present a variety of responses depending on the area that is investigated.

In order to mitigate the poor film quality issue of the ligand exchanged LBL NC assembly, spin-coating, dip-coating and slide-casting methods are preferred. The spin-coating method has been widely attempted by many previous researchers and is known to be moderately successful in developing a few hundred nanometer thick assembly; however, we would like to develop a much thicker assembly (hundreds of micrometers). Spin-coating the NC dispersion for thousands of times wastes much more of the solution, time and efforts than other methods. Therefore, a slide-casting method was studied in this research. The advantage of utilizing the slide-casting method is that: a) one does not need to waste as much solution as needed for the spin-coating, and b) one expects a much thicker layer of NC assembly per repetition, compared with the spin-coating or dip-coating method. Fig 3.33 shows the slide-cast PbS NC assembly, with EDT treatment between each repetition, deposited 10 times. It was then followed by 10 repetitions of the hydrazine treatment based on the expectation that hydrazine treatment will produce an n-type NC assembly [18];

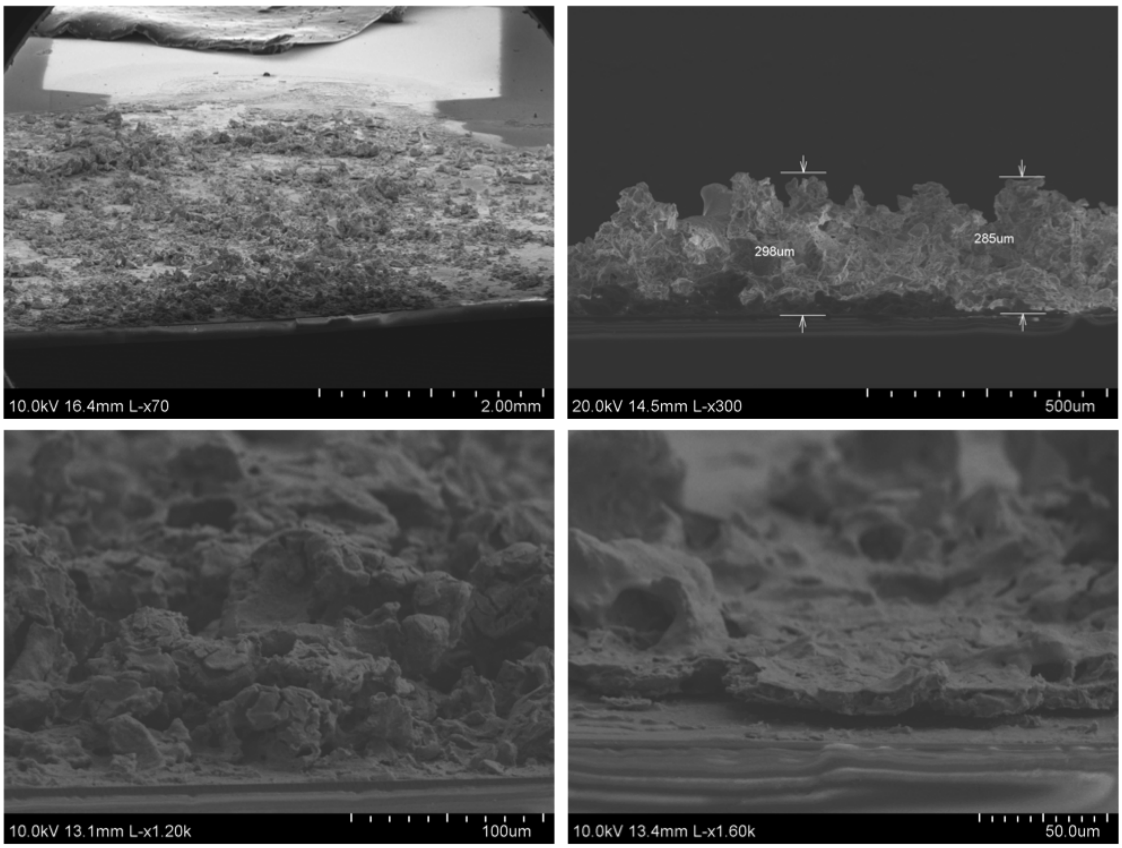

Figure 3.32: SEM images of PbS NC assembly deposited by *drop-casting* method. The surface property was represented by a large number of cracks and crumbs. The thickness of film was also irregular.

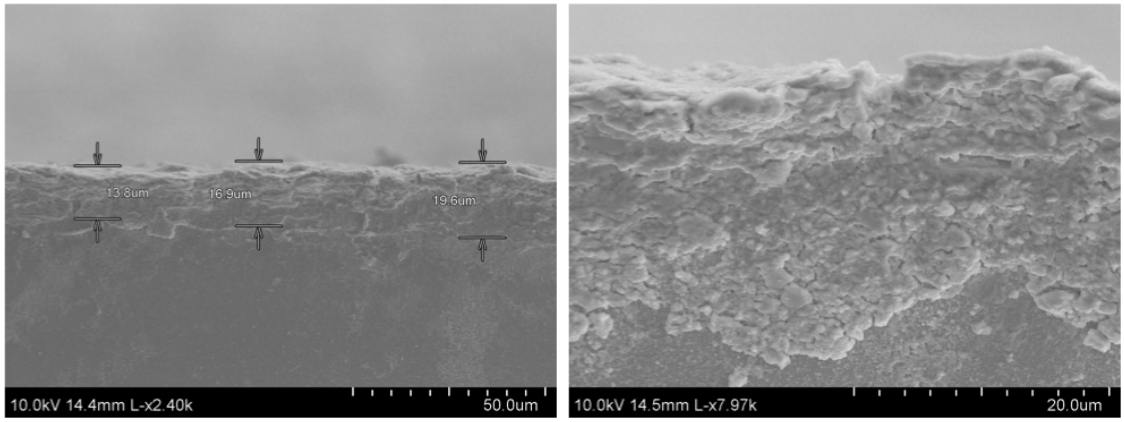

Figure 3.33: SEM images of PbS NC assembly deposited by dip-coating method by 20 times with 10 layers of EDT treatment and 10 layers of hydrazine treatment.

thus, this sample could be an p-n type structure.

In order to efficiently use the NC dispersion, the dip-coating method was also attempted. The dip-coating method has been also reported to be successful as well in the fabrication of ∼100 nm solar cell fabrication [13]. We have repeated the dip-coating LBL process for 150 times, and it deposits a good quality film during the first few dozen iterations. However, as one repeats the procedure, the quality of the film deposited worsened noticeably, developing more cracks and crumbs on the surface, as the procedure was repeated. Considering that the deposition process is balanced by the gravity and the adsorbing nature of small particles that have large surface area, at some point, small pieces often start fall off the surface. Thus, even though dip-coating usually deposits uniform layers over a large area, there still can be some inhomogeneities; minor cracks, for instance. In addition, the NC assembly after the dip-coating is susceptible to re-dissolving during subsequent coats. Furthermore, although minor cracks can be filled, as one repeats the dip-coating process, they sometimes worsen as the solvent can etch part of the NC assembly. This effect is not visually noticeable as long as the repetition is within, ∼50 times; however, higher multiplicities makes the inhomogeneity more significant. The resulting cracks can give rise to heavy crumbs that can fall from the NC assembly, and be etched by the solvent.

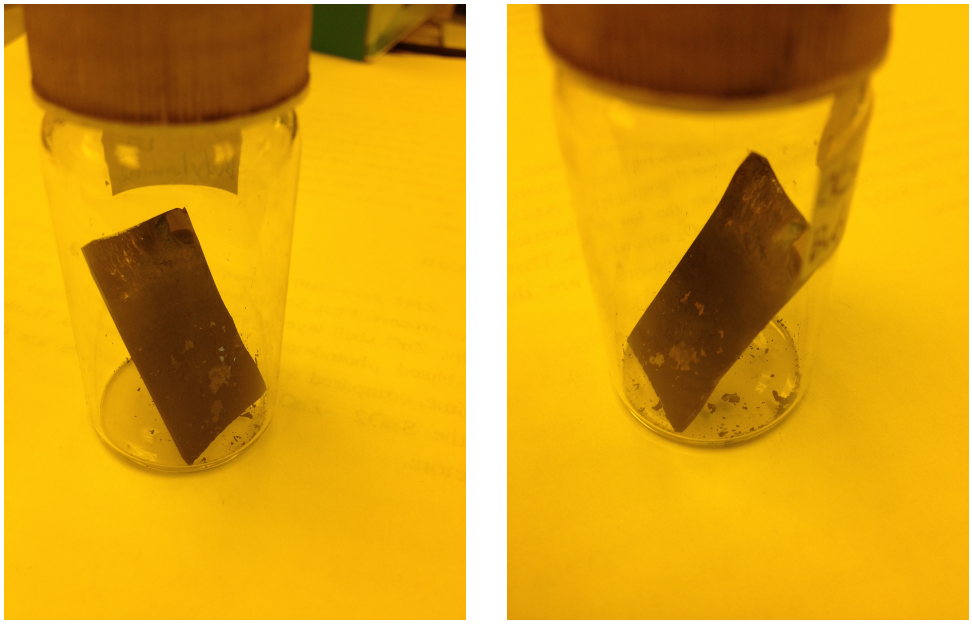

(a) (b)

Figure 3.34: Dip-coated PbS assembly with EDT treatment repeated for 150 times. Note that the surface state worsens and cracks fallen off to the bottom of the vial as time goes by: from (a) to (b).

Fig. 3.34 shows an example of the dip-coated NC assembly which was repeated for 150 times, however, the quality of the film was poor – one can see a number of crumbs fallen from the area on the bottom of the vial. The coarse samples are not conducive to metal-contact deposition as the assembly separates from the substrate when high vacuum is applied – residual solvents quickly evaporate, and cracking worsens – and the adhesion from the NC assembly to the substrate cannot stand the weight of the assembly with heavy metal deposited.

3.3.3 Blended Assembly of NC/Polymer Composite

As will be discussed in the next section (IV), more-than-10 μm-thick NC assemblies created by various methods have encountered inevitable but very substantial challenges in charge carrier transport properties; and this significantly compromises their viability as an ionizing radiation detector. Amongst many type of efforts to enhance the charge transport properties, blended composite structure approaches for

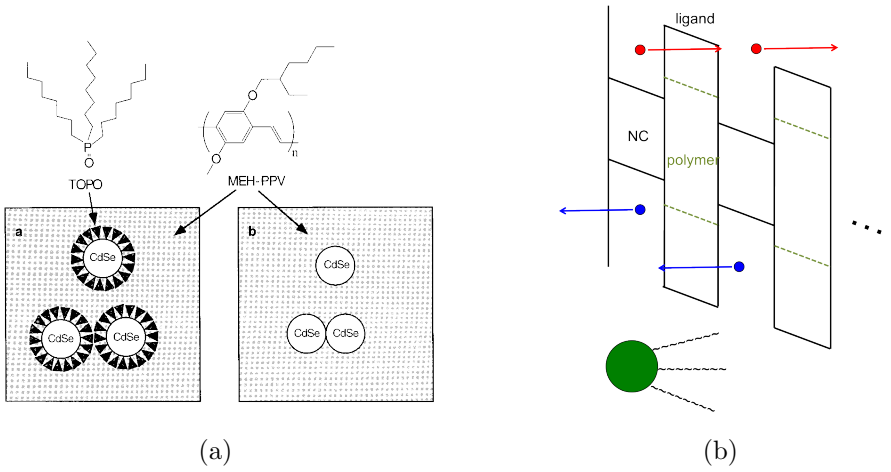

(a) (b)

Figure 3.35: Configuration and charge carrier transport of the NC assembly in a blended composite structure: an example of TOPO-capped CdSe. NCs can exist in the blended structure either with or without surface ligands around the particle.

the NC assembly have been attempted vigorously throughout many previous studies [17, 22, 23]. Configurations of the blended composite assembly of NCs and conductive polymers are illustrated in Fig. 3.35. Advantages one can take by introducing conjugated polymers blended with NC assembly involve ease of processing, low cost, and physical flexibility in large area coverage. Organic/NC composite approaches have been demonstrated to produce efficient optoelectronic devices operating in the visible light and IR region, especially related to photovoltaic applications – solar cells and photodiodes, and light harvesting devices, representatively, LEDs [19, 106–108].

In these approaches, the selection of the suitable semiconducting polymer is critical in achieving efficient charge separation and transport between the NCs and polymers. Conjugated (semiconducting) polymers are typically used as a hole transporting agent, due to the relatively high hole mobility compared to the electron mobility. Thus, it is important to provide a good band alignment which allows an efficient hole transfer process between the NC and polymer. That is, the ionization potential of the polymer should, ideally, lie closer to vacuum than that of the NC. However, the ionization potential of the bulk PbSe is ∼4.75 eV, and hole conducting polymers typ-

ically have ionization potentials ∼5.1 eV or above [109]. The low ionization potential of PbSe as bulk is not so favorable for providing a suitable energy band alignment with type-II heterojunction needed for efficient for charge separation and conduction. This issue can be overcome by attempting: a) NC approaches in which the energy band gap is substantially spread, and b) high voltage bias applied on both side of the assembly which can smoothen out the potential barriers between the NCs and polymers. Among many kinds of conductive polymers, MEH-PPV (Poly[2-methoxy-5-(2-ethylhexyloxy)-1,4-phenylenevinylene]) is known to have a relatively low ionization potential around ∼5 eV [17]. If one uses a PbSe NC which has energy band gap of 0.7 eV, one could align the energy bands favorably for hole conduction.

Thus, in order to realize suitable charge transport, the PbSe NC solution is mixed with a conductive polymer, for instance, para-MEH-PPV (poly[(p-phenylenevinylene)-alt-(2-methoxy-5-(2-ethylhexyloxy)-p-phenylenevinylene)]), which is used as a hole transporting agent. Although drop-, dip-, and spin casting can each be employed to produce responsive detectors, we attempted to achieve greater device reproducibility via slow (60, 90, 150 rpm) spin-casting, in which the PbSe NC solution is mixed with the para-MEH-PPV.

Depending on the batch of the solution, the concentration of the conductive polymer in the composite solution was varied from 1–3 weight percent of the overall solution. For instance, for the detector comprised of star-shaped particles, 30 mg of para-MEH-PPV was dissolved in 1 ml of chloroform, which was combined with 1 ml of the PbSe dispersed in chloroform, from which the colloidal solids were cast. As shown in Fig. 3.36, as the relative concentration of PbSe increases, the solids change from yellow to black. Greater polymer concentrations formed a brighter, more yellow assembly, whereas the pure PbSe NC assembly exhibits a dark assembly. In addition, the composite solution with a greater percentage of MEH-PPV covered the substrate more readily and took less time to dry than the PbSe NC only solutions or composite

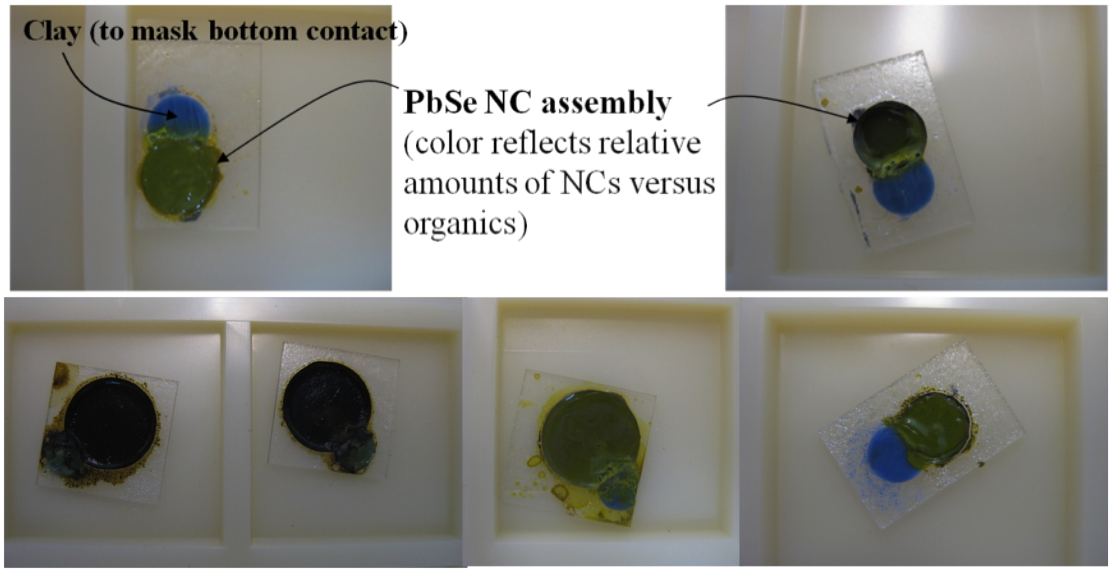

Figure 3.36: PbSe NC/MEH-PPH composite assembly deposited on the glass substrate. PbSe NC/MEH-PPV composite assembly samples before top metal contact deposition, left two samples, notably contains less concentration of MEH-PPV.

solutions with less MEH-PPV concentration. The molds from the thinner silicon and glass substrates were formed using wet and dry etching techniques of which procedure is explained in Appendix B. Fig. 3.37 shows the assemblies deposited into 5 mm deep holes with 15 mm diameters milled into plastic substrates, and the detectors therefore form active depths that are a few millimeters thick.

If the array is close-packed, then the length of the interstitial space separated by the monomer is only 0.67 nm, compared with a typical 5 nm diameter NC, as shown in Fig. 3.38. It would be ideal if the packing structure of PbSe NCs conjugated with conductive polymer is closely-packed, with the highest packing fraction achievable. The consequence of this is that most of secondary-energy loss is in the PbSe, as desired, so that the energy conversion process can be controlled by the geometry. Specifically, the energy loss of an (gamma-ray induced) electron moving through the PbSe in the a unit cell is 96 times that of the energy loss in the MEH-PPV. Furthermore, the energy in the PPV isn't lost, but rather gets converted into electron-hole pairs via its band-gap (2.6 eV). Thus, the material has attractive qualities in the charge transport

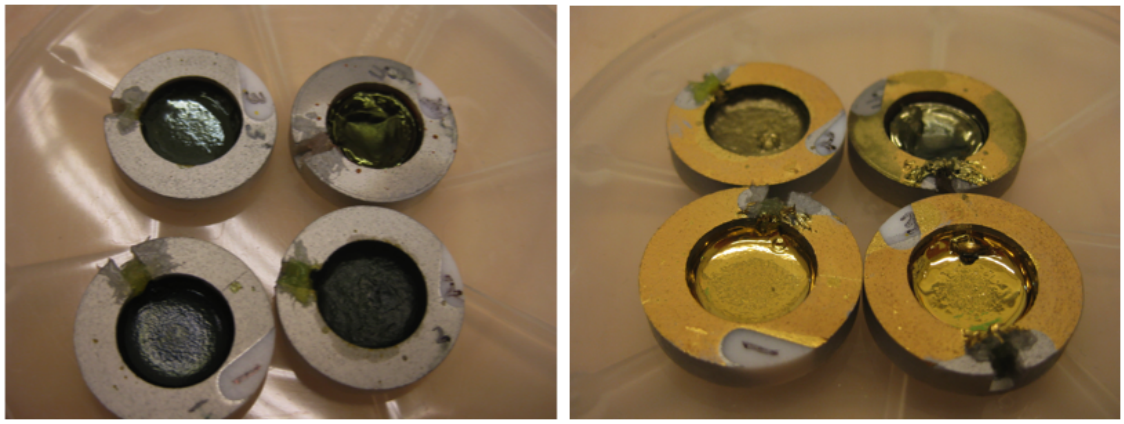

(a) (b)

Figure 3.37: PbSe NC/MEH-PPH composite assembly deposited on plastic substrates, (a) before the top metal contact is formed and (b) after gold contact evaporation.

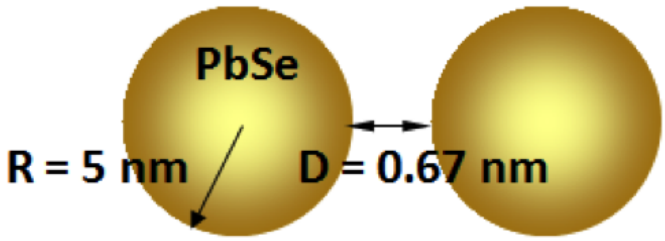

Figure 3.38: Typical geometry configuration for a PbSe quantum dot separated by a single link of the MEH-PPV polymer chain.

without substantially impairing the charge conversion. However, the geometry of the solid deviates from a perfect face centered cubic (FCC) structure to a degree depending on the size dispersion of the colloidal solution; nevertheless, the reduction in densities between the single-crystal lead chalcogenides and the nanocrystalline forms reflects the values that are achieved when the ordering and spacing are optimized for spherical NCs. As will be discussed in Appendix A, Monte Carlo simulations on the radiation response from the PbSe NC/MEH-PPH composite assembly show that, even in nanocrystalline form, the lead chalcogenides maximize the probability of interacting with impinging high-energy photons, and more generally, they exhibit superior characteristics for the efficient stopping of primary or secondary charged particles.

3.3.4 CdTe NW Assembly

The solution of CdTe NWs was filtered through 200 nm-pore membrane paper using vacuum filtration. The ease of deposition in the vacuum filtration method enables one to take advantage of macroscopic assembly formation via the vacuum filtration method. The vacuum was applied for 48 hours, and the sample took approximately 3 subsequent days to fully dry. The resulting film was intact and peeled off from the filter as shown in Fig. 3.39(a).

In the SEM images of Figs. 3.39(b) and 3.39(c), individual nanowires form an assembly. As it is shown in Fig. 3.39(c), nanowires are twined and mashed together by the force gradient from the vacuum applied, to form a macroscopic assembly. The thickness of the film was approximately 7 μm, as the SEM micrograph of the film-edge in Fig. 3.40 shows.

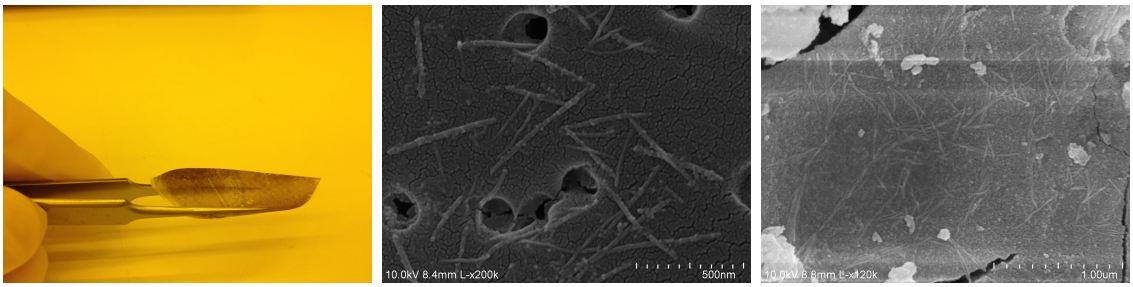

(a) (b) (c)

Figure 3.39: (a) Photograph of CdTe NW assembly following the film's removal from the vacuum filtration paper. (b,c) SEM images of CdTe NW assembly surface showing the agglomeration of individual nanowires in the assembly.

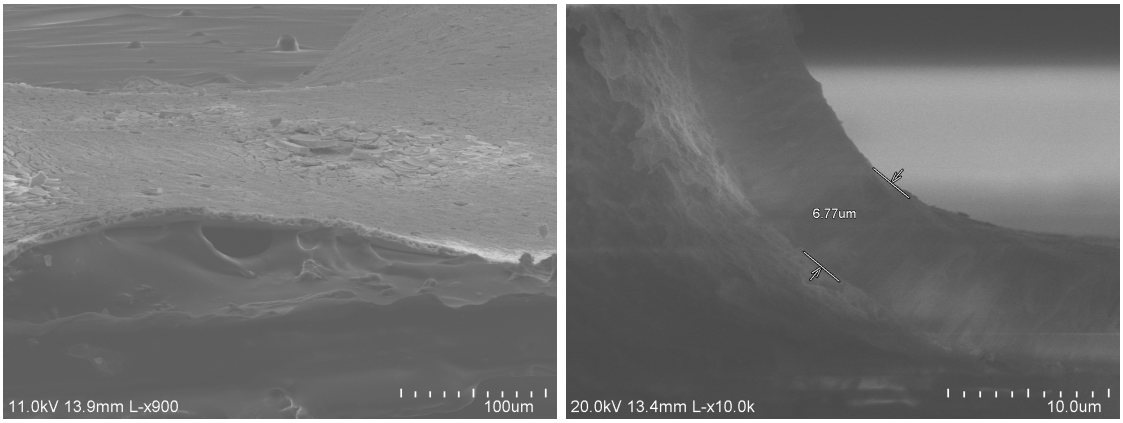

(a) (b)

Figure 3.40: SEM images of CdTe NW assembly showing the cross-sectional view of the NW assembly exhibiting $\sim$7 μm thickness.

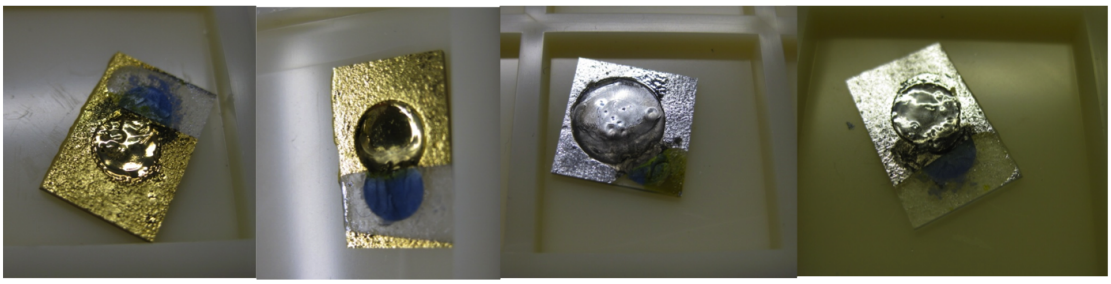

Figure 3.41: PbSe NC/MEH-PPV composite assembly samples after top metal contact deposition.

3.3.5 Metal contacts

Various metal contacts can be used to abut the NC assembly, in which the band-structure can vary significantly with the particle size. In general, most of the materials used in this research including MEH-PPV, are known as p-type and therefore metal contacts with higher work functions, such as Pt (5.6 eV) and Au (5.2 eV), were used for the ohmic contact, and the rectifying contact was applied by depositing lower work function metals, such as In (3.8 eV) and Al (4.2 eV). Various types of NC assembly samples were sandwiched by 300 nm of metal contacts, which were evaporated with the Enerjet e-beam evaporator at the Lurie Nanofabrication Facility in the University of Michigan. Various combinations of samples were made in order to study the effects of the metal contacts, including Pt/NC/Pt, Pt/NC/In, Au/NC/Au, Au/NC/In, etc. Nevertheless, the behavior of the resulting detector does not depend strongly on the bounding Schottky barrier; rather, the charge creation and transport is more dependent on the uniformity of the colloidal solid underlying the electrodes, as will be discussed in the next chapter (Chap. IV). Fig. 3.41 shows some examples of completed detectors.

In this chapter, synthetic procedures for colloidal NC dispersions of CdTe, PbS and PbSe were described, and various characterization methods for the NC dispersion were introduced. Specifically, TGA-stabilized CdTe NCs were synthesized aqueously,

whereas PbS and PbSe NCs were synthesized through injecting lead-oleate precursors into non-polar organic solvents. Variation to the reaction conditions in the synthesis – injection and growing temperature, growing time, and precursor ratio – resulted in changes in the size and shape of the NCs, which were investigated with TEM, XRD, and PL measurement.

NC-based assemblies were fabricated utilizing the self-assembling nature of the NC, where colloidal NC deposition methods including drop-, slide-, spin-casting and dip-coating were attempted in combination with the LBL deposition method and the ligand exchange treatments. For example, assemblies of CdTe NC/PDDA bilayer were formed via dip-coating and spin-casting methods, and PbS NC assemblies were formed through drop-, slide-casting, and dip-coating methods. CdTe NW assemblies were fabricated by introducing the vacuum filtration method, as an attempt to overcome limitation of NCs in charge carrier transport and to reduce the fabrication time and effort to form an assembly of the large volume. Lastly, blended-structure assemblies of the PbSe NC/conductive polymer composite were fabricated as a means to overcome challenges in charge carrier transport properties of the NC assembly.

Surface morphology of the NC assembly was investigated by an SEM to characterize the uniformity of the assembly, where we could identify the crack and crumb formation; the surface condition of the NC assembly depends on the detail of the fabrication method and process. Metal contact combinations comprised of Pt, Au, In and Al were evaporated on the top and the bottom of the fabricated NC assembly, which will be investigated for their electrical properties and responses to the radiation in the next chapter (Chap. IV).

CHAPTER IV

Results and Evaluation

Nanocrystal assemblies, made of CdTe NCs, CdTe NWs, PbS and PbSe NCs, fabricated with various procedures described in the previous chapter were tested for: a) electrical properties and b) radiation response when struck by alpha and gamma radiation sources. Fig. 4.1 presents a typical configuration schematically shown for the NC assembly detectors formed by either drop-, slide-, spin-casting or dip-coating, making use of its self-agglomerating nature, and finally sandwiched between various metal contacts. The current-voltage (I-V) characteristic curve was investigated for the NC assembly samples in order to discern the electrical nature of the underlying colloidal solid. The responses of the NC assemblies to the radiation sources were then studied via alpha particles from an Am-241 source, and the best quality samples were tested for the gamma-ray response using various gamma sources – Ba-133 for low energy gammas, Cs-137 for intermediated energy gammas, and Na-22 and Co-60 for high energy gammas. Gamma-ray spectrum was acquired using a typical Nuclear Instrument Modules (NIM) apparatus. ORTEC 142A preamp, ORTEC 571A amplifier, and Trump 8K MCA (ORTEC) or Pocket MCA 8000A (Amptek) were mainly used to collect the differential pulse height spectra from the energy deposition of incident radiation quanta.

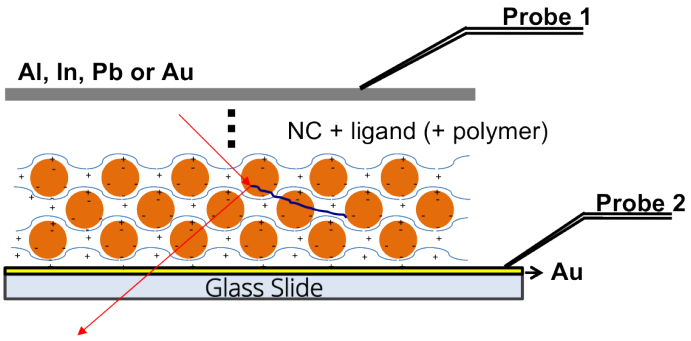

Figure 4.1: Schematic illustration of the NC assembly bounded by the top and bottom electrodes.

4.1 CdTe Nanostructure System

4.1.1 CdTe Nanocrystal Assembly

4.1.1.1 Drop Cast Samples of TGA Stabilized CdTe NC

Fig. 4.2 shows typical I-V curves obtained from the drop-cast CdTe NC assembly samples deposited on the Au- and Al-evaporated glass slides. Each probe needle was placed on the NC film and the metal substrate, expecting that the tungsten probe tips will make a metal-semiconductor contact on the top side. Known as a p-type semiconductor, in general, bulk CdTe (electron affinity 4.44 eV, ionization potential of 5.97 eV) [110, 111] will exhibit rectifying behavior at an Al or In interface, and it will make an ohmic contact with higher work function metals such as Pt and Au [91–93]. However, Pt and Au cannot make a perfect ohmic contact, as one can often observe the effect of space charge limited (SCL) current in the lower bias region of the typical I-V curves of bulk CdTe, which manifests the existence of the space charge region created by the potential barrier at the metal-semiconductor contact. This phenomenon is expected to be more prominent in the NC assembly-metal contacts because the energy band gap broadens, and a number of trapping sites and levels in the NC assembly will introduce much more space charge that prohibits the current flow. Thus, both Al and Au formed rectifying contacts with the nanocrystalline

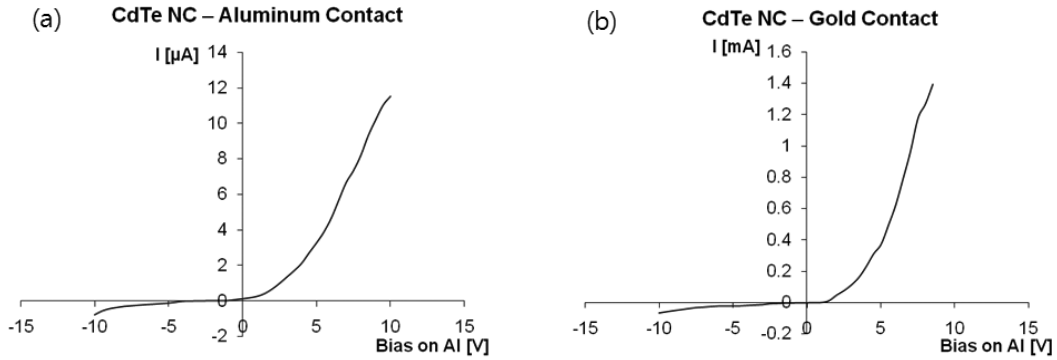

(a) Al/CdTe NC

(b) Au/CdTe NC

Figure 4.2: Current-voltage characteristics of CdTe NC assembly drop-cast on (a) aluminum and (b) gold evaporated substrate.

CdTe, as expected given the relative band-structure of the adjoining materials. The aluminum contact had higher contact resistance than the gold-NC system, since a higher potential barrier for the flow of majority carriers (holes) is expected from the CdTe NC-Al contact, but both exhibited Schottky contact formation and charge depletion in the detector bulk.

The CdTe NC-Al contact sample, which has good rectifying behavior, was tested under alpha particle impingement from an Am-241 source. Given the large agglomeration of NCs connected by the organic coordinating materials into the solid, a poor detector response was produced as expected. Pulse height spectrum from the MCA as shown in Fig. 4.3 exhibits a slight shoulder above the electronic noise in the background.

4.1.1.2 Layer-by-Layer Assembly

The CdTe NC-Al contact devices made by the LBL method with multiple cycles of manual dip-coating also exhibited rectifying behavior at the lower bias range of -20–0 V, as shown in Fig. 4.4. By either the LBL or drop-casting method, low work function metals such as aluminum or indium make a good blocking contact with high potential barriers applied on the metal-NC assembly boundaries. Even though it is

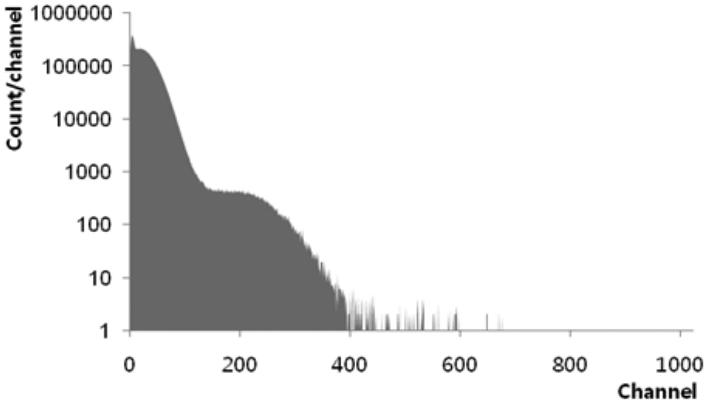

Figure 4.3: Energy spectrum of Am-241 alpha source obtained from a drop-cast CdTe NC-assembly detector, with an aluminum contact, utilizing an Ortec 142A preamp and an Ortec 572A shaping amplifier.

hard to find a perfect ohmic contact material for which the energy band is aligned with the ionization potential of CdTe, gold and platinum can make a reliable resistive contact for the material. Thus, one can utilize a Al(or In)/CdTe NC/Au(or Pt) structure for a Schottky diode-type detector configuration.

Fig. 4.5 shows response of the CdTe NC assembly shown in Fig. 3.27(c), derived from the charge sensitive preamplifier and shaping amplifier when impinged by an 5.5 MeV alpha particle. The CdTe assembly was formed by LBL deposition of 48 bi-layers via spin-coating on gold-evaporated silicon wafer, topped with an indium contact. Both metal contacts were 300 nm thick deposited by e-beam evaporation with a rate of 10 Å/s. The signal was distinguishable from the noise fluctuation, verified by its appearance correlating with the presence of the radiation source. However, the energy spectrum did not produce a discernible alpha peak above the threshold. The spectrum looked similar to the spectrum shown from the drop-cast sample above (Fig. 4.3). One expects only slight energy depositions within a ∼170 nm layer, particularly for weakly ionizing electrons. Even if one exposes the assembly to 5.485 MeV alpha particles (from Am-241), the energy deposited from the transmission of the ion

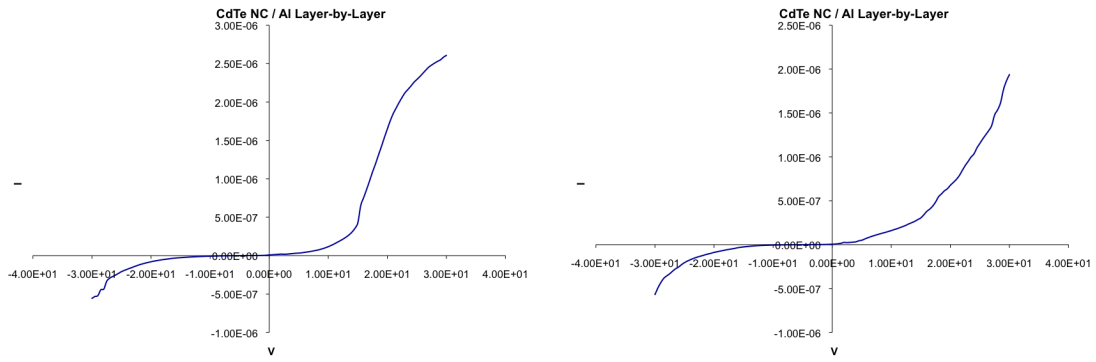

(a) (b)

Figure 4.4: I-V curves of CdTe NC assembly formed by LBL dip-coating on Al-evaporated substrate. Two samples show slightly different behavior in the forward bias, which is speculated to be the stronger influence of space charge effect induced by trapping sites on boundaries, polymers or surfactants.

through the layer is estimated to be less than 50 keV.[1] This is enough energy to produce a measurable signal, which is very promising because gamma-rays, for instance, can produce energy depositions that are 10 times as big if there is enough volume to fully stop the products (primary and secondary electrons) of the interaction.

Interestingly, CdTe NC assembly samples sandwiched between aluminum and platinum contacts exhibited very promising results, which were also highly reproducible; technically, 16 out of 16 detectors showed a similar response. Fig. 4.6 shows the alpha signal derived from the preamplifier and shaping amplifier. 58 repetitions of LBL deposition was performed to create the NC assembly of which the thickness was estimated to be ∼250 nm from a SEM study, as shown in Fig. 3.29. These samples were tested at 0 V bias applied, with and without the Am-241 source. Notably, these samples have shown very good charge transport properties, which is represented by the sharp rising characteristics of the signal, compared with Fig. 4.5. Moreover, the signal amplitude per each incident quanta of an alpha particle was fairly large, considering that the amount of kinetic energy that can be deposited in a 250 nm assembly

[1]This depends on the kinetic energy of the alpha particle, which is dependent on the distance between the source and the detector

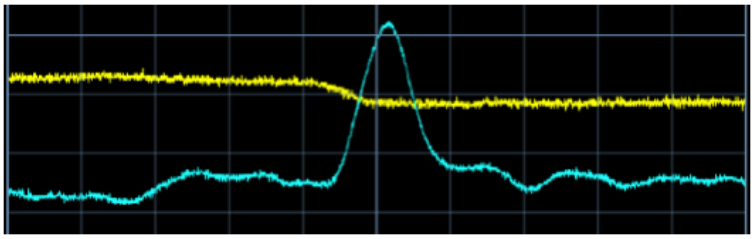

Figure 4.5: The alpha signal pulse derived from the charge sensitive preamplifier and corresponding shaping amplifier coupled to a Au/CdTe NC/In LBL assembly: Preamp (yellow) and shaped (blue) signals derived from the passage of a 5.486 MeV alpha particle through a ∼170 nm CdTe nanocomposite detector, in which the induced charge signal is measured with a ORTEC 142A preamp. The time scale is 10 μs per division and the vertical scale is 20 mV and 1 V per division for the preamp and shaped pulse.

was only less than 100 keV at most.[2]

Pulse height spectrum was acquired for the (expectedly) *transmissive* alpha particles incident on the sample. Fig. 4.7 shows the pulse height spectrum acquired from the Al/CdTe NC/Pt assembly sample with/without existence of the Am-241 source. Compared with the background, i.e., without the source, the NC sample produces remarkably larger number of pulses when the Am-241 source exists. The peak area is expected to be the major energy deposition of the alpha particle when it is penetrating through the detector. The continuum area in the lower channels is attributed to the energy straggling effect and inefficient charge collection mechanisms of the NC assembly (e.g., trapping at various boundaries, contact resistance, space charge limited behavior). In addition, the alpha source was not collimated, thus, the energy deposition of the alpha particle will inherently have a finite distribution in energy deposition, depending on their path through the source and intervening air volume.

The gamma ray response was also tested for the assembly, however, we did not expect either high count rates or sizable pulses, considering that the thickness of the assembly was only 250 nm; the interaction probability with the incident gamma

[2]This can be also verified with a SRIM/TRIM simulation as will be discussed in the next section (4.1.2.1).

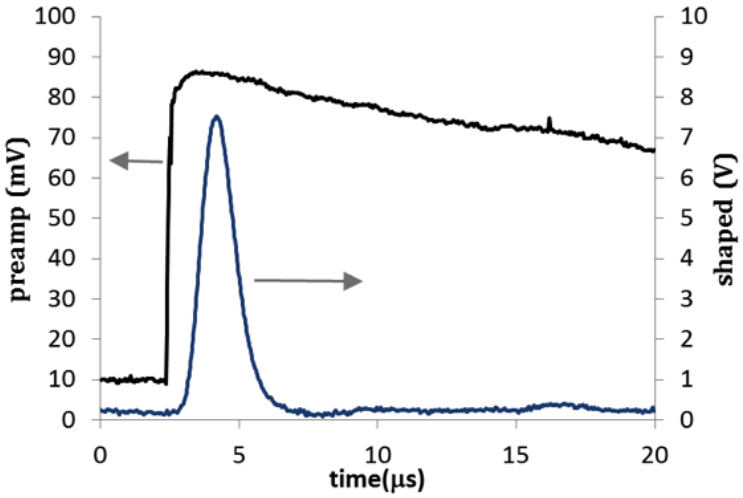

Figure 4.6: The alpha signal pulse derived from the charge sensitive preamplifier (black) and corresponding shaping amplifier (blue) coupled to an Al/CdTe NC/Pt LBL assembly.

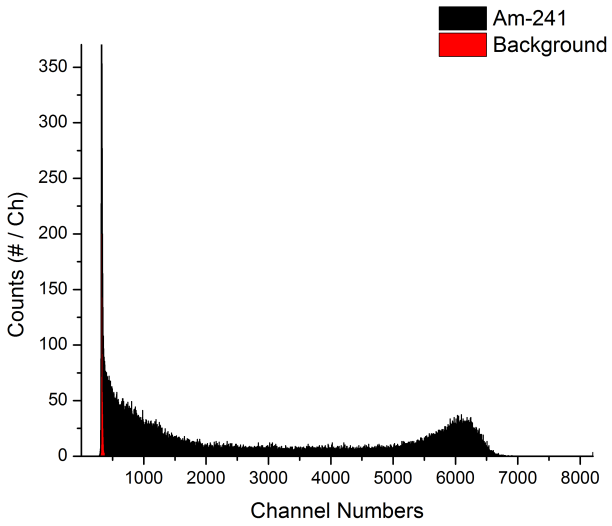

Figure 4.7: Pulse height distribution derived from ~250 nm CdTe NC detector operating in transmission mode.

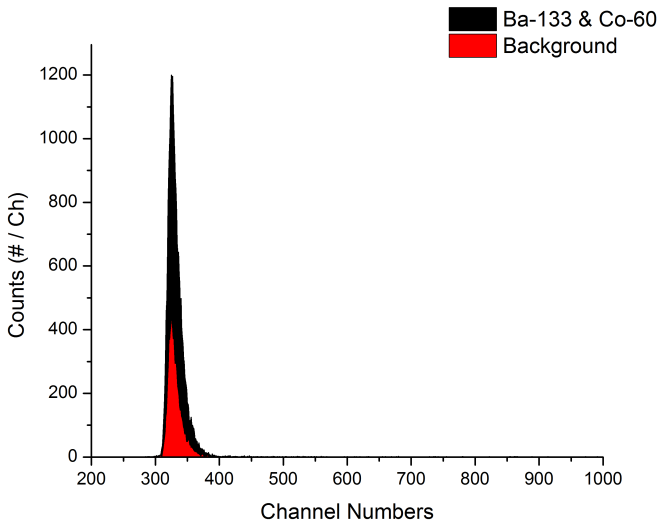

Figure 4.8: Gamma response from the Al/CdTe NC/Pt assembly deposited with LBL method; overall increase of the count rate was observed with existence of the gamma sources.

is extremely low. Furthermore, as discussed in the PENELOPE simulation (2.3.1), even 80 keV electrons (from either photoelectric effect or Compton scattering) can proceed $\sim$10 μm before they are mostly stopped; thus the energetic primary electrons will escape from the detector volume. Fig. 4.8 shows the comparison of responses from the CdTe NC assembly sample with and without the gamma sources. Note that the low discrimination level for the MCA was set as 250 channel in order to reduce the influence from the noise fluctuation on data collection; continuous distribution of the pulse height spectrum is chopped off at 250 channel. One can notice that the number of counts in total increases slightly when the source is present, however, none of the discernible features from the gamma-ray energy spectrum was observed. The relatively rare gamma-ray interactions will deposit only a small portion of their energy, yielding charge depositions that are on the same order of magnitude as the noise fluctuations.

Even though the cadmium salts may not be as favorable as their lead equivalents – at least in their physics properties – they represent a promising material upon

which nanostructured ionizing radiation detectors can be developed. Furthermore, detectors fabricated using the LBL method are more reproducible in their behavior than those that are solidified using gross drop- or spin-casting methods. As shown in Fig. 4.7, the results are nevertheless promising because only several tens of keV is deposited during the alpha-particle passage, resulting in a signal that has excellent signal-to-noise and good charge transport. Note further that the detector is unbiased because we made an effective Schottky junction to the underlying material. The CdTe NC assembly fabricated by the LBL method therefore works very well in the range of a couple hundred nanometers thick which is typical dimension of existing NC-based devices. In fact, one pathway through which one might be able to make thick, large area detectors is to continue the LBL method to larger thickness values, the main drawback being the time required to realize efficient detectors. For instance, roughly 80 hours of the water-based drop-and-dry synthesis is required to realize 10's of micrometers of material thickness. This lengthy process time motivated the CdTe nanowire assembly approach using the vacuum filtration method as was discussed (3.1.2).

4.1.2 CdTe Nanowire Assembly

The CdTe NW assembly sample including the metal deposition, is shown in Fig. 4.9(a). The sample was cut with razor and tested for its electrical characteristics and radiation response. In order to avoid electrical shorting, we masked the sample with aluminum foil, and only a limited area of the sample was deposited by the metal contact (Fig. 4.9(b)). Fig. 4.10 shows the indium deposited sample in the test box. Note that the backside is evaporated with gold.

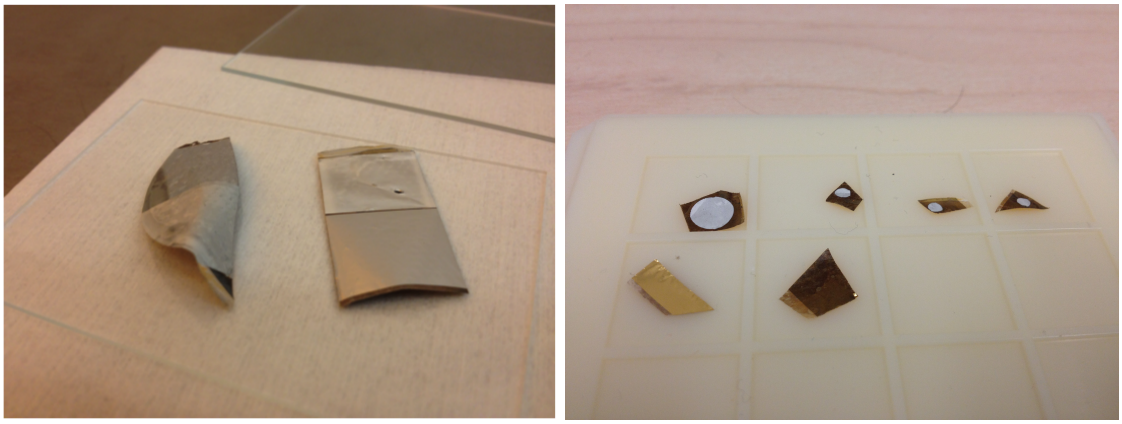

(a) (b)

Figure 4.9: (a) CdTe NW assembly after the metal deposition from the Enerjet evaporator. (b) CdTe NW assembly after cut with a razor. Top metal is indium and the bottom contact is evaporated with gold.

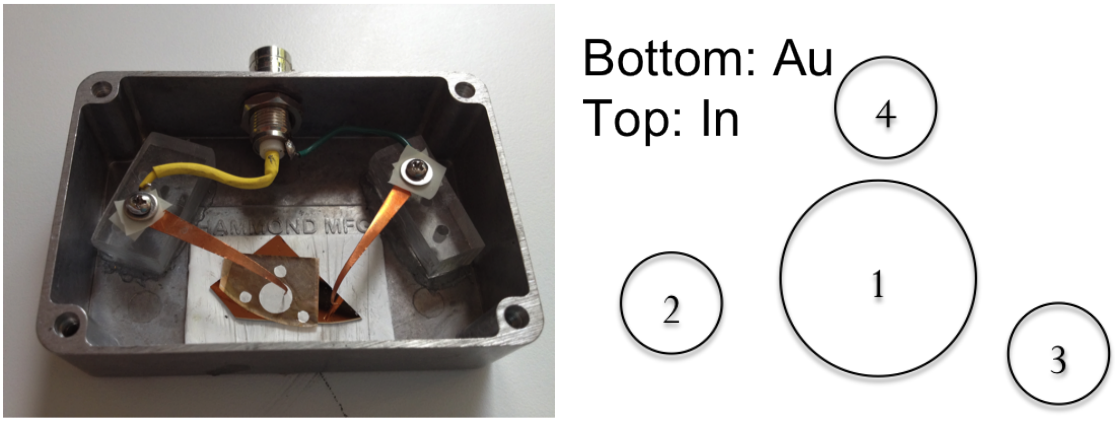

(a) (b)

Figure 4.10: A photography of CdTe NW sample in the testing box. The top metal contact is indium and the bottom contact is gold. The sample was masked during the indium contact deposition in order to avoid the electrical shorting. Bias is applied on the indium side.

4.1.2.1 Simulation

A SRIM calculation [71] was performed for the 5.486 MeV (85.2%) and 5.443 MeV (12.8%) alpha particle emitted from the Am-241 source. First, the particle track was simulated (Fig. 4.11(a)) to estimate the energy loss of the alpha particle in the air for an 18 mm distance from the source as shown in Fig. 4.10. The alpha particles transmit through the air and arrived at the detector surface with an energy of $\sim$3.6 $\pm$ 0.1 MeV. The energy of the transmitted alpha particle through the $\sim$7 μm thick CdTe NW assembly and single crystal CdTe thin film (for comparison) was also calculated.

Fig. 4.11(b) shows the distribution of alpha particle energy emitted from the Am-241 source and then transmitted through the source-detector distance and the detector volume. Here, the CdTe NC layer is modeled as follows. CdTe NCs exhibiting 550 nm PL emission are known to be approximately 3 nm in diameter, and a 3 nm CdTe has approximately 100 atoms and about one third of them are on the surface; thus they are terminated by the capping ligands (TGA – $C_2H_4O_2S$). We have used that ratio to estimate the energy profile from the alpha source arriving at the detector medium and through the detector medium. The energy profile of alphas transmitted through the modeled 7 μm CdTe NW assembly was calculated to be $\sim$2.5 $\pm$ 0.12 MeV, and the energy profile of the alphas transmitted through the modeled 7 μm single crystalline CdTe layer was calculated to be distributed in $\sim$1.4 $\pm$ 0.15 MeV.

Whereas CdTe NCs are enclosed by TGA capping ligands, CdTe NWs are an assembly of CdTe NCs for which the ligand is partially removed and assembled together where the ligand is absent. Therefore, NWs have less ligand density expected than from the CdTe NCs, and the alpha particle is expected to lose more energy than the CdTe NC layer modeled. However, the density of the sample, as measured with a balance, at 1.8 g/cm^3, compared with 7.8 g/cm^3 of the single crystalline CdTe, suggests that the NW packing is sparse; therefore, the 1.1 MeV estimate of the energy deposition is an upper bound on the experimental energy utilized.

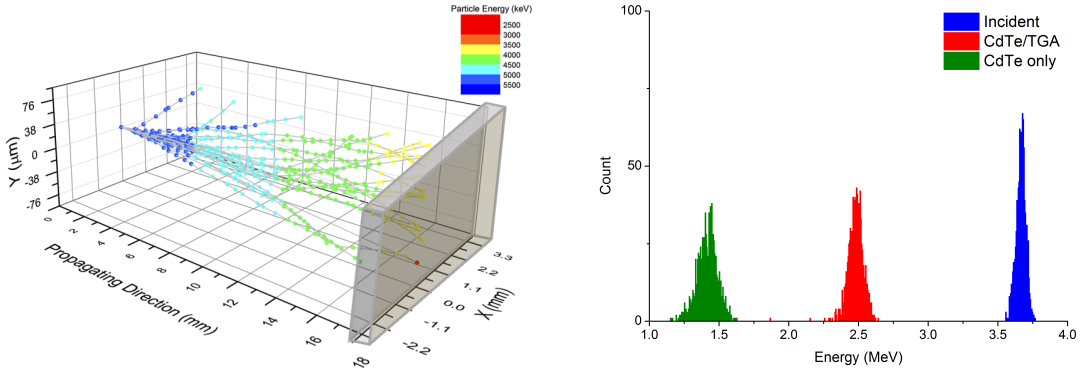

(a) (b)

Figure 4.11: Particle track simulation by SRIM and the transmitted energy of alpha particle emitted from the Am-241 source.

This technique can be combined with many other experiments testing the thin film detector with radiation impingement, as was discussed in the previous section regarding the amount of energy deposited on the 250 nm thick CdTe NC assembly. Not only limited to alpha particles, this method can be combined with MCNP simulation or PENELOPE simulations to study the actual amount of energy that is likely to be deposited in the detector volume.

4.1.2.2 Measurement

Electrical Properties The electrical properties of a thin film semiconductor are influenced, in part, by the barrier height at the material interfaces, and by the trapping of charge carriers in the bulk of the material, the resulting space-charge from which can induce hysteresis in the current-voltage characteristic [112]. Based on the research into organic semiconductors [113] and polycrystalline silicon thin-film transistors (TFTs) [114], the hysteresis is attributed to some combination of: a) the trapping/detrapping of charge carriers at the interfaces, b) polarization of the material (such as ferroelectricity), and c) charge injection from electrodes [112–114].

Furthermore, polarization of the CdTe crystal is well known, and the mechanism

for the material's polarization has been extensively studied [91–93]. The gradual accumulation of fixed space charge in the crystal deforms the electric field and affects the charge carrier motion, an effect that manifests itself in a "space-charge limited (SCL)" current effect which is often modeled as a quadratic form of current in a voltage sweep.

The electrical properties of the prepared sample were investigated by measuring current-voltage (I-V) curves with a Keithley 4200-SCS measurement tool at room temperature. The measurement was done with a high accuracy, long integration time mode ("quiet sweep" with 138 ms measurement period), and a 0.5 s sweep delay and hold time was used in order to stabilize the device between measurements.

The current-voltage (I-V) characteristic curves are illustrated in Figs. 4.12–4.14, in which the curves for each sample are measured between (a) ±10 V, (b) ±50 V, (c) ±200 V, and the voltage-sweep bias was applied on the indium side. Each figure corresponds to I-V curves measured at the different areas of the NW sample shown in Fig.. 4.10, in which Spots 3 (and 2, not plotted) were nearest the boundary of the filtration paper, and Spot 4 was closest to the middle of the paper. One expects contact areas 1 and 4 to have experienced a higher force gradient during vacuum filtration, which can potentially impact the density of the NW packing. Figs. 4.12–4.14 provide evidence that there is indeed a difference in the transport characteristics of the sample as the position is varied.

Specifically, Spot 3, which is nearest the edge of the filter used to assemble the solid, has an I-V curve (Fig. 4.13) that exhibits a high degree of hysteresis with very low current flow (sub pA), both observations of which are consistent with poor charge transport in the assembly and insulating behavior. The measured leakage current values are 0.2 pA at +10 V bias, 2.3 pA at +50 V bias, and 40 pA at +200 V bias.

Spot 1 (Fig. 4.12) shows that the charge carrier conduction is slightly more limited

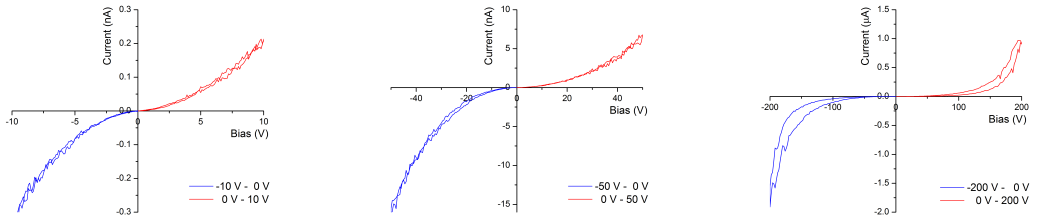

(a) (b) (c)

Figure 4.12: Current-voltage (I-V) characteristic curves measured from **Spot1** of Fig. 4.10 of the CdTe nanowire assembly with Au/In contacts. Note that the bias is applied on the In side.

under positive bias, as expected, since the indium contact makes a Schottky contact to the sample. In Fig. 4.12, note that the leakage current is 0.2 nA at +10 V bias, 7 nA at +50 V bias, and ∼1 μA at +200 V bias. Little hysteresis was observed at the lower biases; however, one can see an increased hysteresis effect near 200 V. This effect may be due the phenomena that at higher electric field gradients, the barrier to trap-assisted tunneling is reduced and conduction into and out-of traps farther from the band-edges can modulate the current flow to a higher degree.

The same trends are observed in the sample (Spot 4 in Fig. 4.10) taken from the center of the filter paper, which exhibits good charge conduction behavior. Leakage currents of the sample are 0.5 nA at +10 V, 12 nA at +50 V, and ∼4 μA at +200 V bias (Fig. 4.14). All else being equal, one would prefer to avoid a material that develops a space charge and/or traps the carriers and we therefore focused the radiation response studies on those samples with a smaller hysteresis effect.

Radiation Response

Alpha source response In order to investigate the radiation response of the NW assembly, alpha particles from an Am-241 source were irradiated upon the Au/In contact sample. We used an ORTEC 142A preamp, an ORTEC 572A Amplifier and

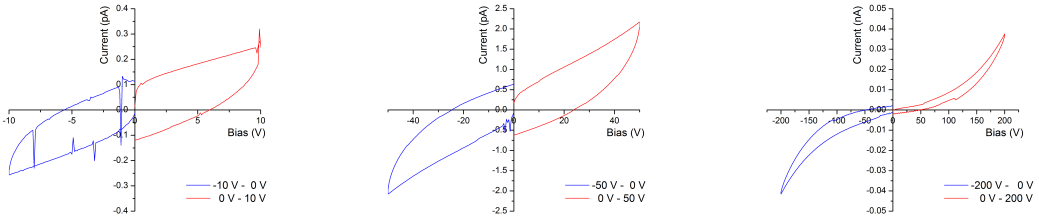

(a) (b) (c)

Figure 4.13: Current-voltage (I-V) characteristic curves measured from **Spot3** of Fig. 4.10 of the CdTe nanowire assembly with Au/In contacts. Note that the bias is applied on the In side.

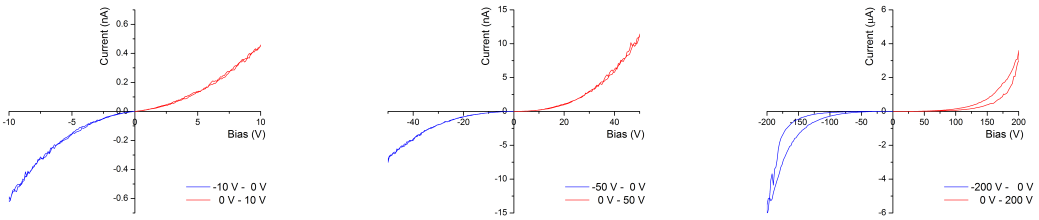

(a) (b) (c)

Figure 4.14: Current-voltage (I-V) characteristic curves measured from **Spot4** of Fig. 4.10 of the CdTe nanowire assembly with Au/In contacts. Note that the bias is applied on the In side.

the pocket MCA 8000A from Amptek to evaluate whether the effects of alpha particle impingement was observable. A high gain on the shaping amplifier (1500) was needed to effectively observe that signals, in contrast to the CdTe LBL samples and PbSe devices (discussed later). Furthermore, the carrier transport time through the 7 μm sample was measured in the tens of μs, rather than the preferred hundreds of ns. Thus, the NW assembly exhibited neither fast transport nor a high charge-creation yield, both consistent with a solid of sparsely-packed NWs.

Nevertheless, one can acquire pulse-height distributions during ion impingement if the sample is biased above 100 V. For instance, Fig. 4.15 shows the distribution derived from (large area) Spot 1, taken at an applied bias of 300 V, which was approached slowly (over several minutes) in order to allow the space charge to dissipate. Note that rapidly ramping the voltage can induce non-destructive breakdown paths to form in the sample, as indicated by pulsing that doesn't accompany radiation impact.

Fig. 4.16 shows the response from contacted area 4, the device closest to the center of the filtration paper, and exhibits a similar alpha particle response to the larger Spot 1 device. Note that the device was biased near that plotted in Fig. 4.15, but the measurement period was much longer, which accounts for the greater number of counts in the distribution.

The shape of the distribution is that which we expect from an Am-241 disk source impacting a standard single-crystalline detector, such as that made from silicon, if very small energy depositions are made. Comparing the response with that (cf. Fig. 4.7) from the much thinner CdTe LBL detector (250 nm vs. 7000 nm), the LBL device has faster transport, larger signals, and consequently, greater separation between the noise and the radiation signal.

Thus, even though the NW samples were motivated, in part, by a desire to improve the charge transport characteristics of the devices – providing transport channels along the wire rather than hopping between ligand-separated NCs – the results indi-

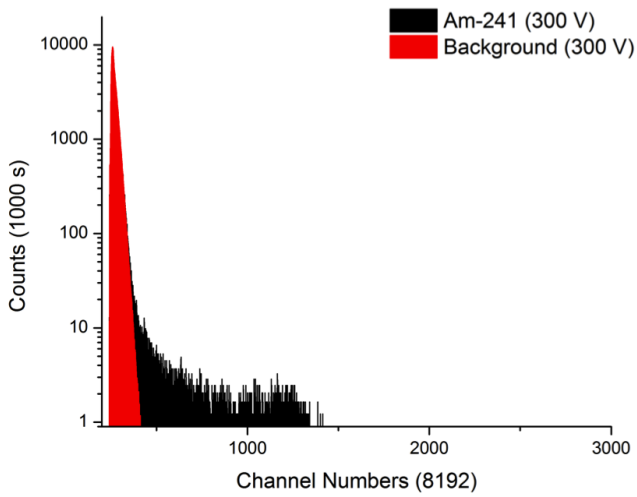

Figure 4.15: Spectral response of the CdTe NW sample, Spot 1 (big spot) to the Am-241 alpha source, measured for 1000 s at 300 V bias applied on the indium contact side, compared with the source-free background spectrum measured for the same amount of time.

cate that this wasn't achieved because of the relatively low density of the disordered NW array.

Gamma response The CdTe NW assembly was also examined for the gamma ray response. The test was conducted on the Spots 1 and 4 of the CdTe NW sample previously tested with an alpha source. As expected, it was hard to obtain a statistically meaningful number of counts in the spectrum; thus, not a distinguishable feature was observed. It was tested with both low energy gamma sources (Co-57, Cd-109, Ba-133) and high energy gamma sources (Cs-137, Co-60). Due to small number of charge carriers created per incident quanta for low energy (359 keV or below) gamma, signal pulses were not distinguishable from the noise fluctuation. Observing features for the high energy gammas were also challenging because: a) it was hard to achieve enough gamma interactions from the small active volume of the assembly, and b) the expected dimension scale of the charge cloud created by the gamma ray interaction was much larger than that created by an alpha particle, as well as the overall size of

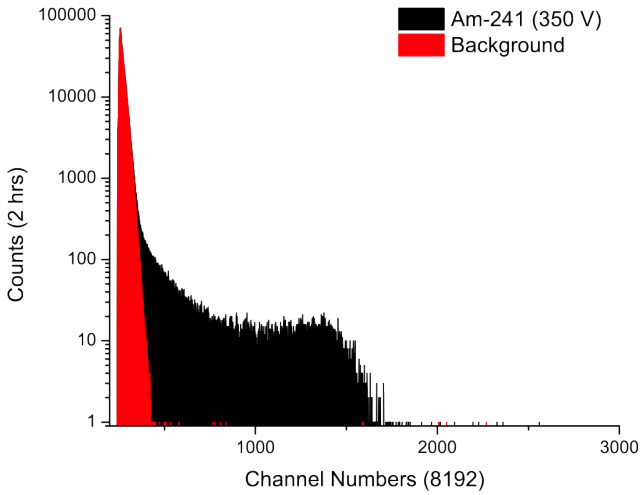

Figure 4.16: Spectral response of the CdTe NW sample, Spot 4 (small spot) to the Am-241 alpha source, measured for 2 hours at 350 V bias applied on the indium contact side, compared with the source-free background spectrum measured for the same amount of time.

the assembly.

Fig. 4.17 shows the gamma ray response of the CdTe NW sample obtained for 9 hours at the Spot 1. Distributions above the background noise presents the gamma-induced response of the sample. The gamma ray response obtained at the Spot 4 did not present discernible features over the background, due to much smaller size of the contact, which limits the active volume for the interaction.

4.2 Lead Chalcogenide (PbX, X = S, Se, Te) Nanocrystals

4.2.1 Plain Drop/Spin Cast Samples

PbS and PbSe colloidal dispersions coordinated with relatively long chained oleic acid group ligands (∼1.5 nm) were investigated and formed into NC assembly solids. The lead chalcogenide NC samples drop-cast on the metal evaporated glass slides were tested for the I-V characteristics to characterize the NC-metal contact. Experiments were conducted in a similar manner with the drop-cast CdTe NC assemblies: probe

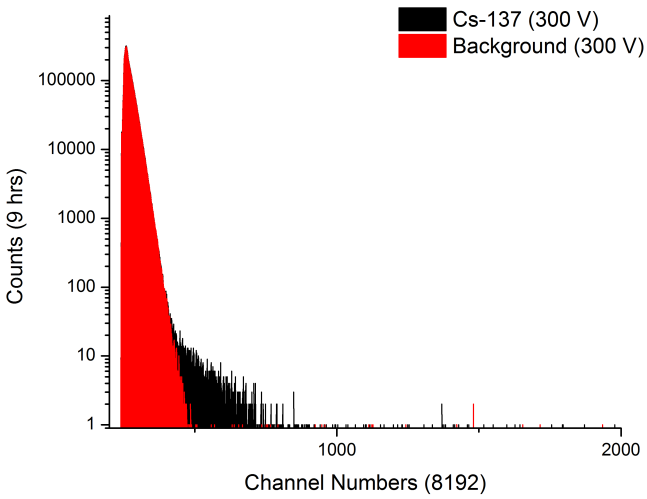

Figure 4.17: Spectral response of the CdTe NW sample to the Cs-137 gamma source, compared with the source-free background spectrum measured for the same amount of time.

needles were placed on the top and bottom of the NC assembly. However, as shown in the SEM images (Fig. 3.24) studied for various drop-cast NC assemblies, there were significant morphological changes across the solid. Depending on which area one put the contact probes on, the I-V curves have very diverse responses. Two examples shown in Fig. 4.18 represent I-V curves obtained from the drop-cast plain PbSe NC samples without any further treatment. Known as p-type material, PbSe is expected to form a Schottky contact with aluminum and a resistive contact with platinum. However, for both PbSe NC/Al and PbSeNC/Pt contacts, the I-V curves showed a similar resistive behavior at the interfaces with poor conductivity, which indicates that the charge transport is constricted by the carrier trapping in the organic coordinating matrix in the sample.

Fig. 4.19 shows I-V curves collected from another set of PbSe NC assemblies formed by the drop-casting method on the metalized substrate, as shown schematically in Fig. 3.21 and the fabricated samples illustrated in Fig. 3.23. Notably, the NC assembly samples also exhibit resistive behavior, with small current leakage. The

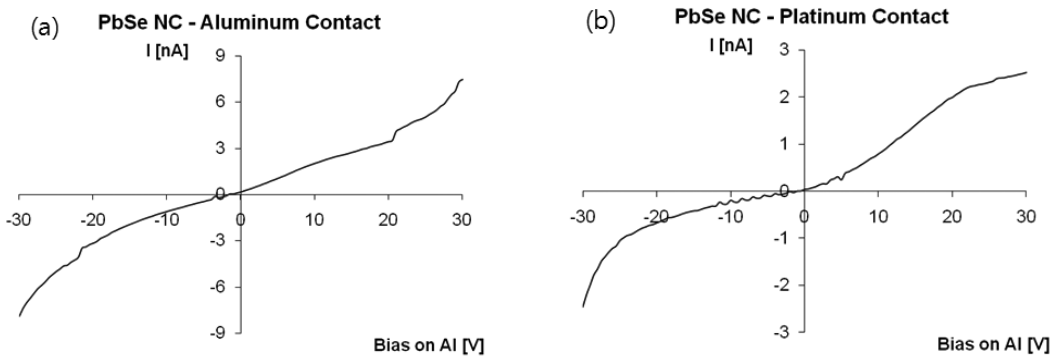

(a) Al/PbSe NC (b) Pt/PbSe NC

Figure 4.18: Current-voltage characteristics of PbSe NC assembly drop-cast on the metal substrate.

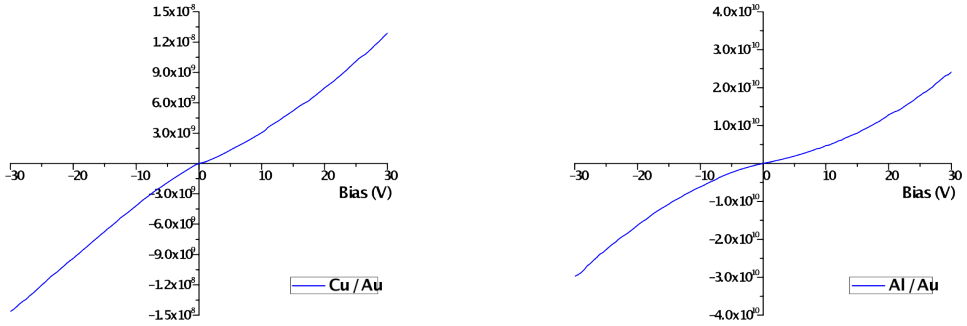

(a) Cu/PbSe NC/Au (b) Al/PbSe NC/Au

Figure 4.19: Current-voltage characteristics of PbSe NC assembly drop-cast as shown in Fig. 3.23.

NC assembly with the Cu/Au contact develops 14 nA of current when 30 V voltage bias is applied, and the assembly with the Al/Au contact exhibits a current 0.3 nA at the same bias condition. However, the thickness of the NC sample was several times thicker for the latter sample, estimated from the number of droplets cast on the substrate, a number usually measured in the hundreds. This small current behavior is expected for the samples because the long (∼1.5 nm) insulating oleic acid capping ligands retard charge flow and prevent delocalization of the electronic wavefunctions.

The spin-casting method with NCs as-synthesized was also attempted. The spin-

Smpl ID	NC ID#	NC size	NC shape	Polymer	Deposition Method	Contact	Amount
②	0724	5 nm	Sphere	NO	Spin-cast	Au / Al	20 u X 10
③	0724	5 nm	Sphere	NO	Spin-cast	In / Au	20 u X 10
④	0926	12 nm	Star	NO	Spin-cast	Au / In	20 u X 10
⑤	0926	12 nm	Star	NO	Spin-cast	In / Au	20 u X 10
⑥	0724	5 nm	Sphere	NO	Spin-cast	In / Pt	20 u X 10
⑦	0926	12 nm	Star	NO	Spin-cast	Au / Au	20 u X 10
⑧	0926	12 nm	Star	NO	Spin-cast	In / Pt	20 u X 10
⑨	0724	5 nm	Sphere	NO	Spin-cast	Au / Au	20 u X 5

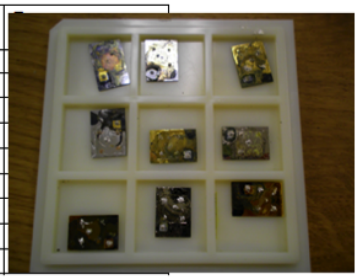

Photoluminescence measurement :
0709, 0724 : 1450 nm – ~ 5 nm – spherical shape
0926 : 1650 nm – 12 nm : star-shaped

(a)

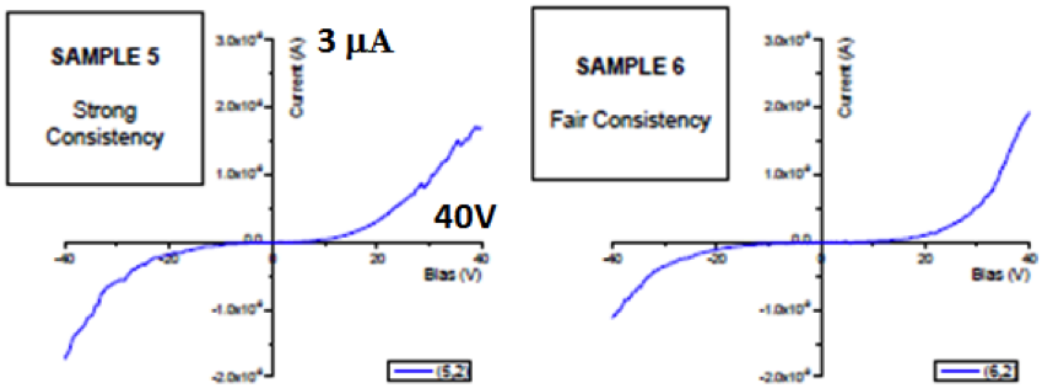

(b)

Figure 4.20: Summary of spin-cast NC detector samples, each of which is coordinated by oleic acid capping ligands.

casting was performed at a slow spinning speed of 60–90 rpm. A summary of other batches of NC assembly detectors coordinated by the oleic acids, which is spin-cast on silicon and glass substrates, is shown in Fig. 4.20(a). Note that with spheres or star-shaped NCs of various size, when bound by various contacting electrodes, the behavior is similar to the I-V curve shown in Fig. 4.20(b), in which the resistive detector may have different degrees of resistivity, but the radiation-induced signals are always either weak or buried in the noise. We therefore require a solution in order to realize the promise of NC-based detectors.

As one of the attempts, one can employ a different electronic read-out architecture; that is, one could look at the early induced current rather than the integrated induced

charge. Upon creation, the charges in the PbSe NCs do transport to the surface of the dot, where they are slowed and trapped by the insulating organic structure. If one can focus on that initial transport, then one can potentially extract a clean signal. However, this requires the development of a new very high-speed circuit, and more importantly, the organics surrounding the quantum dots participate in energy extraction from the radiation-induced primary particle, thus reducing the information extraction. We would therefore rather improved the underlying material itself.

The poor charge transport was confirmed as I-V curves shown above, when the samples were tested for radiation responsivity, in which a charge-sensitive preamplifier failed to collect radiation pulses that were distinguishable from the noise, as induced from an Am-241 source; instead, the resulting solid acted like an insulator. We know (from other detector measurements with the NCs) that the radiation (alpha particles or secondary-electrons) produces electron-hole pairs within the quantum dots themselves. An electric field is also formed across the detector volume, with the active region acting like a resistive detector. The charges are thus well-created and transit through the NCs themselves; however, the charge transport is retarded by the poorly conducting oleic acid groups such that the charge is trapped and collected over long enough periods that the shaping times used were too short to discern any signal without picking up electronic noise fluctuations. Although a current-sensitive preamplifier can potentially be employed to sense the induced charge signal, in order to maximize the signal-to-noise, the carrier trapping in the organic coordinating matrix must be quenched. This also provided a motivation for alternative approaches in NC based devices: a) ligand replacement by chemical treatment, and b) the blended assembly approach.

4.2.2 Ligand Exchange – Chemically Treated Samples

As has been discussed (3.3.2.2), the substitution of long oleic acid molecules with shorter chain ligands will make the hopping distance of charge carriers between nanoparticles smaller, improving the charge transport within the NC assembly. The EDT and hydrazine treatment can be done for both PbSe and PbS NCs; however, due to the sensitivity of PbSe NCs which requires rigorous control of the environment, the chemical treatment was mainly attempted on the PbS NC assembly in this research. Drop-, slide-casting method, and dip-coating methods were used in this procedure, as was elaborated upon in the previous chapter (3.3.2.2).

Fig. 3.32 showed the highly variable surface morphology of PbS NC samples due to the shrinkage of NC assembly when treated by EDT, the effect of which is a lack of consistent electrical behavior over the sample region, which is illustrated in Fig. 4.21. The PbS NC was drop-cast on a gold-deposited glass substrate, topped with an indium contact, however, due to the poor quality of the assembly, the indium contact was not very consistent or reliable even upon visual inspection. I-V curves obtained from multiple regions exhibited diverse behavior, of which two examples were plotted.

Fig. 4.22 shows I-V curves obtained from a slide-cast PbS NC assembly deposited layer-by-layer (LBL) for 50 layers with the EDT treatment, and then covered by 20 layers modified by the hydrazine treatment. The assembly was deposited on a gold-evaporated glass-based substrate, topped with an aluminum contact. In contrast to the drop-cast sample, the surface looked smooth and even. Before destroying the sample to take a cross-sectional image with the SEM, the sample was investigated for its electrical behavior and radiation response. However, the thickness of overall assembly is estimated to be $\sim$50 μm considering that the PbS NC sample shown in Fig. 3.33, which consists of 10 layers of EDT and 10 layers of hydrazine treatment provided $\sim$15 μm thick layer assembly. Thus, we expect this sample to fully stop the

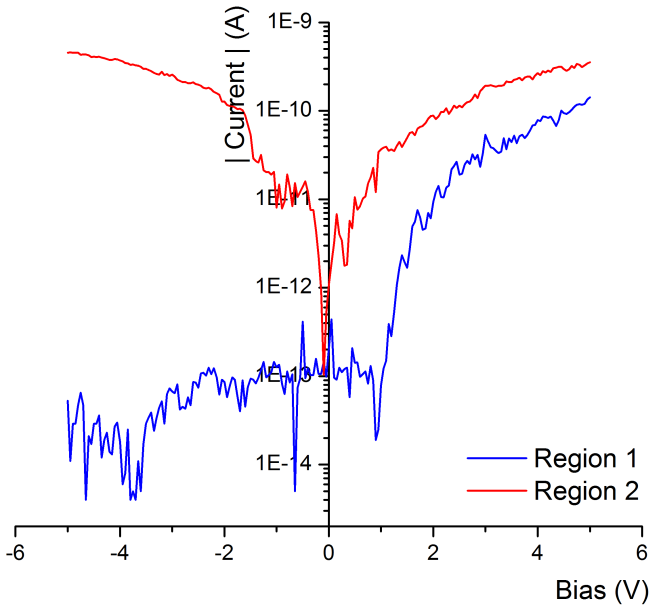

Figure 4.21: I-V curves of drop-cast PbS NC assembly deposited on gold-evaporated glass slides with EDT treatments between each drop, investigated at two different regions.

alpha particle within the NC assembly.

Fig. 4.22(a) shows the I-V curves of the PbS NC sample investigated at two different locations in the range of ±20 V. Notably, there is a rapid increase of the current after 15 V, and the response is different for the two areas. The reason for this is considered to be macroscopic inhomogeneity of the sample. Even though slide-cast samples look smooth upon visual inspection, the quality of the assembly is not ideal, as one can tell from the SEM images (Fig. 3.33) from the last chapter. There still exist boundaries between layers and internal cracks, which prevents an efficient charge transport throughout the assembly.

If a close look is taken at the I-V curve, there is no significant difference between the two I-V curves in the range of ±10 V, as shown in Fig. 4.22(b). The curve shows resistive behavior with slight space charge limited effect. At least in the lower bias region, the PbS NC sample has a more or less consistent behavior over the entire region.

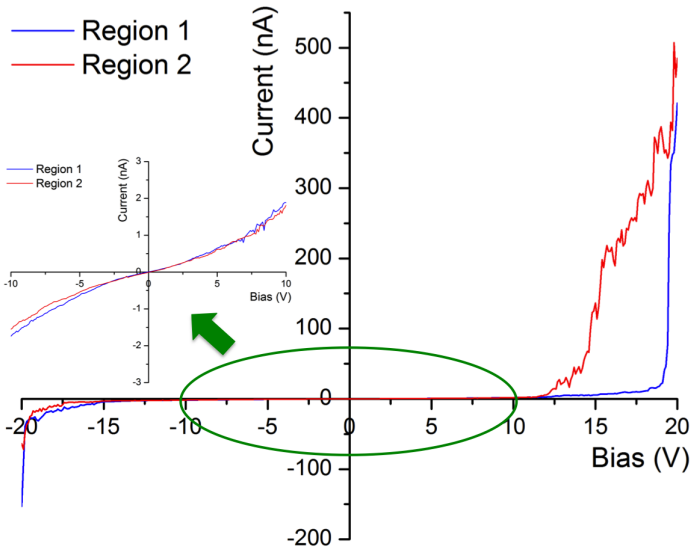

Figure 4.22: I-V curves of slide-cast sample with 50 layers of EDT treatment and 20 layers of hydrazine sandwiched by Al and Au contact.

The sample was then tested for the alpha particle response. The PbS NC sample with EDT and hydrazine treatments as described above, was tested at different bias settings. Up to ∼200 V, it was hard to distinguish the pulse signal from the inherent fluctuation of the system noise. Starting from ∼200 V, one could distinguish the different pulses due to radiation impact. The signal-to-noise ratio increases as one applies higher bias on the sample, as one can tell from the preamplifier signals shown in Fig. 4.23. Note that the signal-to-noise ratio increases as higher bias was applied. The alpha particle response was also investigated by collecting the pulse height spectra as shown in Fig. 4.24. The pulse height caused by alpha particle increases as the applied bias increases (Fig. 4.24). However, it saturates at ∼800 V, and further increases in the bias only induces more background competition. The background spectra shown in Fig. 4.24(a) is measured at 1000 V bias applied on the sample.

Fig. 4.24 shows the alpha spectrum collected at 1000 V as one varies the shaping time of the amplifier. One would prefer to have a shaping time that is similar to the rise time of the preamplifier signal shown in Fig. 4.23. A shorter shaping time than the rise time will not integrate the full energy absorption, causing a ballistic deficit.

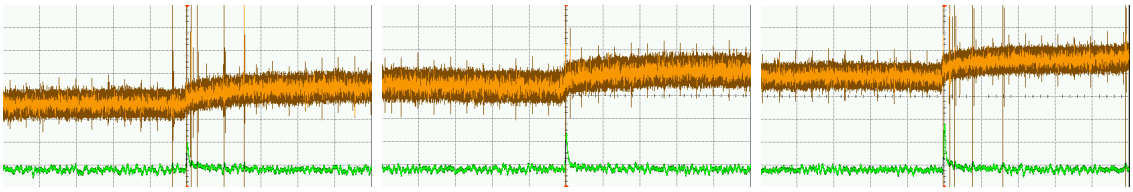

(a) (b) (c)

Figure 4.23: Preamplifier (yellow) and amplifier (green) signal from the PbS NC assembly sample described above, induced by the alpha particle emitted from Am-241 source. Equipment settings were at: fine gain 1.5, coarse gain 1000, shaping time 1 μs, and bias (a) 250 V, (b) 400 V, and (c) 600 V. Note that the preamplifier signal amplitude increases and the rise time becomes shorter as one increases the bias. Time scale is 50μs per division and the voltage scale is 5 mV and 500 mV per division for yellow and green.

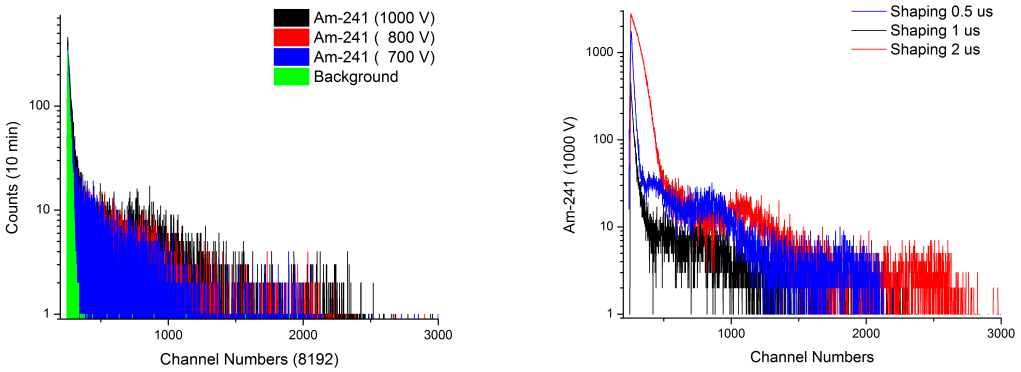

(a) (b)

Figure 4.24: Pulse height spectra acquired from the PbS NC sample described above, responding to the incident alpha particles emitted from the Am-241 source. (a) Bias applied to the sample was varied, from 700 V to 1000 V. The background shows the pulse height distribution of background noise fluctuations at 1000 V bias setup. (b) At 1000 V bias setting, the shaping time of the amplifier was varied. One can expect the system is picking up more noise by integrating the pulse signal over longer shaping time.

Meanwhile, pulses derived from long shaping times will be adulterated by unnecessary noise fluctuations into the shaped pulse. Even though the maximum signal pulse is larger for the 1 μs and 2 μs shaping times because of the lengthy rise times of the preamp pulses, further measurement was based on the 0.5 μs shaping time in order to reduce the contribution from the noise response and to enhance the signal-to-noise ratio.

Therefore, alpha spectrum from Am-241 was collected at 1000 V with 0.5 μs shaping time. The fine and coarse gain was 1.5 and 1000, respectively. The spectrum was collected using an MCA-8000A (Pocket MCA) from Amptek with a voltage range of 5 V. Fig. 4.25 shows alpha spectrum collected from the PbS NC sample for 10 minutes, followed by 10 minute background measurement. The kinetic energy of the incident alpha particle is estimated to be $\sim$3.6 $\pm$ 0.1 MeV from the SRIM/TRIM simulation above (4.1.2.1), as the same test box was used to test the NC sample. Since the 10 minute measurement shows limited features in the spectrum with very poor statistics, we collected the spectrum for 1 hour.

As shown in Fig. 4.25(b) a one hour measurement of the alpha-induced distribution reveals three peaks connected by the continuum. The peak on the highest channel is expected to correspond to those regions of the sample for which charge carriers are created most efficiently and maximally transferred to the electrode. Peaks in the lower channels may correspond to less efficient but still highly probable routes of charge carriers in which a significant portion is trapped and lost along the path. If there is a major crack or separation between layers and the alpha particle interacts in that region, the alpha particle may deposit only part of its energy in the active region. Continuums are due to the broad source distribution as well as varying regions of charge loss in the sample.

The response to gamma rays were also studied, using Ba-133, Na-22 and Co-60 sources. Fig. 4.26 shows the response of the PbS NC assembly to the gamma sources

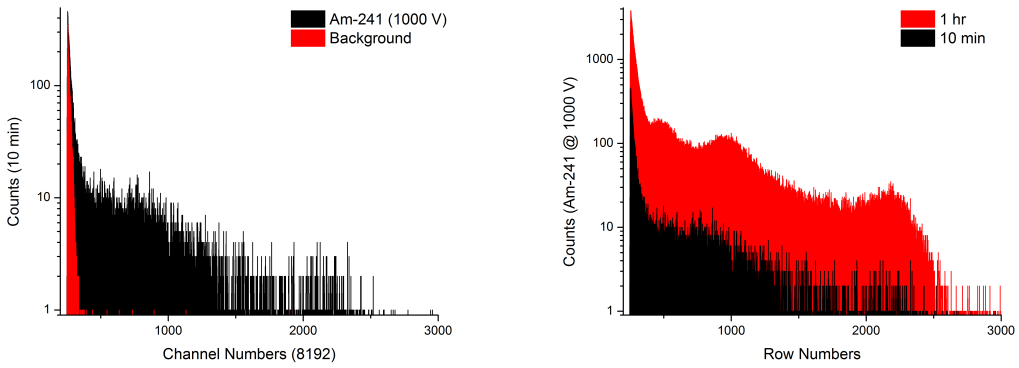

(a) (b)

Figure 4.25: Alpha spectra collected with an MCA compared with the background noise distribution. The spectrum was measured for (a) 10 min. and (b) 1 hour in comparison with the 10 min. spectrum.

compared with the background spectrum. First the spectrum was measured with Ba-133 and Na-22 sources on the box, to provide low energy gammas (Ba-133, less than 400 keV), intermediate and high energy gammas (Na-22, 511 keV and 1274 keV). One can observe that the count rate increases over the background area (Fig. 4.26(a)). However, it was hard to distinguish the main features of the gamma ray spectrum because the poor charge conversion results in a low SNR. The spectrum was measured for 4 days with Co-60 sources (Fig. 4.26(b)) in order to maximize the number charge carriers created from an interaction that may contribute to the signal, but again, the small integrated charge results in indistinct features.

The next sample is another PbS NC sample made by dip-coating 50 layers with the hydrazine treatment in between. The assembly was deposited on a platinum evaporated glass substrate (Appendix B), topped with an indium contact. For up to 50 layers the surface quality of the film was not seriously compromised; thus, the surface looked smooth. Fig. 4.27 shows the preamplifier (yellow) and shaping amplifier (green) responses of the NC assembly to alpha particles from Am-241 source at different biases. The waveforms were obtained at 380 V, 500 V and 700 V. The

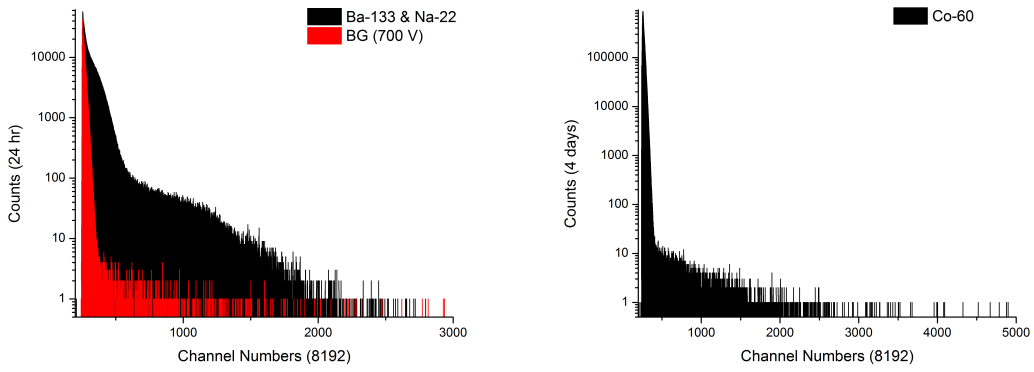

(a) (b)

Figure 4.26: Gamma ray spectrum collected for the PbS NC sample for (a) Ba-133 and Na-22 sources collected for 24 hours and (b) Co-60 source collected for 4 days.

time scale is the same 50 μs, and the voltage scale was 5 mV and 500 mV per division[3] for preamplifier and shaping amplifier signals respectively. As expected, the signal rise time decreases as the bias increases, which makes the 1 μs shaped pulse larger and more easily distinguishable.

Fig. 4.28 shows the alpha spectrum obtained from the PbS NC sample dip-coated 50 times with hydrazine treatment in between. Measured at 500 V, one could easily distinguish the pulse signal induced by the alpha particles. Increasing the bias up to 700 V increased the overall pulse height distribution to higher channels. In addition, at 700 V, the spectrum revealed another peak which was concealed in the background noise at the lower bias, likely due to a distribution from an inefficient region in the assembly.

Compared with the drop-cast samples, the slide-cast assemblies and dip-coated assemblies by LBL deposition with chemical treatment enhanced the charge carrier transport; thus, one can see responses from the alpha particle. However, one can observe that either the charge creation is poor or the trapping is dominant, as indicated by the amplitude of the preamplifier signal, which is ~5 mV at optimal operating

[3]The voltage scale was 5 mV and 1 V per division in Fig. 4.27(c)

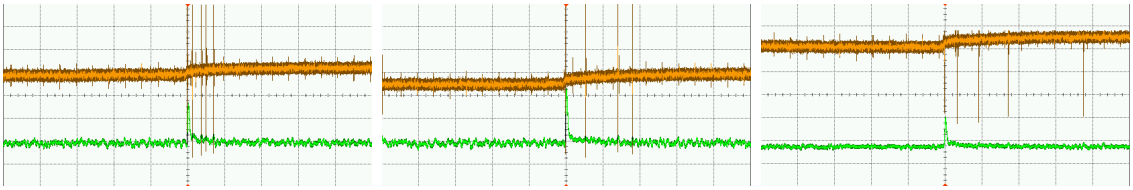

(a) (b) (c)

Figure 4.27: Preamplifier (yellow) and amplifier (green) signal from the dip-coated PbS NC assembly with hydrazine treatment, induced by the alpha particle emitted from Am-241 source. Equipment settings were at: fine gain 1.5, coarse gain 1000, shaping time 1 μs, and bias (a) 380 V, (b) 500 V, and (c) 700 V. Note that the preamplifier signal amplitude increases and the rise time becomes shorter as one increases the bias. Time scale is 50μs per division and the voltage scale is 5 mV and 500 mV per division for yellow and green.

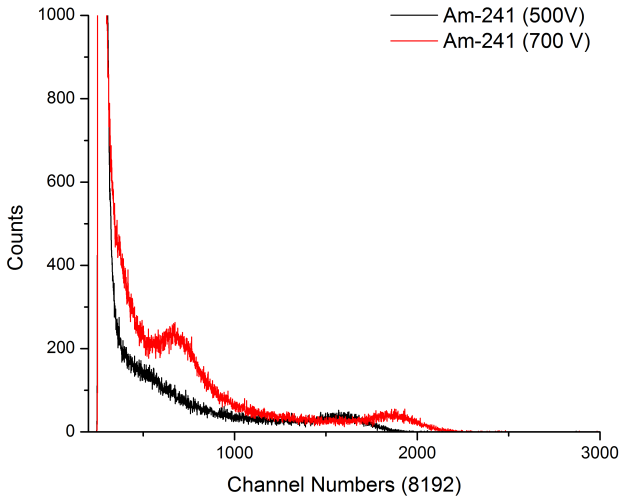

Figure 4.28: Dip-coated sample with 50 layers of PbS NC with hydrazine treatment sandwiched by Pt and In contact.

conditions. Furthermore, the LBL method, as has been mentioned, has drawbacks of lengthy fabrication and processing time and deterioration of the film quality for thick samples. Making a macroscopic thick layer via ligand exchange with chemical treatment therefore still requires an optimization in both the device processing and charge transport properties.

4.2.3 Blended Assembly of NC/Polymer Composite

As has been discussed previously, as an effort to enhance the charge transport behavior of NC assemblies, the blended structure approach with conductive polymers was investigated. Even though using a conjugate polymer introduces another medium between the NCs, and another potential source of charge loss, the processing methods are more conducive to creating a homogeneous film without visible cracks at the macroscopic scale. Moreover, inducing a conjugate polymer will reduce the density of the assembly. We haven't discussed in this research the application of NC assemblies to fast neutron detection, which takes advantage of low atomic number elements to induce head on collisions with incident neutrons.

The successful application of one batch of the polymer-coordinated detectors is summarized in Fig. 4.29. Note that the detector yield was 55% for this early batch, in the sense that 5 out of 9 detectors were capable of clear 5.485 MeV alpha-particle detection. Furthermore, note that the response was declared weak, as explained below, for the drop-cast samples, but the one spin-cast sample examined produced an excellent detector.

Specifically for the drop-cast samples, a weak-response was one for which the induced charge signal was small enough that thermal and leakage-current noise substantially impacted the conversion of the radiation to voltage pulses. Some example waveforms for drop-cast sample #2 (10 nm spherical NCs drop cast with Au/In electrodes) are shown in Fig. 4.30, in which the preamplified signal in yellow is derived

(a)

SampleID	NC ID#	NC size	NC shape	Polymer	Deposition Method	Contact	Suggested Bias (V)	Etc
① Via	0528	8 nm	sphere	X	Drop-cast	Al / Au	0 – 2	
② 1-3	07271	10 nm	Sphere	O	Drop-cast	Au / In	30-50	
③ 1-7	07271	10 nm	Sphere	O	Spin-cast	Au / Au	.....	
④ 1-5	07271	10 nm	Sphere	O	Drop-cast	Au / In	Upto 200	
⑤ 2-2	0925	25 nm	Star	O	Drop-cast	Au / Au	0-10	
⑥ 2-4	0926	12 nm	Star	O	Drop-cast	Au / Au	0-5	PL 1650 nm
⑦ 2-6	0927	18 nm	Star	O	Drop-cast	Au / Au	0-5	Middle point
⑧ 2-8	0928	?	?	O	Drop-cast	Au / Au	20-30	Good sample
⑨ 1-1	07271	10 nm	Sphere	O	Drop-cast	Au / Al	Up to 100	Good solar Cell

- **no response, low noise**
- **weak α response, low noise**
- **strong α response, high noise**
- **weak α response, low noise**
- **weak α response, high noise**
- **weak α response, high noise**
- **no response, high noise**
- **no response, high noise**
- **no response, high noise**

(b)

Figure 4.29: (a) Photograph and layout for the detectors in a tray. (b) The NC size and shape, as well as the contacting geometry, for the nine detectors, as well as a subjective assessment of their radiation-detection properties (on the right).

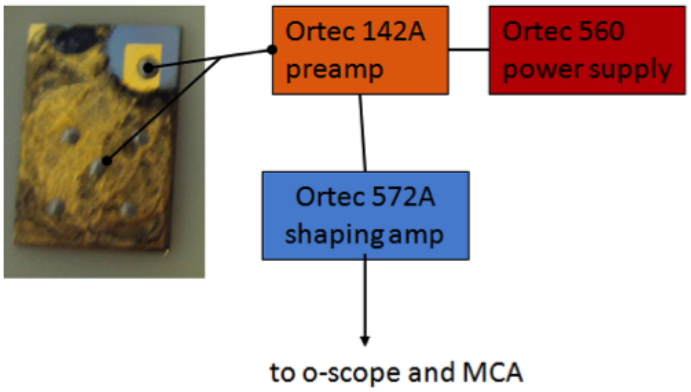

(a)

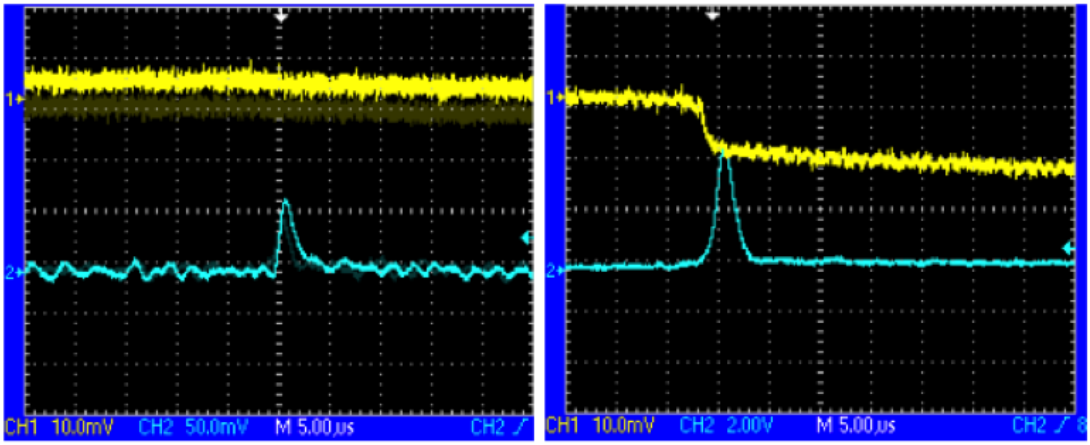

(b)

Figure 4.30: (a) Schematic of electronic signal processing chain. (b) Resulting preamplifier (in yellow) and shaping amplifier (in blue) waveforms as derived from a drop-cast sample of 10 nm PbSe spherical NCs. Note that in the right side blue waveforms, the shaping amplifier gain was increased from 100 to 1500 (reduced vertical scale 20 mV per division to 2 V per division).

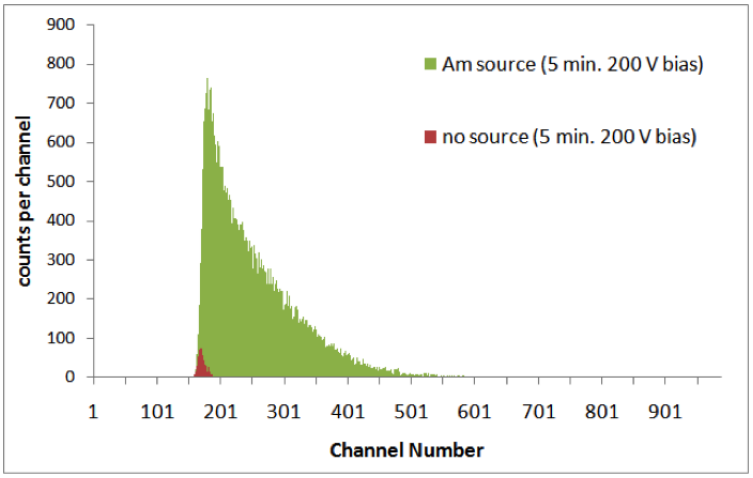

Figure 4.31: Pulse height spectrum obtained from "weak-response" samples, with and without an Am-241 alpha source present, in which the gain on the shaping amplifier was 1500 and the shaping time was 0.5 μs.

from an ORTEC 142A preamplifier, and the blue signal corresponds to the pulse after amplification through a shaping amplifier (ORTEC 572A). Note that the detector response, as measured via the preamp signal, is rather weak and indistinguishable from the noise for bias voltages less than 100 V. However, as the bias is increased to several hundred volts, then the signals are not only distinct from the noise (cf. Fig. 4.30(b)), but two distinct modes of transport are evident, presumably due to rapid electron transport accompanied by more deliberate hole motion. Although the radiation signals are clearly evident, the noise remains substantial compared with the signal, as clarified in the alpha particle-induced pulse height distribution, shown in Fig. 4.31.

The measurement results thus indicate that although the drop cast samples can detect radiation, the signal-to-noise ratio is limited. For the samples of Fig. 4.29, the signal-to-noise ratio was excellent for the spin-cast sample, and we therefore transitioned to spun-cast detectors. After sampling 27 detectors however, we found that spin-casting alone did not result in a high-yield of excellent detectors. For instance, Fig. 4.32 shows the detector summary for a tray of spin-cast detectors, in which we again find that one can readily extract radiation-induced pulses from roughly

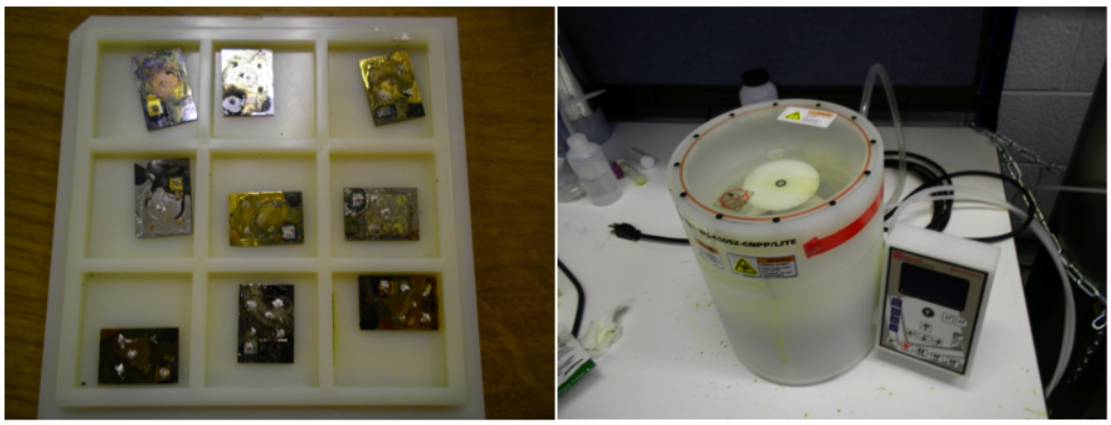

(a)

Smpl ID	NC ID#	NC size	NC shape	Polymer	Deposition Method	Contact	Amount	
	0724	5 nm	Sphere	O	Spin-cast	Au / Al	20 u X 10	-shorted
②	0724	5 nm	Sphere	O	Spin-cast	In / In	20 u X 5	
③	0926	12 nm	Star	O	Spin-cast	In / Au	20 u X 10	- strong α response, low noise
④	0724	5 nm	Sphere	O	Spin-cast	Au / In	20 u X 10	- weak α response, low noise
⑤	0724	5 nm	Sphere	O	Spin-cast	In / Au	20 u X 10	- weak α response, low noise
⑥	0926	12 nm	Star	O	Spin-cast	In / Pt	20 u X 10	
⑦	0724	5 nm	Sphere	O	Spin-cast	Au / Au	20 u X 10	
⑧	0724	5 nm	Sphere	O	Spin-cast	In / Pt	20 u X 10	
⑨	0926	12 nm	Star	O	Spin-cast	Au / Au	20 u X 10	=> 50 % detector yield

(b)

Figure 4.32: (a) Photograph and layout for the detectors in a spin-cast sample tray, as well as the spinner used to cast the samples. (b) The NC size and shape, as well as the contacting geometry, for the nine detectors, as well as a subjective assessment of their radiation-detection properties (on the right).

half of the detectors, and 11% of the detectors provide excellent characteristics.

Fig. 4.33 summarizes that pulse-height distribution from a detector with a weak alpha particle response, in which the alpha particle peak is indicated by the broad hump to the right, which must compete with the noise shown in the figure. By counting the number of pulses under the distribution, we estimated the effective area of the detector, given the known geometry, the source strength (0.1 μCi Po-210 source), and the accumulation period, and found that the count rate was consistent with a 1 cm^2 area. Thus, we successfully made detectors in which the entire deposited area is active, in this case the entire 1 cm^2.

The difference between good and bad detectors can be appreciated by examining

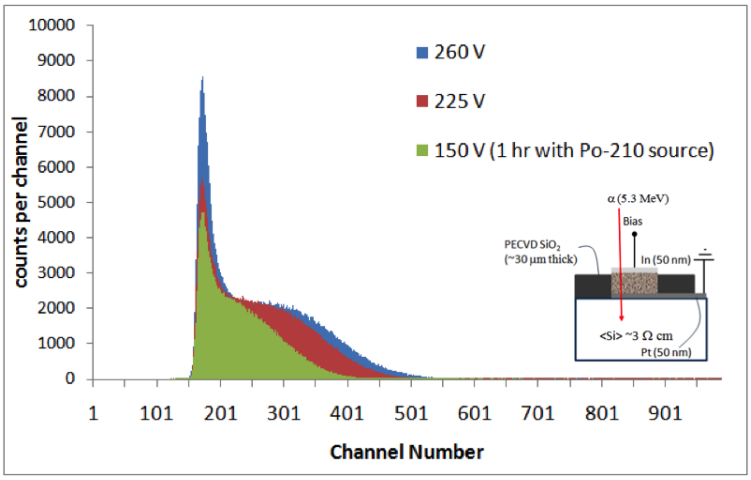

Figure 4.33: For the geometry in the inset, the pulse height distribution of an Am-241 alpha source at various bias voltages, in which the gain on the shaping amplifier was 100 and the shaping time was 0.5 μs.

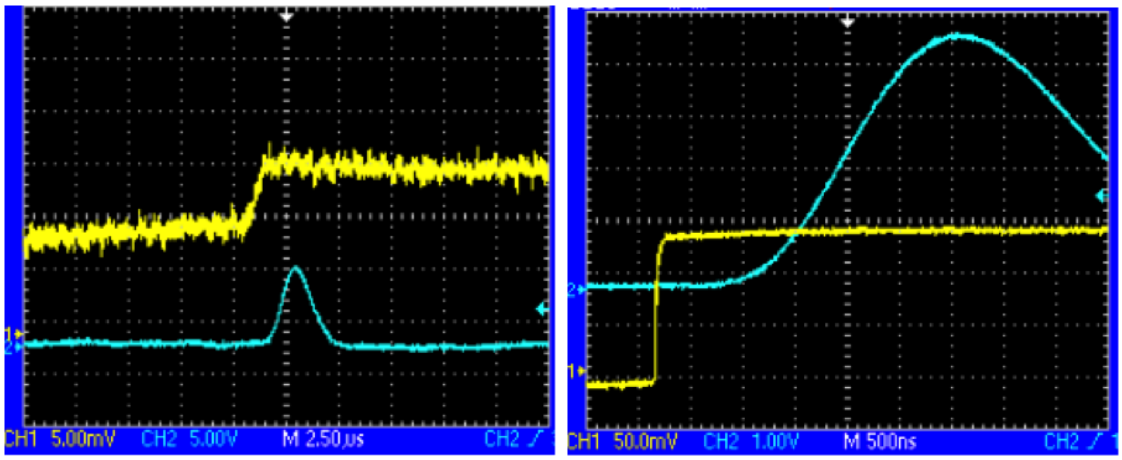

(a) (b)

Figure 4.34: Comparison of the preamplifier and the shaping amplifier waveforms obtained from two different spin-cast NC blended composites: (a) an example of "weak" response detector and (b) excellent detector.

the waveforms shown in Fig. 4.34. The pulses in Fig. 4.34(a) correspond to the spun-cast sample examined in Fig. 4.33, which produces a discernible distribution from the small, 5 mV (preamplifier) pulses shown. However, if the same alpha particle impacts an excellent detector, than the pulses, shown in Fig. 4.34(b), are sharper ($\sim$200 ns rise time) and much bigger (140 mV), reflecting excellent charge conversion and transport. In fact, the pulses are superior to those that we detect with conventional semiconductor materials, CZT and Si. We will examine the characteristics of these detectors next.

Although blends of conductive polymers and NCs have lost favor for solar-cell applications because of relatively poor charge-transport characteristics, we find acceptable mobility, as indicated in the relatively rapid pulse rise of the NC PbSe detector of Fig. 4.35, and more importantly, negligible trapping effects. Trapping can reveal itself either in: a) the induced-charge pulse shape- through slope variations that correspond to the removal of charges from the drift stream, or b) via low-energy tailing of the gamma-ray peaks due to diminished charge collection at increasing interaction depths. As indicated in the pulse shapes and in the gamma-ray spectra in Section 3, neither manifestation of charge trapping is evident.

Fig. 4.36(a) shows the general configuration of a 1 cm$\times$1 cm detector, in which a colloidal dispersion of spherical 7.4 nm PbSe nanoparticles are cast with an interstitial polymer. Note that although the isolating oxide is only 30 μm thick, the active PbSe colloidal solid was several hundred micrometers thick. The pulse height distributions, or energy spectra that result are shown in Fig. 4.36(d). As reflected in the black pulse trace of Fig. 4.35, the signals are sharp and clean above the background, yielding the black energy distribution in Fig. 4.36(d), which is collected when the detector is exposed to alpha particles from an Am-241 source, which emits a 5.486 MeV alpha particle (85% yield) as well as a 5.443 MeV alpha particle (13% yield). Thus, the peak corresponds principally to the deposition of 5.486 MeV of energy in

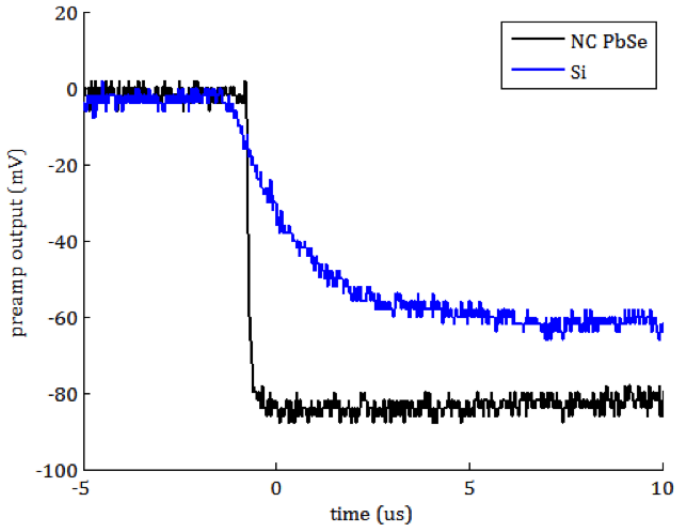

Figure 4.35: The pulse shape derived from the charge-sensitive preamplifier (ORTEC 142A) when an alpha particle from Am-241 is incident upon a silicon PIN or NC PbSe detector, both operated at 0 V applied bias. The PbSe nanoparticles are spherical with a mean diameter of 7.4 nm (± 0.5 nm).

the detector, broadened not by the detector characteristics but by the thickness and nonuniformity of the button alpha-source. In fact, in comparing the shape with that derived from a silicon surface barrier detector, the fabrication of which is described in M. Jeong *et al.*[115], the resolution is comparable to or superior, which implies that the conductive polymers are not only accomplishing the goal of realizing good charge transport through the device, but they are not substantially participating in the charge loss of the secondary electrons.

As shown in the (yellow) pulse shape in Fig. 4.36(c), the signals are sharp and clean above the background, yielding the black energy distribution in Fig. 4.36(d), which is collected when the detector is irradiated by alpha particles. In fact, the energy resolving behavior is quite impressive because when it is compared with a highly engineered silicon surface barrier detector (see the blue distribution in Fig. 4.36(d)), the resolution is superior and the signals are bigger. The counts per bin from the NC PbSe distribution are multiplied by 6.5 in order to facilitate shape comparisons. The

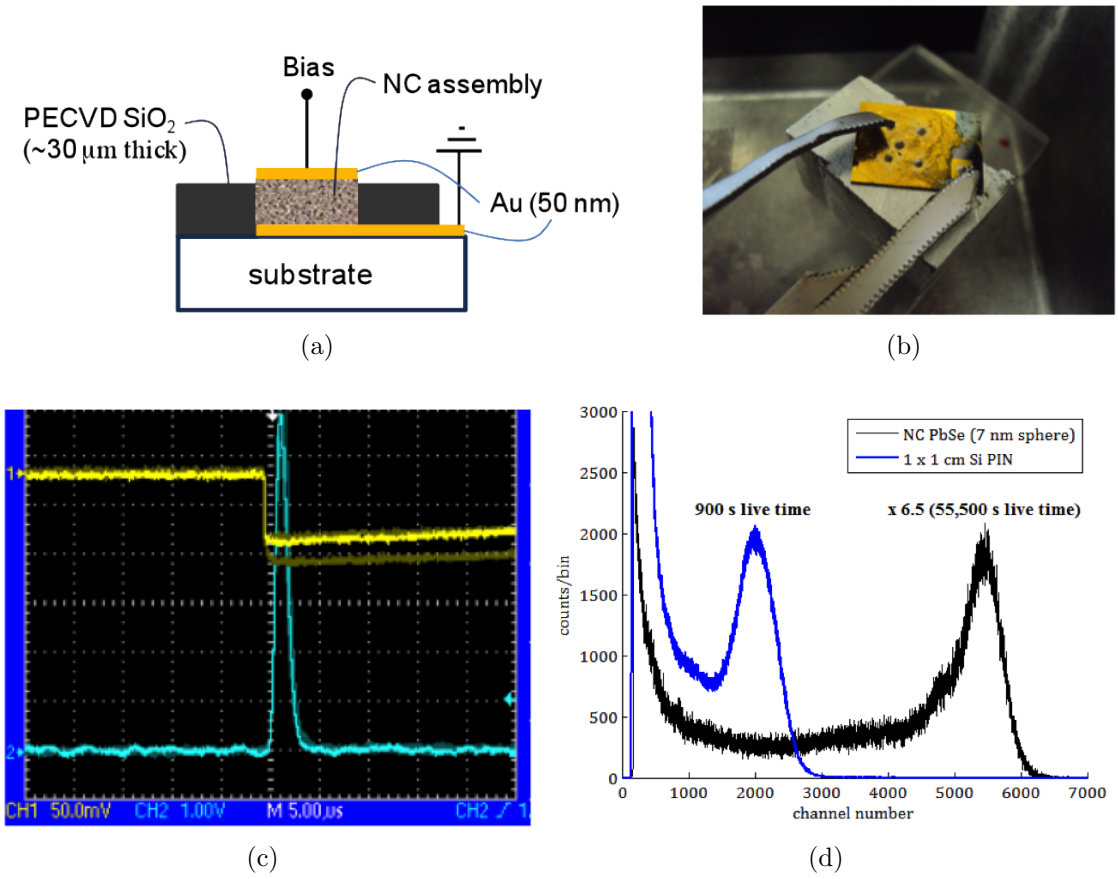

Figure 4.36: (a) Schematic diagram of radiation-detector device geometry, in which NC assembly is sandwiched between metal contacts (Au on both anode and cathode sides in this case). (b) The realized device, in which the NC solid thickness was several hundred micrometers. (c) Typical pre-amp pulse, in yellow, as measured with an ORTEC 142A preamp, and shaped pulse, in blue, as derived from the detector biased at 0 V operating at room temperature. (d)Comparison of the pulse height distributions from the PbSe NC assembly and a 1×1 cm^2 silicon surface-barrier detector. The counts per bin from the NC PbSe distribution are multiplied by 6.5, in order to facilitate shape comparisons. The duration of the silicon measurement was 900 s and that of the NC PbSe was 55,500 s (15.4 h), reflecting the small effective area of the detector.

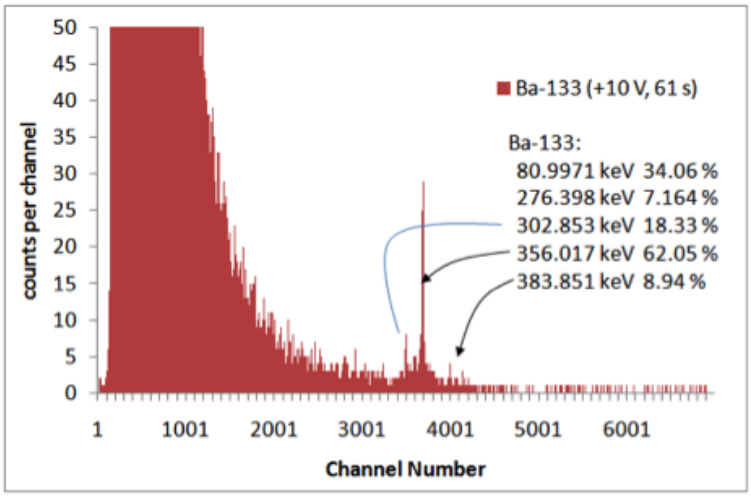

Figure 4.37: The gamma-ray spectrum derived from a Ba-133 source.

duration of the silicon measurement was 900 s and that of the NC PbSe was 55,500 s (15.4 h), reflecting the small effective area of the detector.

This is confirmed in the gamma-ray spectrum derived from a Ba-133 source, shown in Fig. 4.37, in which the peaks are resolved with HPGe-scale accuracy. Specifically, we achieved an energy resolution of 0.16% at a gamma-ray energy of 356 keV (from Ba-133). Furthermore, this result was achieved at room temperature, with a chemical solution fabrication methodology that allows one to deposit the active material across large areas at atmospheric pressure using standard wet-chemistry techniques. This rather remarkable result implies that the conductive polymers are not only accomplishing the goal of realizing good charge transport through the device, but they are not substantially participating in the charge loss of the recoil electrons.

That is, it isn't particularly surprising that the inherent energy resolution of the PbSe nanoparticles is fine, since the mean band-gap is 0.63 eV ($\pm$ 0.03 eV); however, the fact that the conductive polymer does not substantially induce deterioration in the charge creation and transport behavior implies that the colloidal PbsSe-solid is comparable to or superior to existing single-crystal materials. The two remaining challenges can be gleaned from Fig. 4.36(d), which shows: (1) that greater measure-

ment periods were needed to accumulate the NC spectrum due to the relatively small size of the active area, and (2) the thermal noise was large enough that the measurement of the small energy depositions that accompany gamma-ray interactions were partially obscured. As shown in Fig. 4.41, we were able to overcome these challenges by utilizing smaller confinement structures and more uniform deposition conditions.

The spectra of Fig. 4.36(d) show that a fine conversion of energy to charge carriers is elicited in the NC assembly. Fig. 4.38 shows that the transport is also rapid. Specifically, in the figure we compare the waveforms from a PbSe NC detector with those from a well engineered silicon PIN detector, both operated at zero bias at room temperature. The much faster rise time (200 ns for PbSe vs. 7 μs for Si) reflects a combination of a narrower charge distribution (for PbSe) as well as a faster drift velocity,[4] as driven by the electric field and the mobility in the solid, reflecting that the charge creation and collection is excellent. The waveforms also reflect the differences in the count rates between the detectors, each of which has a fabricated area of 1 cm^2 – note that greater number of pulses during the oscilloscope accumulation period. The fact that the Si count rate is 394 times the PbSe count rate implies that the active area of the PbSe detector is only 0.25 mm^2 (= 500 μm$\times$500 μm). This is expected at the early development stage ($\sim$2008) because during deposition, there are domains of packing-uniformity separated by cracks, and the behavior reflects the superior behavior of one of those domains. In fact, the dual nature of the detectors- excellent performance over some sub-section of the detector and moderate performance over the rest of the detector, was demonstrated explicitly in certain detectors, an example of which is shown in Fig. 4.39.

Fig. 4.39 shows the detector, which is comprised of spun-cast 12 nm star-shaped NCs with conductive polymer and bound by In/Au contacts. Fig. 4.39 shows two classes of pulses which then translate into two features on the pulse height distribu-

[4]For this particular sample, the thickness of the blended NC assembly was comparable to the thickness of a silicon wafer, i.e., a few hundred micrometers.

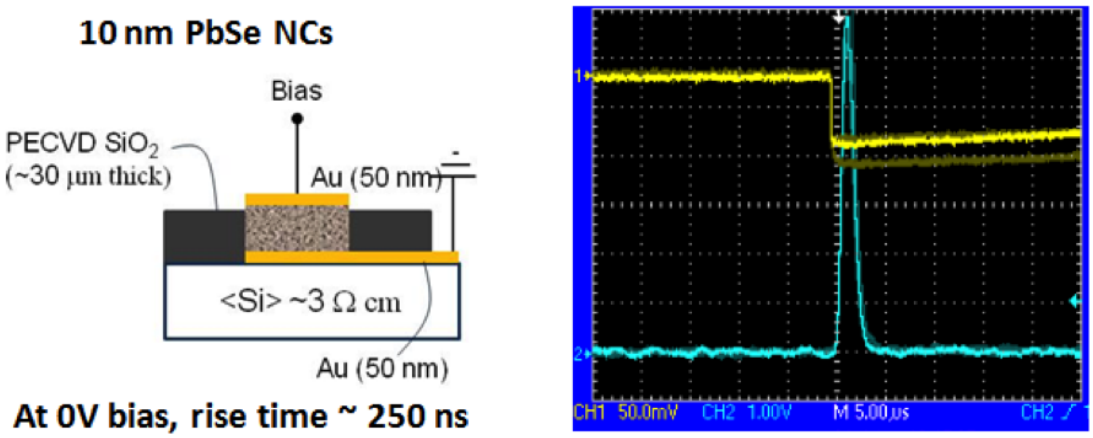

(a)

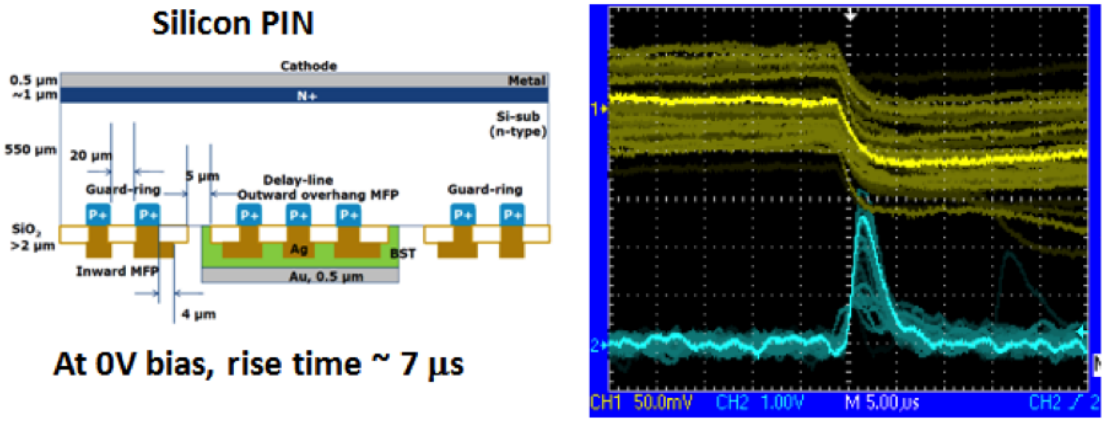

(b)

Figure 4.38: The pulse shape derived from the charge-sensitive preamplifier (ORTEC 142A) when an alpha particle from Am-241 is impinged upon (a) a silicon PIN or (b) NC PbSe detector, both operated at 0 V applied bias. The PbSe nanoparticles are spherical with a mean diameter of 7.4 nm (± 0.5 nm).

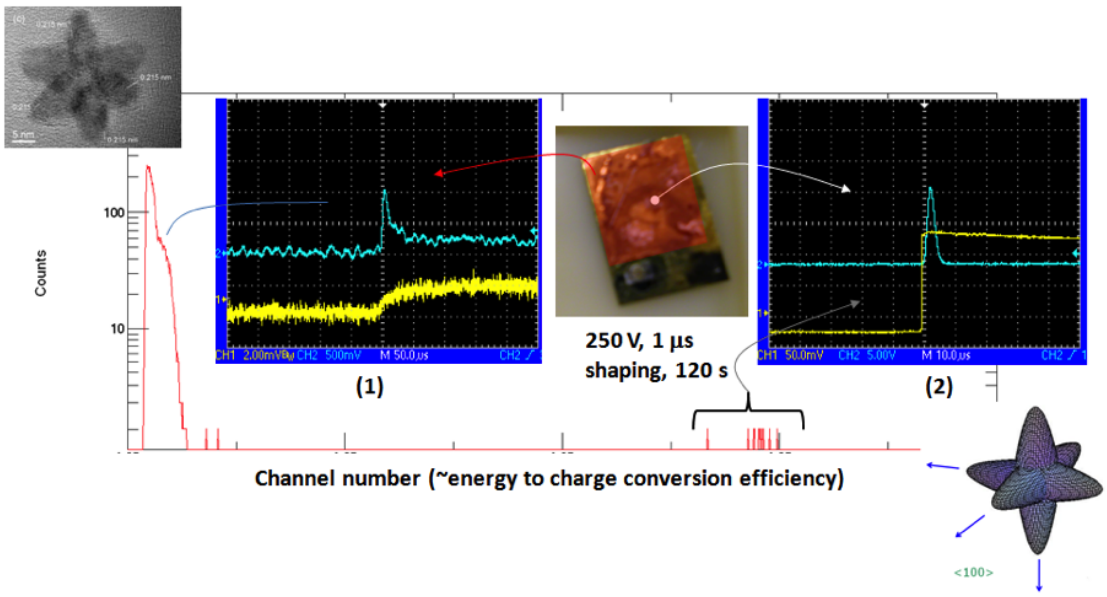

Figure 4.39: For a 12 nm star-shpaed PbSe NC detector biased at 250 V, the pulse height distribution and typical pulses contributing to the features. The detector is also pictured as well as a TEM micrograph and model of the star-shaped particles.

tion. First, there is a high rate of small (∼2 mV) slow (∼100 ms) pulses, indicating that most of detector works with low mobility and limited conversion efficiency. At higher channel numbers there is a small amount of large (150 mV) and fast (200 ns) pulses, which correspond to high mobility and good charge collection. If one increases the detector bias to voltages above 300 V, then the entire detector exhibits excellent charge collection in the form of sharp large pulses; however, the noise intrudes after a short duration of operation (10's of seconds). The source of this instability is currently under investigation, and must be resolved because it can impair detector performance if spectra are accumulated over long periods. For instance, Fig. 4.40 shows the pulse height distribution derived from a 10 nm sphere PbSe NC detector, in which a Cs-137 was placed in close proximity. Although the Cs-137 gamma-rays contributed to the distribution, the thermal noise entered into the distribution as a large background component.

Fig. 4.41(a) corresponds to a mixed spectrum derived from alpha particles- emerg-

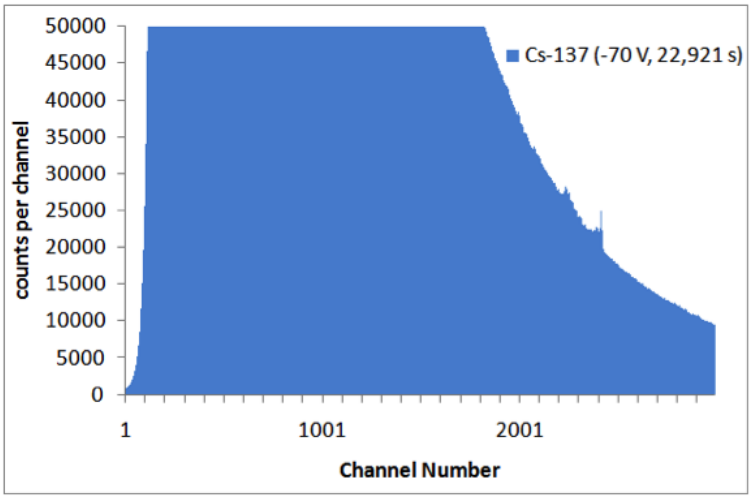

Figure 4.40: For a 10 nm sphere PbSe NC detector biased at -70 V, the pulse height distribution when irradiated by Cs-137 gamma source. The broad background is due to the leakage current fluctuation.

ing from a thin-film Am-241 alpha particle source and Ba-133 gamma-rays impinging upon the 1×1 cm^2 detector shown in Fig. 3.41. The alpha source, placed 3.7 cm away from the detector surface, attenuates the 5.49 MeV particles to the energy range shown, and the Ba-133 source was placed external to the box housing the detector, 5 cm distant. If one focuses on those spectral features whose appearance correlates to the presence of the Ba-133 source, then we can identify the features using both the pulse amplitude and the frequency of occurrence as follows.

Although the material need not be linear, the pulse amplitudes of the three full-energy gamma-ray peaks were linearly related to the energies identified in Fig. 4.41(b). Second, the areas under the spectral features correspond to the expected values. For instance, if one takes the gamma-ray emission yield as well as the photoelectric absorption probabilities into account, the area of the 383.85 keV peak should be 12% of that under the 356.02 keV peak, compared with a measured value of 11%. The sizes of the x-ray escape features diminish for thicker detectors; however, the thin detector was utilized to characterize the charge-creation characteristics, minimally adulterated by charge-loss considerations, so that W and the inherent energy resolution can be

better estimated.

Fig. 4.42 shows the spectral widths compared with three state-of-art detectors, all operated at room temperature except for the high purity germanium (HPGe) detector, which was cooled with liquid nitrogen, noting that although they are state-of-the art detectors of typical volumes, the Si and CZT comparison-spectra don't represent the ultimate material limit- one can cool the silicon and use a smaller volume of high-quality CZT, for instance. The 1×1 cm^2 detector was fully depleted across the 550 μm thickness and biased at +100 V. The coaxial HPGe detector (GEMPM45P4-108: 84.7 mm diameter$\times$32.8 mm length) was operated at a bias of +3800 V, and the spectrum was accumulated over a 24 hour period, thus accounting for the relative smoothness of the curve compared to the PbSe-equivalent. The $2\times2\times1.5$ cm^3 $Cd_{0.9}Zn_{0.1}Te$ (CZT) detector uses a gridded array of 11×11 pixels to realize single-polarity charge sensing via the small pixel effect, and depth correction is used to compensate for non-uniform electron trapping [116]. As shown in Fig. 4.36 above, nanostructured detectors can yield a sizable built-in voltage due to the metal-semiconductor interface alone and can be operated at low bias voltages; however, the particular NC PbSe detector used in Fig. 4.42 was resistive and operated at a bias of +320.3 V.

As shown in Figs. 4.42(a) and 4.42(b), the energy resolution of the PbSe nanocomposite is superior to silicon and CZT and comparable to HPGe, yielding an energy resolution of 0.42% (1.5 keV) at 356 keV, compared with a resolution of 0.96% (3.4 keV) for CZT and 0.39% (1.4 keV) for HPGe. Fig. 4.42(c) shows an equivalent comparison between the detectors when impinged upon by 661.7 keV gamma-rays from Cs-137. The Cs-137 source was more than one hundred times less intense than the Ba-133 source and the peak was therefore less well sampled. More importantly, the slight gain drift in the detector, as described later, dominated the peak width shown in the figure. Nevertheless, the Cs-137 results buttress those derived from Ba-133 gamma-rays; namely, the nanocomposite detector provides an energy estimate with

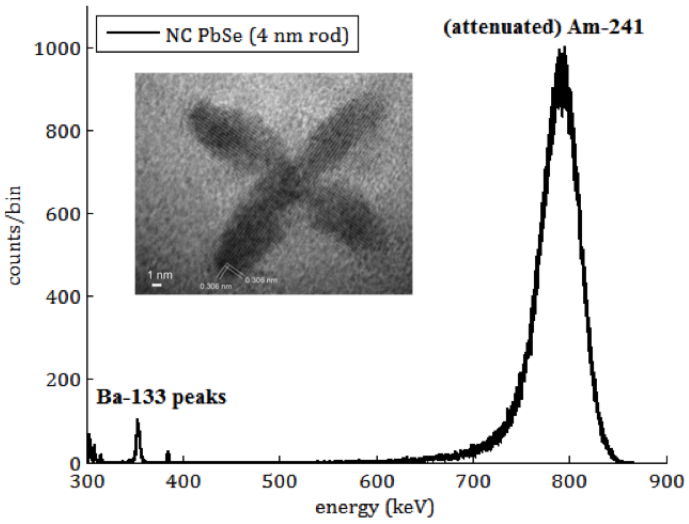

(a)

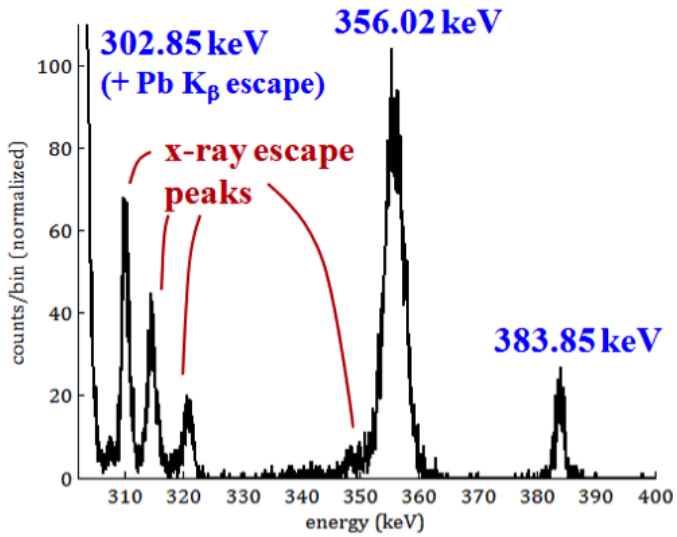

(b)

Figure 4.41: (A) Energy spectrum derived from Ba-133 gamma-rays and Am-241 alpha particles, attenuated through 3.7 cm of air, impinging upon a 1×1 cm^2 detector comprised of a 22 μm thick composite assembly of para-MEH-PPV and star-shaped PbSe nanopartiles, accumulated for a duration of 900 s. The inset shows a TEM micrograph of a typical PbSe NC in the assembly. (B) Typical Ba-133 spectrum derived from a thin detector, in which the Pb and Se x-ray escape peaks are prominent.

similar fidelity to that produced by HPGe. Given the higher electronic noise associated with the preamplifier readout (ORTEC 142A for the NC PbSe compared with a cooled A257P for the HPGe), the intrinsic Fano noise of the nanostructured detector is thus superior to all of the single-crystal semiconductor detector media shown.

In order to fully realize the potential of lead-salt nanomaterials, one must optimize the design and synthesis of both the NC's and the overall solid and furthermore, gain a greater understanding of the non-idealities of the material shown below; namely, gain-instability. One might expect a priori that a nanostructured detector might exhibit non-linearity due to an energy-dependent variance in the charge multiplicity. For instance, if the charge multiplication probability is enhanced relative to phonon-assisted relaxation processes at higher (secondary) electron energies, then the calibration between induced-charge and energy might exhibit positive curvature. However, if a higher multiplicity of excitons is created in a NC at higher deposition energies, then negative curvature might result since the effective band-gap may increase as the lower-energy states are filled. Experimentally, we don't observe a significant curvature in the charge-to-energy conversion ($R^2 = 0.99996$).

The detectors can exhibit drift, which manifests itself as gain instability, as indicated in Fig. 4.43, in which the gap between the full-energy peak and the x-ray escape peak is filled in as the peak shifts as a function of time. Although the exact source of the instability is unknown, phenomenologically the shift is consistent with a variation in the detector capacitance because for those small (< 1 mm^2) detectors which have a negligible capacitance compared to the circuit capacitance, the spectral features are highly stable. For instance, the alpha particle spectrum of Fig. 4.36 could be collected indefinitely, and repeated months later and still exhibit reproducible behavior. Furthermore, variations in the capacitive area and width are not expected; thus, the observations imply that the gain instability is caused by variations in the effective permittivity of the medium, which is influenced by the creation and drift of charge

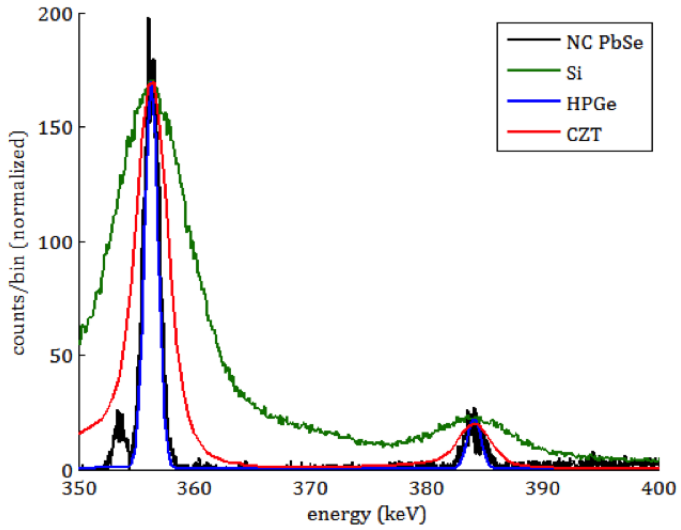
NC PbSe
Si
HPGe
CZT
counts/bin (normalized)
energy (keV)
0
50
100
150
200
350
360
370
380
390
400

(a)

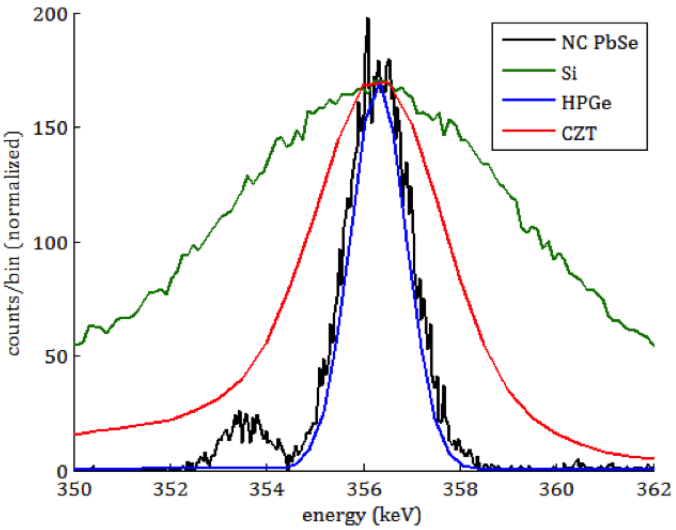
NC PbSe
Si
HPGe
CZT
counts/bin (normalized)
energy (keV)
0
50
100
150
200
350
352
354
356
358
360
362

(b)

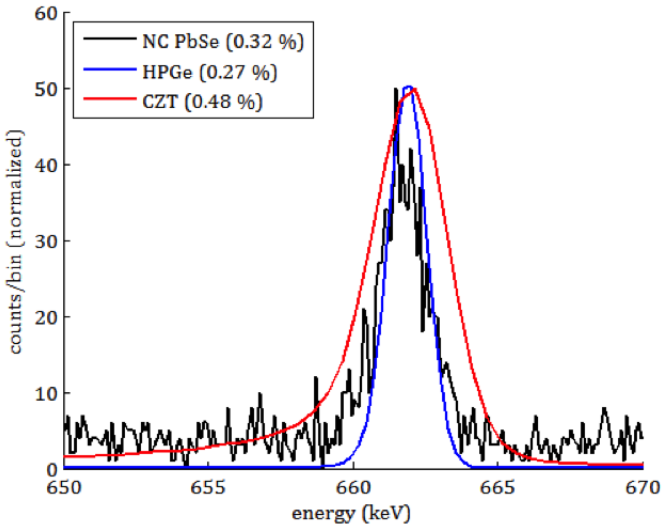

(c)

Figure 4.42: (a) Spectral comparison between high-resistivity silicon (green), CZT (red), HPGe (blue), and the PbSe nanocomposite (black), when exposed to gamma-rays emitted from Ba-133. The different measurement periods (e.g., 21.2 min. for NC PbSe, 24 hr for HPGe) account for the differences in curve smoothness, and the curves were normalized to the number of counts in the PbSe peak. Note that the HPGe and NC PbSe traces largely overlap except for the x-ray escape peak from the NC PbSe detector. (b) Close-up of the 356.02 keV peak. (c) Spectral comparison between CZT (red), HPGe (blue), and the PbSe nanocomposite (black), when impinged upon by gamma-rays emitted from Cs-137. The energy resolutions are shown in the legend. The measurement period for the NC PbSe spectrum was 46.4 min.

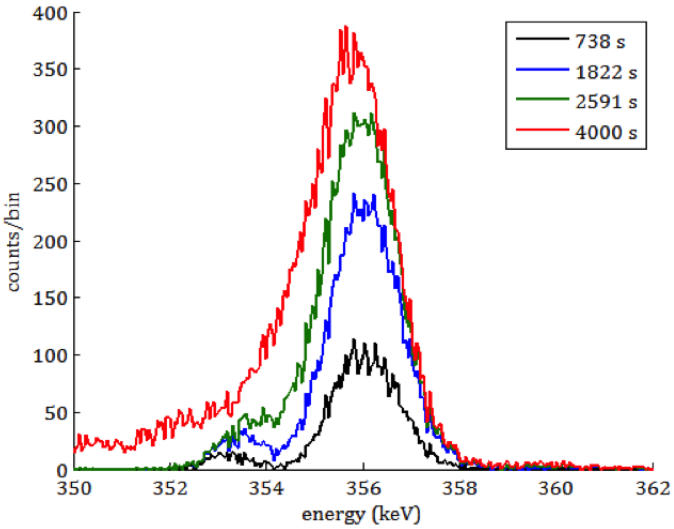

Figure 4.43: Temporal variation in the 356.02 keV peak derived from Ba-133, for the star-shaped NC PbSe detector of Fig. 3.41. The legend indicates the measurement period (live-time) for the various traces.

carriers. Although one can design the preamplifier to be insensitive to modulations in the dielectric properties of the detector medium, one would prefer a highly stable medium and the source of variation should therefore be controlled.

CHAPTER V

Conclusion

In principle, nanostructured media allow us to measure ionizing radiation with greater precision than can be achieved with single-crystal media because one has greater experimental control over the detectors governing parameters – the size and shape of the nanoparticles – than can be equivalently achieved in a nominally single-crystal media, in which defects and impurities can readily spoil the performance of the sensor. More importantly, one can yield fundamentally superior detection characteristics because one has a mechanism through which the informational processes – such as electron creation- can be controlled relative to the loss processes- such as phonon excitation. Fortuitously, this superior physics is also accompanied by a less expensive fabrication modality. Thus, nanocrystalline (NC) semiconductor materials provide an attractive material basis because they present a means of: a) decreasing the underlying material cost by utilizing a solution-based fabrication methodology, b) increasing the range of candidate materials by including the narrow-gap semiconductors, and c) increasing the exciton multiplicity upon the impingement of radiation by utilizing multi-exciton generation, qualities that can potentially be utilized to revolutionize the capabilities of radiation imaging instruments.

In this research, nanostructured cadmium and lead salts have been extensively studied as advanced media for nuclear radiation detectors. The sensitivity of their

charge-transport properties to the surface conditioning of the nanoparticles and their degradation under ambient conditions has discouraged their use in a semiconductor configuration; rather, most of the efforts geared toward nuclear radiation detection had been focused on nanostructured scintillation materials. Furthermore, the slight thicknesses that accompany the traditional spin-, dip-, and drop-casting methods have argued against their use as sensors of more highly-penetrating radiation.

However, the nanoscintillator approach has been hampered by: a) multi-exciton yield followed by non-radiative transition, b) poor light yield when mixed with a conjugating organic scintillator agent, and c) compromise in the transparency as a scintillator. We have shown that detectors with deep depletion regions can be constructed such that the deposited charge can be effectively drifted and the energy of the interacting quanta can therefore be measured. Furthermore, the accuracy of that measurement is comparable to those estimates provided by the best single-crystalline semiconducting materials, providing evidence for enhanced charge multiplication as the degree of strong confinement is increased. Nanostructured materials have therefore been projected as the next-generation material for the detection of ionizing radiation, the adoption of which depends on overcoming the difficulties associated with using a composite material comprised of innumerable interfaces at which information can be lost.

5.1 Achievements

In this research, here we have achieved:

1) The synthesis and characterization of NCs with good optical properties and narrow size distribution.

2) An examination of various solution-based NC assembly fabrication methods.

3) The successful charge transport through a NC assembly using assemblies employing ligand exchange, those deposited using the LBL method, and blended structures.

4) The attainment of distinguishable responses from radiation sources for most of the NC assembly detector samples: not only from the alpha sources, but also from low energy gamma sources in some good-quality NCs.

To summarize the deposition methods, the pros and cons for each method are:

1) Drop-casting

Pros: Deposition of large amount of material at a time and, therefore, a short processing time.

Cons: Film quality is less controllable.

2) Layer-by-layer

Pros: Controllable deposition of single layers.

Cons: Lengthy processing time and labor.

3) Ligand exchange

Pros: Decreases the inter-particle distance between NCs and makes them much more closely-packed.

Cons: Compromises the film quality due to significant contraction of the assembly when dried.

4) Blended structure with conductive polymer

Pros: The ease in achieving a macroscopic-scale assembly. Moldable and degree of chapping is reduced. Enhanced charge transport.

Cons: Introducing another medium between NCs through which charges must transport. Energetically unfavorable.

5) Vacuum filtration method

Pros: Quick and easy way to achieve a thick film of nanomaterial.

Cons: Pressure gradient uneven. Difficulties in peeling-off.

5.2 Confronting Challenges

The following are major challenges in the development of NC based nuclear radiation detectors, but these are also highly relevant to all optoelectronic devices;

1) Utilization of CM (enhancing CM efficiency)

2) Enhancing charge carrier transport

3) Refinement of the fabrication modality

4) Background noise suppression

As it has been observed from the very different scales of induced charge signals depending on detectors processed with various designs, the drift motion of charge carriers is seriously hampered by the trapping and loss of the charges within the assembly. Whereas a specific configuration of the active volume has exhibited good charge carrier transport properties which can exploit the CM property of NCs, a large portion of the NC samples still show a poor charge transport ($\sim$5 mV step pulse and $\sim$100 μs rise time of the signal), which reflects a significant loss of charges on path. Even though the charge transport properties of the NC assembly have been improved, there is still a room for further improvement.

Therefore, one needs to develop a fundamental understanding of the processes by which charge carriers interact in semiconductor materials in order to aid in the development of advanced radiation detection materials. Most importantly, one would like to achieve monodispersity of the NC size and the favorable coordination chemistry in order to realize a uniform close-packed assemblies. In addition, with the advantage of size-tunable optical properties, one may want to consider the band gap engineering of the active volume media which can favorably contribute to the charge carrier drift

motion with high mobility. The refinement of the fabrication protocols is also desired, to ensure a thick and homogeneous crack-free NC assembly deposited on the substrate. The adhesion with the metal contact, even though a minor issue, also needs to be considered to form a robust contact which can reduce the loss of charges by phonon scattering at the contact boundary.

In addition to the problems related to the quality of the sample itself, ensuring a stable testing environment must be also considered; that is, among the three factors contributing to the overall fluctuation of the system – charge carrier statistics, charge collection, and electronic noise – the former two are related to the performance of the detector, whereas the last one is related to the testing environment. Especially, in those situations in which testing a small-response is studied (e.g., distinguishing 5 mV response in the presence of 1 mV amplitude fluctuation), a slight difference in the fluctuation of the background noise can substantially jeopardize the signal-to-noise ratio of the system.

Fig. 5.1 shows a comparison of background noise fluctuations acquired in different nuclear electronics environment setups. Fig. 5.1(a) illustrates the difference in the background noise when it was measured in daytime or nighttime. As one can notice the background level is higher for the daytime measurement. Therefore most of the measurements were conducted in the nighttime. Fig. 5.1(b) shows the difference in the background noise measured using two different bias supplies at the same bias setup, one with less inherent fluctuation ($\pm$ 0.1 V) than the other ($\pm$ 0.5 V). In the measurement of the black spectrum to see the difference in the presence of background noise shown as red and blue area, the lower noise supply is obviously preferred. Instability in the preamplifier can also hamper the signal-to-noise ratio; thus, it is important to use a stable electronic setup in the measurement of sensitive devices.

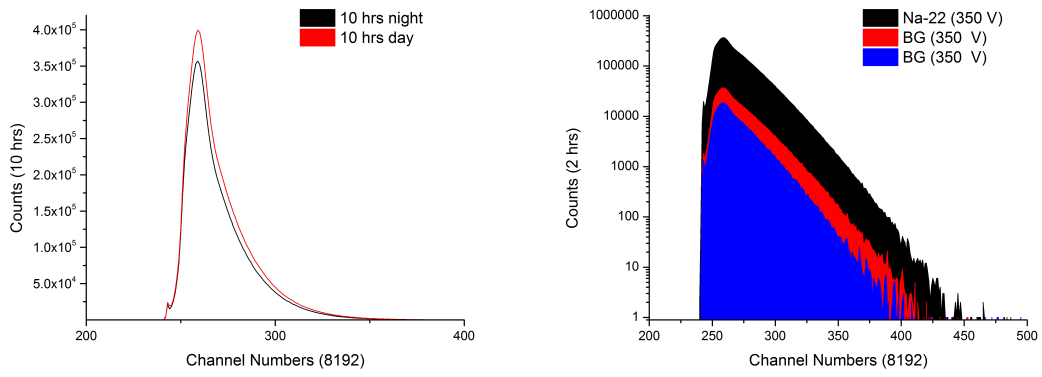

(a) (b)

Figure 5.1: Comparison of background noise fluctuation in (a) day and night measurement, and (b) using different bias supplies at the same bias setting.

5.3 Future Work

5.3.1 Material Possibilities

As has been discussed in the previous section (5.2), the future work can be focused on further enhancement of the charge carrier transport properties of the NC assembly. In addition, an effort to refine the fabrication process to provide a better quality coordination environment between the NC particles that form an assembly is needed. Furthermore, other materials with various configurations can be also investigated. The possibility is open to the various materials of different shape that are being studied in the field of NCs. In lead salts, we might prefer to use PbTe, as long as the poor stability of PbTe NCs is improved, because of the advantages in elemental composition of the material. One does not necessarily have to be limited to cadmium telluride or the lead salts. Bismuth sulfide (Bi_2S_3) nanorods are one of the good examples that satisfies our criteria [117, 118].

For instance, as the potential has been briefly discussed in this study, a possible scenario is that the enhancement in charge conductivity could be established from an enhanced number of "bridges" that connects between nanostructures efficiently.

That is, close-packing of non-spherical shaped nanostructures – tetrapod, octahedral, nanorods, nanowires – may be able to construct better transport pathways than spherical particles that transfers charge carriers. Therefore, the approach introducing exotic-shaped particles to form an assembly could be promising.

Type II core-shell particles are also promising, providing that most of the conjugate polymers are hole conducting agent. Thus, if one can efficiently separate electron from holes which can be easily extracted out of the NC particle and travel through the conductive polymer medium, one can expect better charge conductivity in the NC assembly media based on a core-shell structure blended with polymer.

5.3.2 Junction Studies

In this research, the electrical behavior was often dominated by the overall quality of the film, rather than the metal-NC contact. However, providing that one can further enhance the quality of the NC assembly, then we can study the junction properties with various metal contacts. It would be desirable to find a good ohmic and Schottky contact configuration that is not subject to the space charge limited behavior. In addition, we can also study phonon dynamics related to the metal-semiconductor junction properties via contact studies [119].

Another structure to investigate is a p-n junction structure. Even though a previous study had shown that the hydrazine treatment can help formation of n-type semiconductor assembly of PbSe NC, the exact role of hydrazine and their chemical mechanism in the formation of the NC assembly is not yet clear. Therefore, we did not seriously consider hydrazine treatment as one of the p-n junction approach; however, if it is correct that hydrazine can help to form an n-type assembly, our EDT/hydrazine treatment devices can be also considered as one of p-n junction approaches.

In addition to this, one may attempt to use well-know n-type structures to make a junction with the p-type lead salt assembly; as we want the p-type material to be

the main active media for the radiation interaction in this case, we want the n-type to be a highly-doped thin-film layer so that the depletion region can be developed in the p-type region. ZnO and TiO_2 (either in the form of nanoparticles or sol-gel film) are popularly studied materials in tandem solar cell application, and one can also try using n-type nanostructures, such as Bi_2S_3 to make a p-n junction diode [118].

5.3.3 Patterning on the Assembly

In the radiation sensing technology schemes one can try implementing single polarity sensing and/or a position sensing scheme on the NC assembly. Single polarity sensing schemes are often used to enhance the energy resolution of a radiation detector which is based on materials that have a significant difference in effective masses of electron and hole – CdTe and CZT, most particularly. Position sensing schemes are a heavily exploited method in the radiation detection and measurement field related to the homeland security and medical applications. In addition, if the electrons and holes can be tracked during their drift through the bulk of the materials, then their passage can be used as a metric to gauge the effect of various material features, such as inclusions, dislocations, and other trapping centers. For quantum-dot solids, the technology allows one to quantify the degree of charge trapping as the size, dispersion, and coordination of the matrix is varied.

If one can from a good homogeneous NC assembly, one can apply photolithography techniques to pattern the NC assembly. Then one can fabricate pixel, strip, and meandering line patterns to apply position sensing schemes for the nuclear radiation detectors. One can implement single-polarity sensing scheme by applying coplanar grid [120] or Frisch collar grid structure [121] to the assembly, which can be realized from the photolithography technique.

5.4 Final Remarks

To conclude, this research is, in short, about an effort to to overcome the homogeneity and charge conductivity challenges based on solvent processing approach using novel semiconductor material. We reported on a nanostructured material that yields an energy resolution comparable to existing single-crystal based detectors with moderate reproducibility. Even though there is a significant room for improvement in many aspects of the nanostructured material – underlining physics, synthesis and fabrication procedures, and testing and calibration schemes, the notion of a nanostructure based ionizing radiation detection approach has a high potential and it is highly promising from both scientific and engineering aspects.

APPENDICES

APPENDIX A

MCNP Simulation of Radiation Responses

A.1 Introduction

Throughout this research, PbSe NC composite assembly detectors with changing various parameters and conditions were fabricated as indicated in Fig. A.1. Compared with HPGe, the detectors responses vary because the lead-chalcogenide colloidal solid is comprised of higher atomic-number constituents, from which high-energy x-rays are emitted during the relaxation of the orbital electrons to low-lying energy states. X-ray escape peaks can therefore feature prominently in the gamma-ray spectra, particularly if the particular radiation-detector is thin relative to the mean free path of the secondary photon. In order to better understand the empirical peaks that arise from the impingement of gamma-radiation upon the PbSe NC detectors, the spectral responses of the detectors were simulated as a function of various fabrication parameters, using MCNPX-Polimi for the Monte Carlo simulations, the results from which are presented in this Appendix. The simulation results buttress the measurements which indicate that nanostructured lead-salts can yield low-cost, large area, high-performance radiation detectors.

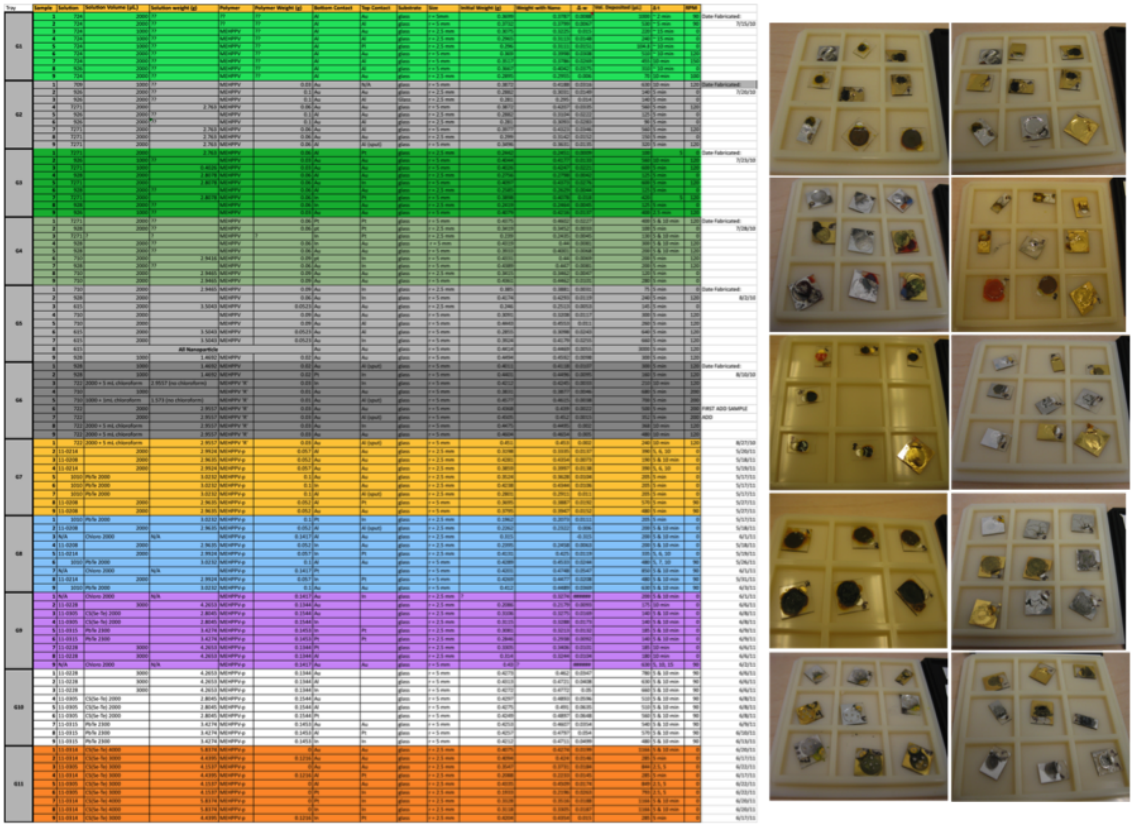

Figure A.1: (Left) Configuration table of the NC composite assemblies with various parameters in the fabrication. (Right) Fabricated NC assembly detector samples in various conditions.

A.2 Modeling of PbSe NC/MEH-PPV composite assembly detector

The self-assembling nature of the nanocrystal enables the formation of a macroscopic material for suitable for radiation detection. However, the self-assembling nature does not always exhibit a regular packing method, as it is shown in Fig. A.2. Fig. A.2(a) shows an SEM image of the surface of the NC assembly. The size of each particle was roughly 30–50 nm. However, the particles consists of smaller nanoparticles, indeed, as shown in the TEM images, Fig. A.2(b). When the smaller nanoparticles construct the bigger particles, the orientation of the lattice plane sometimes align with each other, and sometimes not. HRTEM images in Figs. A.2(c) and A.2(d) show the alignment/mis-alignment of the lattice planes between nanocrystals at their boundary region. It is expected that the orientation of the nanoparticles are more or less aligned with each other when there is an enough time allowed for the particles to assemble to the superlattice structure.

The fabrication methods used to produce a self-assembled colloidal solid, comprised of either spherical, star-shaped, or polygonal NCs have been discussed in (3.1). The degree of NC-lattice ordering is dependent upon the size and shape dispersion, with monodisperse ($< 5\%$ variation in the lateral extent of the NCs) particles resulting in close-packed, regularly-spaced solids, while dispersions with greater than $\sim$10% size-uncertainty result in random-packing.

For the physical detectors, the NC size dispersion was generally greater than 10%, but we hypothesize that those detector regions with the finest energy-resolution performance correspond to a high degree of NC ordering, because the charge mobilities are generally higher than those found in poorly order solids in which the conductive polymers retard the drift velocity. For the sake of gauging the energy-deposited by impinging radiation both superlattice structures as well as homogenized detectors

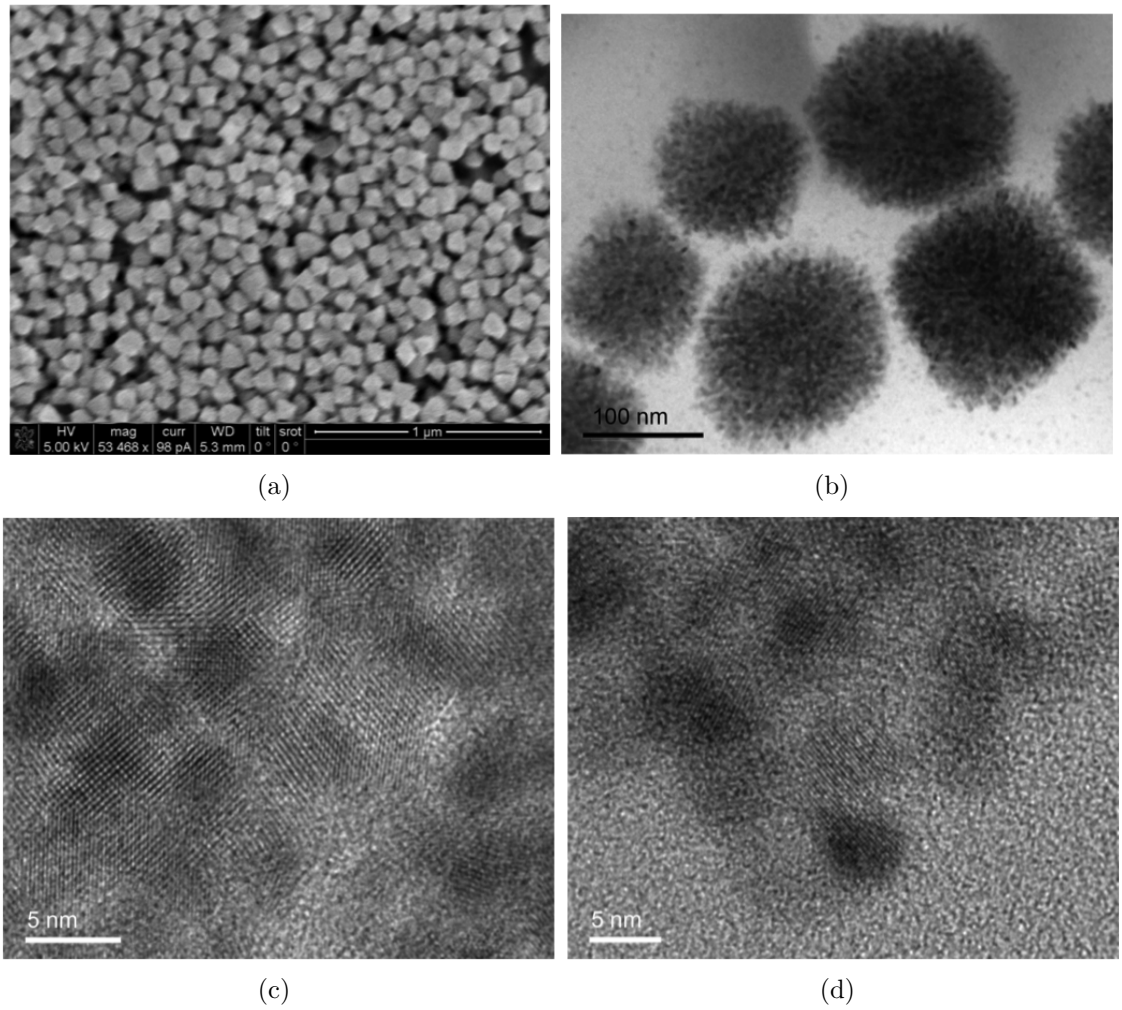

(a) (b)

(c) (d)

Figure A.2: (a) SEM image of the NC assembly surface, (b) HRTEM image of a large nanoparticle composed of smaller particles and (c,d) assembling morphology of the particles at the boundary.

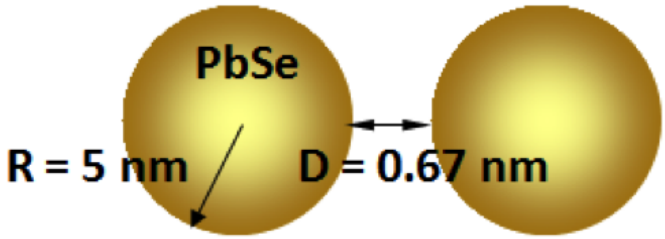

Figure A.3: Typical geometry for a PbSe quantum dot separated by a single link of the surfactant.

were simulated. As a result, both produced comparable results because the range of the secondary reactants far exceeds the size dimension of the NCs.

If one assumes a uniform size distribution of the PbSe NCs, the packing of the quantum dots in a superlattice structure governed by cubic unit cells can arrange via either simple cubic (sc), body centered cubic (bcc) or face centered cubic (fcc). The face centered cubic and hexagonal close packed structure can form the most closely packed structure. The volumetric fraction occupied by the PbSe in each scheme is: 52% (sc), 68% (bcc), or 74% (fcc and hcp) respectively, in the case of the closest packing.

In the physical detectors, the NCs are separated by the capping ligands, which impose a finite separation between particles, as illustrated in Fig. A.3, in which a polymer order of 1 is assumed for the organic surfactant of a short chain such as butylamine (BA). In reality, we have experimentally sampled the parameter space in which the relative volumetric blend between the NC volume and the polymer volume can vary; however, the best detectors generally have a high concentration of NCs, and we will therefore simulate a typical separation. For example, making a simple assumption of 1 nm (20% of the size of the particle) interparticle distance between the 5 nm PbSe NCs shown in Fig. A.3, the packing fractions reduce to: 39% (sc), 51% (bcc), and 56% (fcc and hcp), respectively. If the size of each particle is not uniform, even higher packing ratios than 74% in volume are possible, because interstitials of smaller NCs can be packed between bigger NCs.

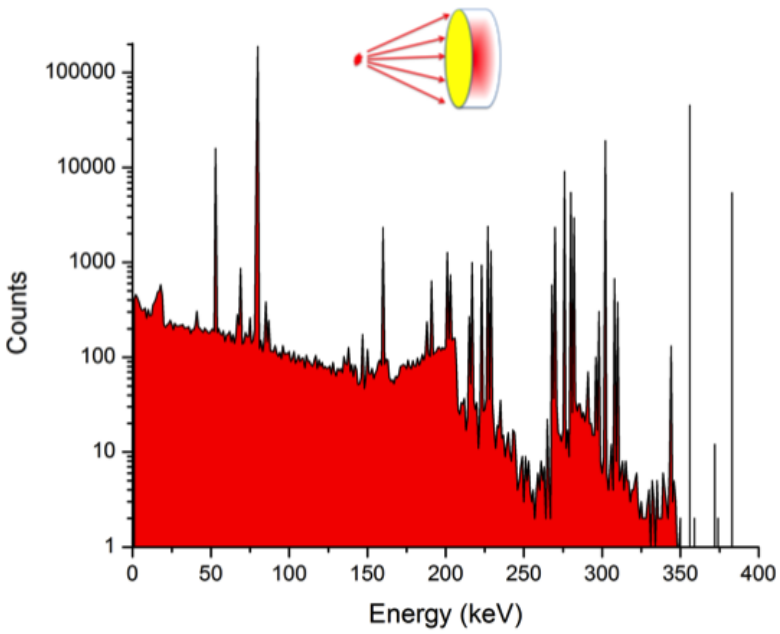

(a)

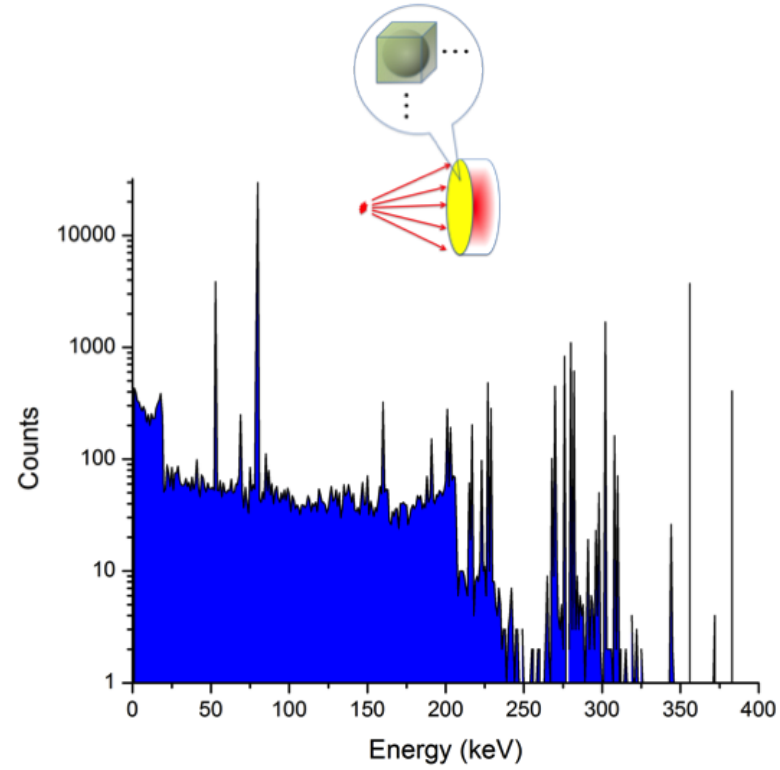

(b)

Figure A.4: Schematic of the simulation geometry and the simulated spectra of Ba-133 from (a) bulk PbSe medium and (b) PbSe NC/p-MEH-PPV composite assembly of 1 mm thickness.

The motivation for utilizing lead chalcogenide NC material for the sensing of ionizing radiation detection was already discussed in (2.2). In comparison with competing detection media, lead chalcogenide materials can exhibit orders of magnitude higher stopping power, especially for high-energy gamma rays with energies exceeding 1 MeV. The Monte Carlo simulation was performed for a PbSe NC/p-MEH-PPV composite assembly, in which a conservative assumption on the particle packing in the assembly is assumed. As shown in the schematic of Fig. A.4(b), a single PbSe nanoparticle contained in a simple cubic unit cell (sc) with the distance between the nanoparticles of 20% of the PbSe NC particle size were assumed and the rest of the cell volume was filled with para-MEH-PPV. Therefore the volumetric fraction of the PbSe NC in the NC/polymer composite cell was only 39%. Amongst various types of MEH-PPVs, p-MEH-PPV ($(C_25H_32O_2)_n$, $\lambda_{ex} = 451$ nm, $\lambda_{em} = 517$ nm in chloroform) was used in the fabrication of the PbSe NC composite assembly samples, because: 1) it was characterized in chloroform, which is the solvent in which the PbSe NCs are dispersed, and 2) it has the longest excitation/emission wavelength so that it could be comparable in bandgap to the NCs.

Energy (keV)	Intensity (%)
53.161	2.199
79.6139	2.62
80.9971	34.06
160.613	0.645
223.234	0.45
276.398	7.164
302.853	18.33
356.017	62.05
383.851	8.94

Table A.1: Gammas emitted from Ba-133 (half life – 10.51 y)

The simulation was performed for a Ba-133 source for which the branching ratio is illustrated in Table A.1, to compare the expected spectral response of the PbSe bulk material with PbSe NC/conductive polymer composite assembly. The detector

was cylindrical, with a 1 cm diameter and 1 mm thickness, and the detector was assumed to have a 300 nm gold contact on the front side, as shown in Fig. A.4. Due to the complicated lattice structure geometry that is repeated hundreds of thousand times in a 1 mm thickness media, the computation time of the Monte Carlo simulation was substantial; therefore, 10^6 particles were simulated for both the composite assembly and the single-crystalline equivalent, and peak broadening due the detector and electronics was not taken into the consideration for the following simulations.

The simulated spectra are illustrated in Fig. A.4. The total intrinsic efficiency for 1 mm thick PbSe bulk crystal was calculated to be 35.5% and the total intrinsic efficiency for the 1 mm thick PbSe NC/p-MEH-PPV assembly was 6.28%; however, the packing fraction can be substantially improved by using shorter chain ligands, or by employing non-spherical particles. Qualitatively, the single-crystalline spectrum has a substantially higher Compton continuum as well as a greater density of x-ray escape peaks; however, the general peak structure is comparable. The extra organic materials used in the colloidal assembly do not muddy the peak structure at the energies of interest.

A.3 Contributions of various event types to the spectra

The simulated spectrum shown in Fig. A.4 exhibits many features, including x-ray escape peaks as well as the full energy absorption peak, and Compton continua from the scattering event either in PbSe NC or in p-MEH-PPV. Therefore, in order to correctly identify each specific feature in the spectra, every interaction that deposits energy in the assembly can be categorized by event type as well as the element with which the interaction occurred. The parsed spectra by event type and interacting element are shown in Fig. A.5.

Fig. 1.5(a) shows the contributions from each event type (photoelectric absorption, Compton scattering, single x-ray escape, and double x-ray escape). If the size of the

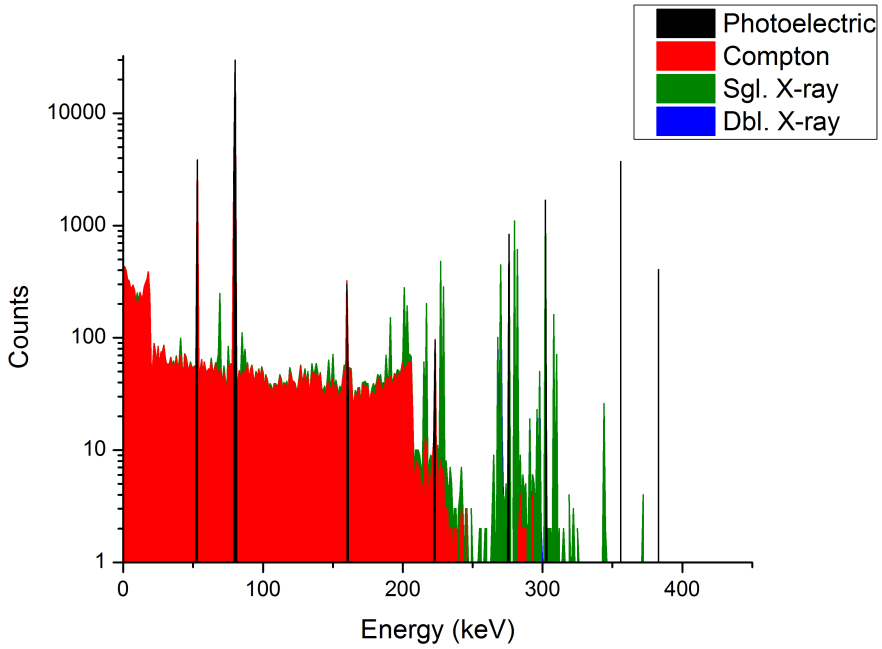

(a)

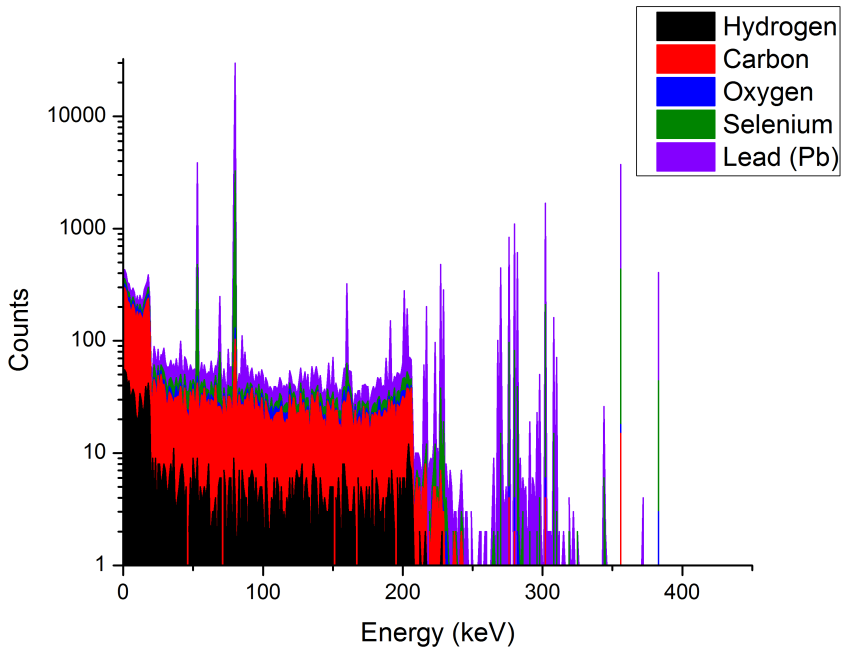

(b)

Figure A.5: Simulated spectra of Ba-133 from the PbSe NC/p-MEH-PPV assembly showing contributions from (a) each event type and (b) interactions with each element.

detector geometry is comparable to or large enough to cover the mean free path of the characteristic x-rays, most of the fluorescence x-rays are expected to go through another interaction in the medium and are likely to be absorbed in the detector. Thus, even though there is always x-ray fluorescence accompanying a photoelectric event, one may see full energy absorption peaks instead of x-ray escape peaks from a detector of large enough volume. Even for the thin detector, the full-energy peaks from gamma ray emissions shown in Table A.1 stand out substantially compared to the Compton continuum, and the shape is dominated by photoelectric absorption, Compton scattering, and single x-ray escape peaks. In the physical spectra, peaks that are consistent with double x-ray escape are also observed, which indicates that the size is smaller than that simulated.

The x-ray escape peaks and the interaction with each element to the overall spectrum of Ba-133 in the PbSe NC/p-MEH-PPV assembly is displayed in Fig. A.5(b). The deposition of energy on selenium and lead is due to the interactions with PbSe nanoparticles, and the interactions with H, C, or O result in energy depositions due to the presence of p-MEH-PPV. Notably, most of the full energy absorption peak events are contributed by the PbSe NCs, whereas the Compton continuum, derived primarily from 356 keV and 384 keV gamma rays, is due to the carbon that accompanies the p-MEH-PPV. This is consistent with the experimental results, in which fully p-MEH-PPV sensors do not possess the full-energy peaks.

Since the photoelectric effect is an interaction of a photon with a bound electron, which is expelled from is orbit, x-ray fluorescence accompanies the interaction. If the detection medium is small enough, then those characteristic x-rays can escape from the active volume, resulting in an energy deposition reduced by the x-ray energy. One can identify from which element a specific x-ray escape peak is originated, an analysis which indicated that most of x-ray escape peaks are derived from Pb and Se atoms. Furthermore, Pb dominates the photoelectric events because the probability

of photoelectric absorption scales with the 4–5th power of atomic number. Moreover, the energies of the characteristic x-rays from Pb are much higher and thus much more likely to escape from the NC assembly. Sometimes, two x-ray fluorescence events can occur in the interaction with Pb atom, and both x-rays can escape the medium. Single fluorescence events and double fluorescence events from the full energy deposition are shown in Fig. A.5(a) with green and blue bars respectively. The energy of the major peaks due to x-ray escape events are as follows: 1) single escape peaks at: 69 keV, 85 keV, 201–203 keV, 215-217 keV, 227–229 keV, 268–271 keV, 280–282 keV, 308–310 keV, and 2) double escape peaks at 216 keV, 269 keV, 271 keV.

One can also identify gamma rays of which energy is contributing to the specific x-ray escape peak, by tracking of each individual event in the assembly. Fig. A.6 shows a few examples of spectral contribution of events originated from gamma ray photons of a certain energy (81 keV, 276.4 keV, 303 keV, 356 keV, and 384 keV). The left column shows overall spectral contribution of gamma ray photons of a certain energy, and right column shows spectral contribution of x-ray escape event from the gamma ray photons of that energy. Therefore, the spectra on the right column are showing only the x-ray escape event selected out from the spectra on the left column. From the plots parsing all the event types, incident energies, and all the elements, one can identify from which element and incident energy a certain escape peak is contributed. These escape peaks and full energy peaks are mostly contributed by PbSe NCs as one can tell from the elemental contribution in the Fig. A.5(b).

A.4 Gaussian Boradening of the spectrum

The simulated spectra shown above did not include any broadening effects of the peak caused by the inherent statistical spread in number of charge carriers, variations in charge collection efficiency, and contributions of electronic noise, for example. The

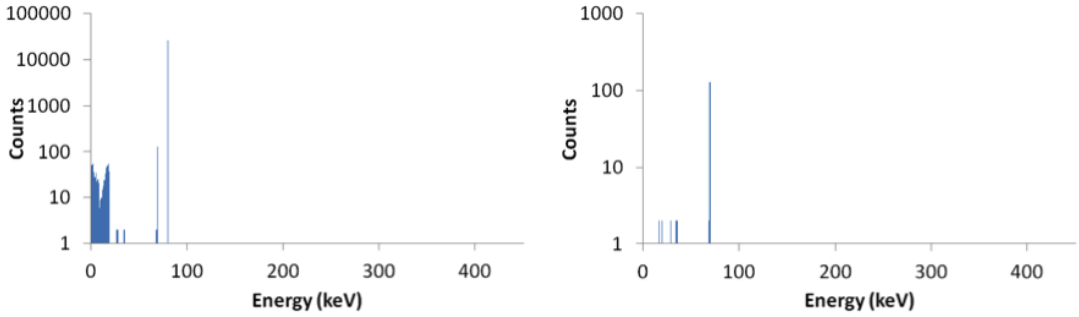

(a) X-ray escape peak from 81 keV gamma existing at 71 keV

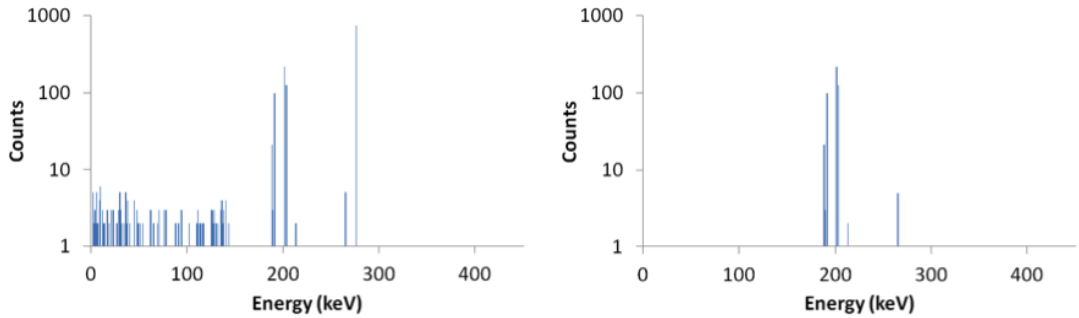

(b) X-ray escape peaks from 276.4 keV gamma existing at 190, 193, 203, 206, 267 keV

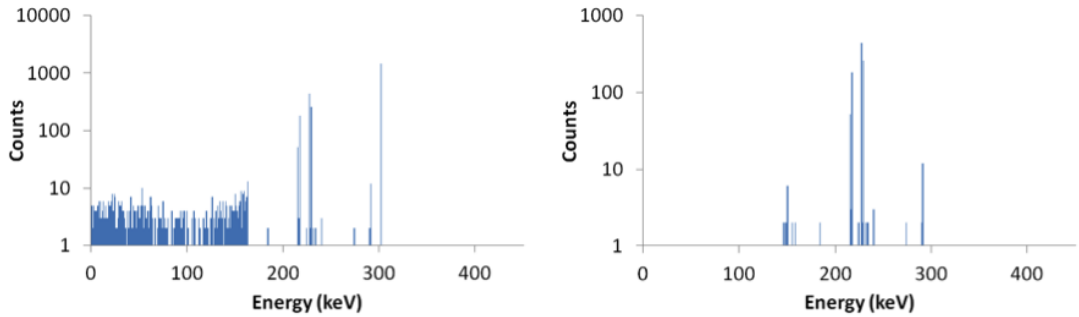

(c) X-ray escape peak from 303 keV gamma existing at 152, 217–219, 229–231, 293 keV

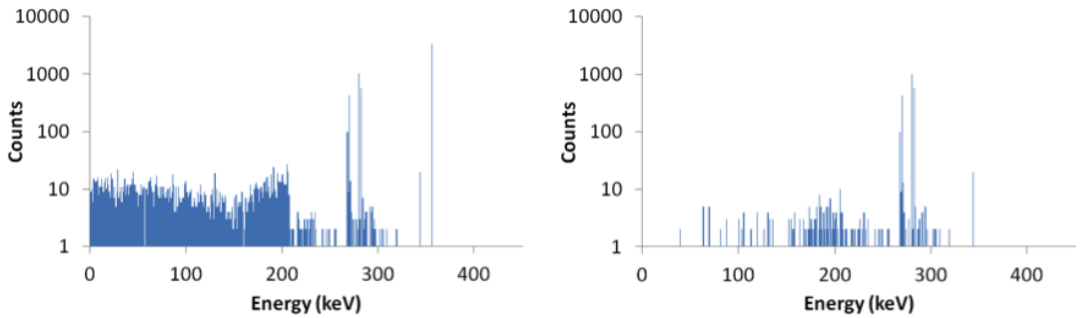

(d) X-ray escape peak from 356 keV gamma existing at 270–273, 282–284, 346 keV

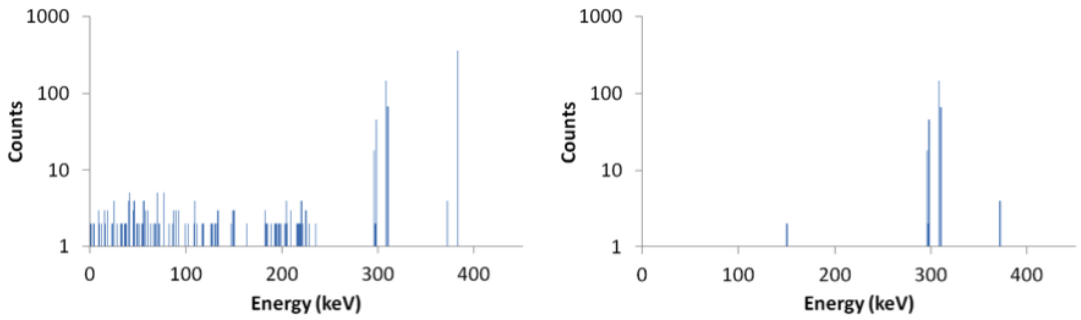

(e) X-ray escape peak from 384 keV gamma existing at 298–300, 310–312, 374 keV

Figure A.6: Simulated spectra from gamma ray photons of a certain energy emitted from Ba-133 having interactions in the 1 mm thick PbSe NC/p-MEH-PPV composite assembly. Left column shows spectral contribution of overall events from the energy, and spectra on the right column show X-ray fluorescence escape events, selected out from the spectra on the left column.

overall energy resolution of the radiation detector can be represented as follows:

$$W_T^2 (= (\text{FWHM})^2) = W_D^2 + W_X^2 + W_E^2 \tag{A.1}$$

where W_D^2 represents the stochastic fluctuations in the number of charge carriers created, W_X^2 is due to incomplete charge collection, and W_E^2 accounts for the electronic noise. Considering the mechanism each component contributes to the energy uncertainty broadening, we can regard the first term as scaling with $\sqrt{E}$, the second term scaling linearly with the energy, and the last term a constant contribution to the energy broadening. Therefore, one can represent the empirical equation as follows:

$$\text{FWHM} = a + b\sqrt{E + cE^2} \tag{A.2}$$

The three parameters can be determined empirically, by fitting the measured resolution in terms of the energy of the peak. If we assume a Gaussian broadening of the peak we can determine the relative contributions about a certain energy peak in

count rate using the probability distribution function represented as follows,

$$f(E) = C\ e^{-\left(\frac{E-E_0}{A}\right)^2} \tag{A.3}$$

where, E_0 = the unbroadened energy deposited in the detector,

E = the broadened energy,

C = a normalization constant. The Gaussian width A can be determined from FWHM:

$$A = \frac{\text{FWHM}}{2\sqrt{ln\ 2}} \approx 0.6 \times \text{FWHM} \tag{A.4}$$

Using experimental data for the peak energy resolution of 356 keV (0.42%) and 662 keV (0.32%) gamma rays from the result, the FWHM curve was fitted.

A.5 Variations in the Spectral Response with Thickness

Fig. A.7 shows the Gaussian broadened energy spectrum simulated for the PbSe NC/p-MEH-PPV assembly of various thicknesses. And Fig. A.8 shows the simulated spectrum for the case of the 20 μm-thick assembly presented in log scale. The overall feature does not look remarkably different from the previous simulation results. Simulations performed for equivalent characteristic NC composite assemblies but with smaller thicknesses, exhibit a higher contribution from the x-ray escape peaks, as expected.

As the detector thickness increases, the probability of capturing the secondary x-rays increases, as reflected quantitatively in Fig. A.9. Note that, in the Fig. A.9 and A.10 results, the nanostructure of the detector was homogenized, because MCNPX cannot model geometries smaller than 50 nm, which prevents the precise modeling of the array comprised of 4–7 nm particles. The physical detector was approximated by

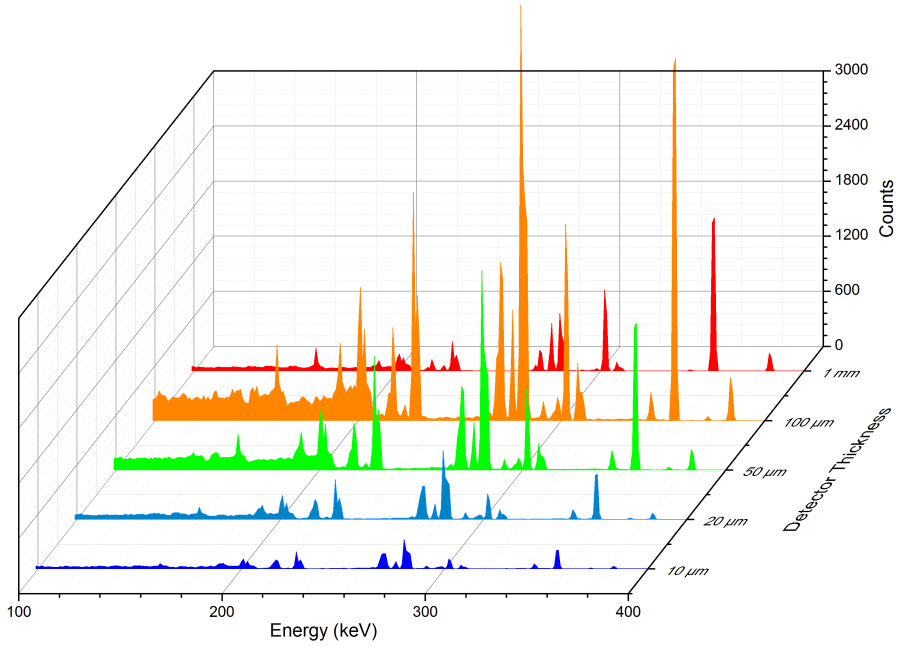

Figure A.7: Gaussian broadened energy spectra of Ba-133 simulated for PbSe NC/p-MEH-PPV assembly of various thicknesses. 1 mm thick assembly was simulated for 10^6 particles, whereas others were simulated for 5×10^7 particles, to qualitatively compare the relative peak area and x-ray escape peaks.

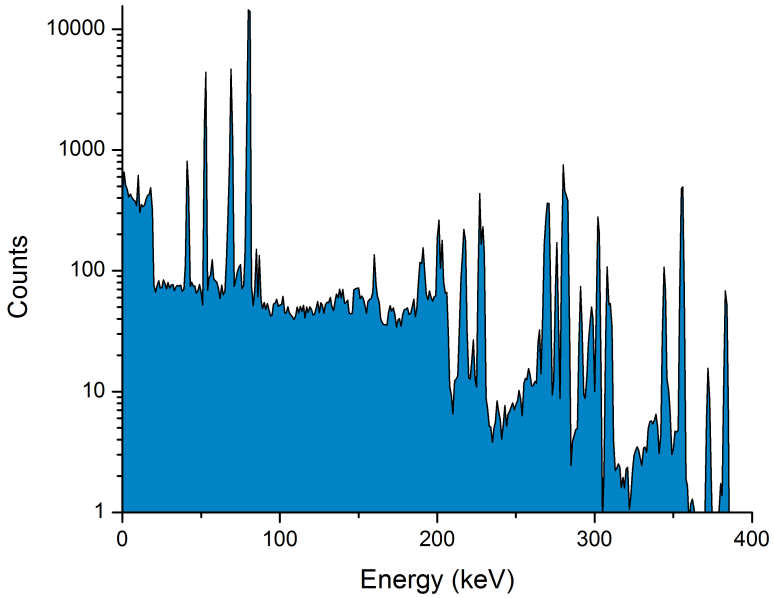

Figure A.8: Gaussian broadened energy spectra of Ba-133 simulated for PbSe NC/p-MEH-PPV assembly of 20 μm thicknesses. One can see relatively higher ratio of x-ray escape peaks compared with simulated spectra from 1 mm or 100 μm thickness assemblies in Fig. A.7.

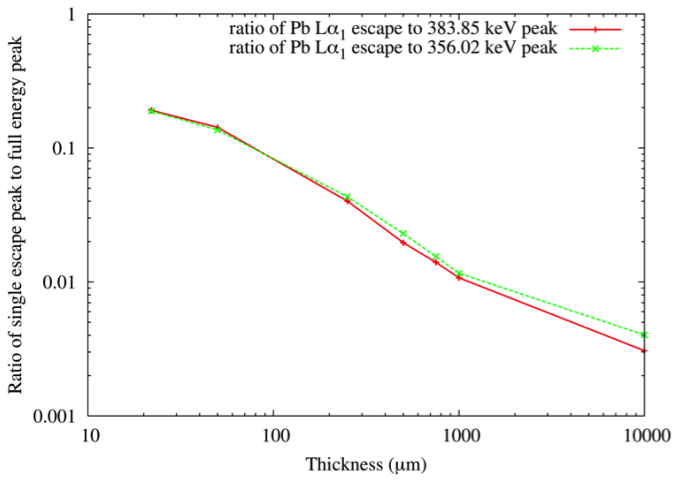

Figure A.9: A plot showing the ratio of the Pb $L_{\alpha 1}$ single escape peak to its full energy peak for increasing thicknesses of the active region.

homogenizing the PbSe nanoparticles and polymer, conserving mass. Nevertheless, the method is valid given that the structure of the PbSe varies throughout the volume of the detector, and that the size of the PbSe nanoparticles is not substantially larger than the size of a PbSe molecule (∼0.1 nm). The PoliMi code was used to select only those events that deposit energy in Pb or Se, as this functionality is not available in the standard version of MCNPX when using a single homogenized material. It was also assumed that the entire NC region was active (i.e., there is no dead layer).

A two-dimensional diagram of the geometry used is shown in Fig. A.11, and was designed to match the experimental setup as closely as possible. The geometry shown in Fig. A.11 was used in conjunction with a Ba-133 point source placed 5 cm above the detector region. The energy spectrum was tallied using 800 energy bins, each with a width of 0.25 keV. As shown in Fig. A.9, the thickness of the detector increases the counts in the full energy peak relative to the x-ray escape peaks, where the ratio of the single x-ray escape peak from Pb $L_{\alpha 1}$ to the full energy peak is plotted against thickness for the 383.85 keV peak and the 356.02 keV peak from Ba-133. As expected, the efficiency of the detector at counting the full energy peaks increases with thickness. More importantly, the complications associated with extracting full-

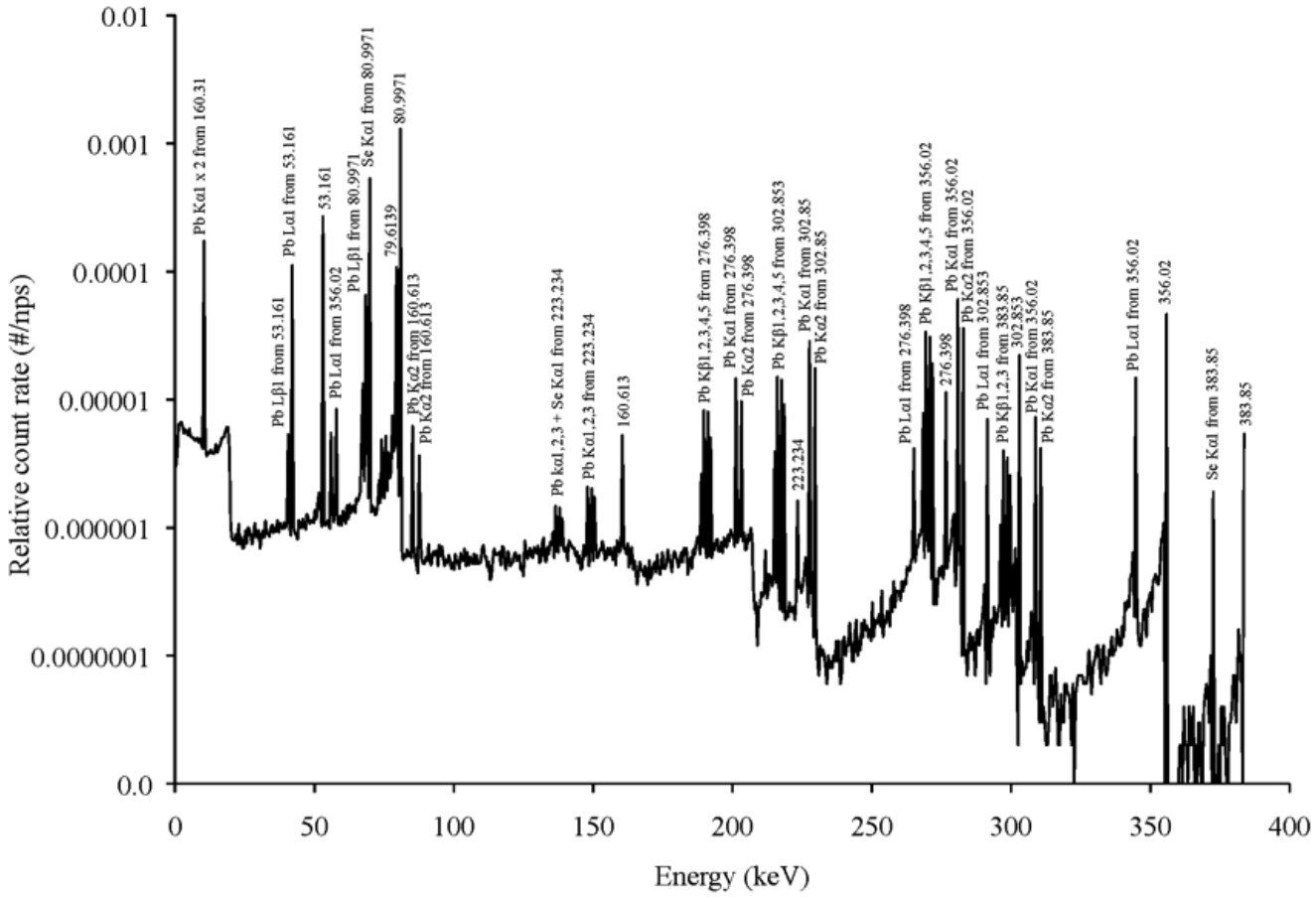

Figure A.10: The energy spectra of Ba-133 from simulation with the main peaks identified. The energy spectra of Ba-133 from simulation with the main peaks identified, using 22 μm thick detector

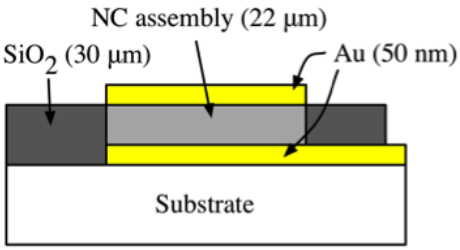

Figure A.11: Diagram of the detector geometry modeled. A 1×1 cm^2 of varying thicknesses (here shown as 22 μm thick) is sandwiched between two Au contacts.

energy peaks from a distribution adulterated by escape features can be avoided for detector with thicknesses greater than roughly 1 mm. The energy spectrum for Ba-133 using a thickness of 22 μm is shown in Fig. A.10 with the main peaks identified. Note that the peaks tail toward lower energies due to secondary electron escape as well as x-ray escape.

A.6 Conclusions

Nanostructured radiation sensors comprised of blended arrays of lead-chalcogenide nanoparticles provide exceptional energy resolution performance. However, if the detector is thinner than ∼100 μm, then the high probability of photoelectric absorption, combined with the high energy of the x-rays emitted from lead, results in a spectrum within which single and double x-ray escape peaks proliferate. Using MCNPX-Polimi, we simulated the performance of the detectors as the thickness was varied and found that if the detector thickness exceeds 1 mm, then the full-energy peaks dominate the response. Furthermore, an event-by-event accounting of the interactions shows that the photopeaks are dominated by the PbSe NCs, but the Compton continuum intensity is governed by the amount of organic polymer used to coordinate the assembly. The simulated results support the experimental spectra, in which the photopeaks are accompanies by a distribution of single and double x-ray escape peaks.

APPENDIX B

Fabrication of Nanocrystal Assembly Substrate

In the fabrication of the NC assembly detector, one of the essential issues was to develop a reliable substrate for the assembly, which can act as a basin to hold the NC solution and let it dry without any leakage. In addition, both the top and bottom metal contacts must be accessible to connect each side of the electrode to the detector electronics module. In addition, the wall of the basin has to be insulating, and it must entirely separate the top and bottom metal contacts. We developed three approaches that allow us to make robust substrates for NC assembly deposition: a) printed circuit board (PCB)-based, b) Si wafer-based, and c) glass wafer-based substrates. Fig. B.1 illustrates schematics and pictures of the 3 different approaches for the NC assembly substrate.

The Printed Circuit Board-based substrate was made by melting soldering lead in the via-hole of the PCB. The circular bottom-contacts can be formed which facilitates the deposition of the NC solution. The thickness can be roughly controlled by the amount of soldering lead deposited on the hole, which is 1 or 2 mm deep; thus, the support structure allows one to grow relatively thick layers of the NC assembly compared with methods which utilize thinner substrates. Furthermore, the PCB provides a natural insulating structure in order to isolate the detectors electrically.

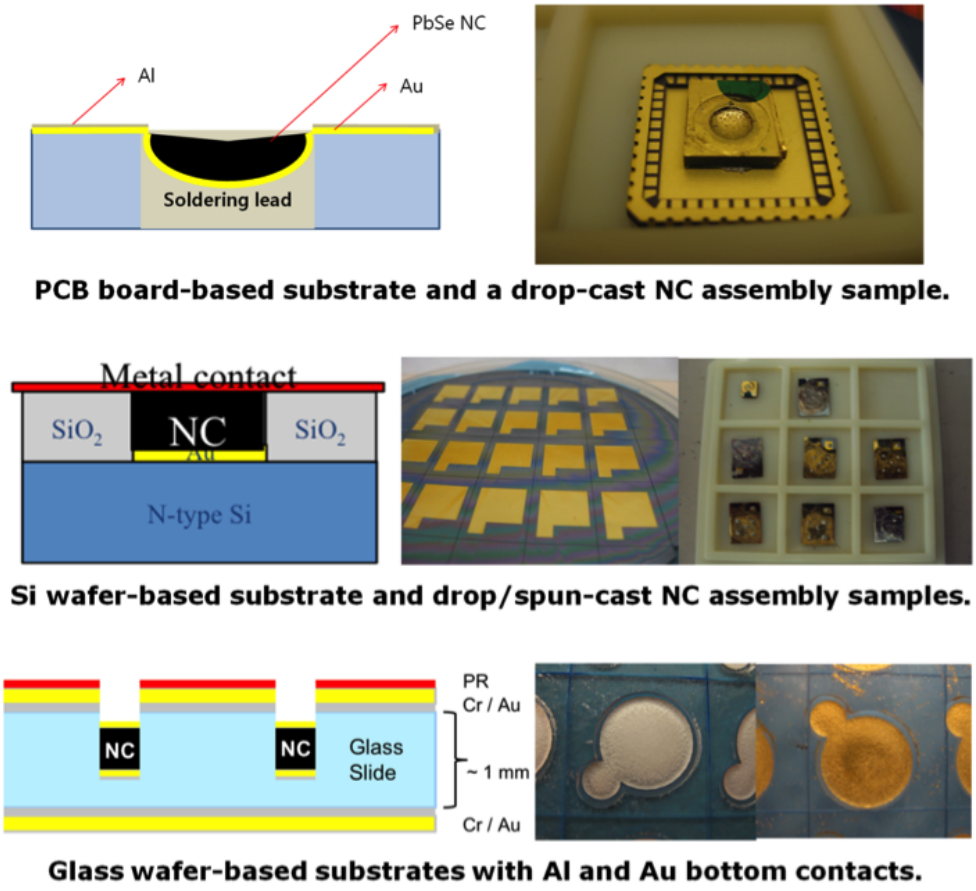

Figure B.1: Illustration of 3 different types of substrates for the NC assembly deposition.

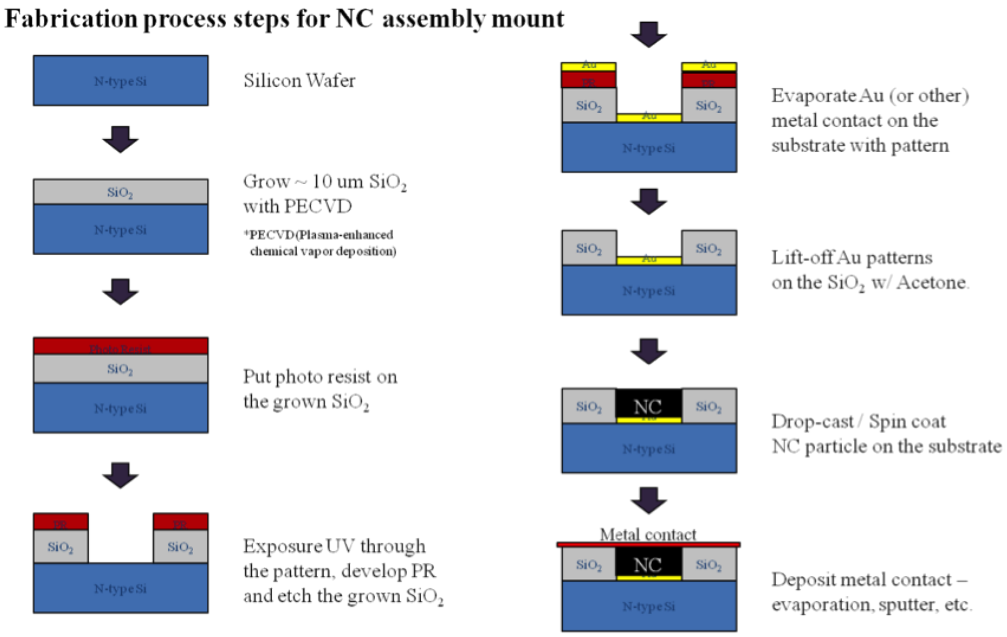

Figure B.2: Schematic of Si wafer-based NC assembly substrate fabrication procedure.

For the PCB-based detector, physical access to both top and bottom electrodes is relatively easy, because the bottom contact is connected all the way through the bottom with soldering lead. However, the round bottom contact does not, in general, deliver a uniform electric field within the NC assembly and the geometry of the NC assembly is somewhat irregular, which complicates modeling of the detector response. Nevertheless, we use the PCB-based detectors mainly as validation tools, comparing their response with the silicon-based detectors, in order to ensure that the detector-response is due to the colloidal solid rather than the substrate or associated oxide layers.

Most of the detectors fabricated were assembled on the silicon substrate using photolithographic methods. The silicon-wafer-based NC assembly substrate fabrication procedure is illustrated in Fig. B.2. After removing debris and organic contaminants on the silicon substrate with a PIRANHA solution (1:1 mixture of hydrogen peroxide (H_2O_2) and sulfuric acid (H_2SO_4)), several micrometers of thermal oxide are grown via plasma enhanced chemical vapor deposition (PECVD). Photo-resist (PR) 1813 is

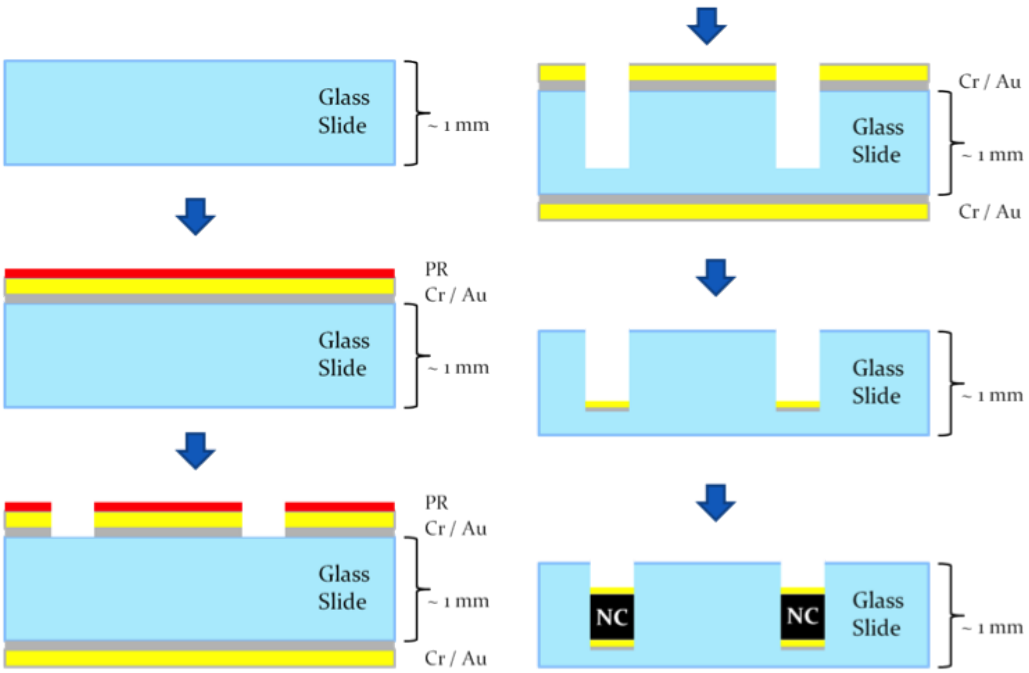

Figure B.3: Schematic of glass wafer-based NC assembly substrate fabrication procedure.

then spun at 4 krpm for 30 sec, resulting in a thickness of 1.5 μm. The PR-coated wafer is then exposed to UV light through the pattern-designed mask with the MA-6 aligner for 6 sec. The PR is then developed with MF319 developer for 1 minute and the patterned silicon dioxide is etched in buffered HF for 20–30 minutes. Electrode metals are then deposited with an Enerjet evaporator, and lifted-off with with 1112A for 1 day. The NC assembly is then grown on the fabricated substrate and a second metal electrode is evaporated on the top of the assembly in order to complete the device.

One of the drawbacks of the Si wafer based substrate lies on the equipment-based limitation of the silicon dioxide (SiO_2) thickness, which is grown to up to tens of micrometers with PECVD, a thickness which limits the volume of the NC assembly, for even if we develop a NC assembly over large areas, one still prefers sufficient thickness to yield a high intrinsic detector efficiency. Moreover, the silicon wafer does not play any role in the NC assembly detector other than to physically support the

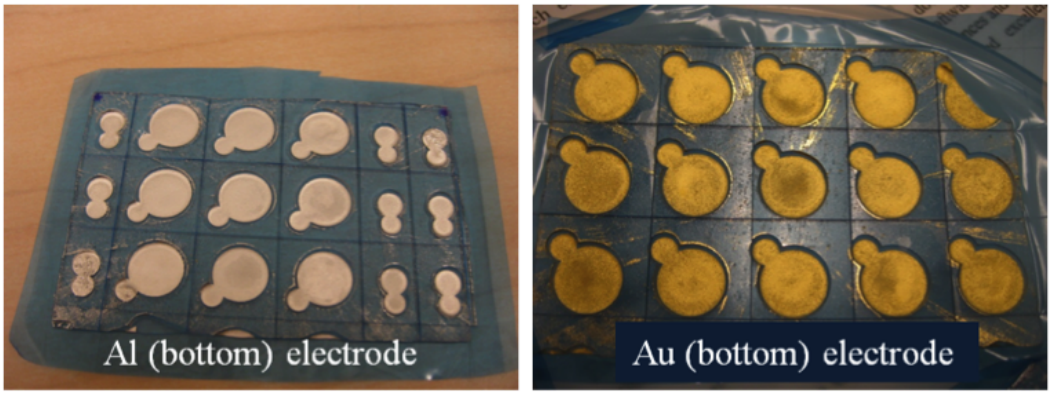

Figure B.4: Glass wafer-based NC assembly substrate with Al and Au bottom contacts.

substrate. In order to enable thicker detectors with an insulating support structure, we have developed the substrate using glass wafers (and glass slide). Instead of growing insulating SiO_2 on the top of silicon wafer, this method makes use of the existing silicon dioxide body to hold and insulate the NC assembly, the detector pit made via HF etching of the substrate. Therefore, one can readily achieve detector wells that are several hundred micrometers to several millimeters thick.

Fig. B.3 shows the fabrication procedure of the glass wafer-based NC assembly substrate, which also makes use of standard photolithography processes. After cleaning the glass wafer with PIRANHA etching, in order to remove debris and other organic contaminants on the surface, a Cr/Au layer of 100 nm/500 nm is evaporated on one side in order to form the bottom contact. Either 1813 or 1827 photo-resist (PR) is spun and hard-baked. After exposing UV light through the designed pattern, the PR is developed to expose the Cr/Au layer along the pattern. We then plunge the wafer into Au and Cr etchant accordingly, which exposes the surface of the glass wafer through the pattern. After evaporating another Cr/Au layer on the back-side in to prevent it from being etched, the wafer is dipped into 1:1 HF solution, for 1.5 to 2 hours, in order to etch the glass wafer along the exposed area, 1.5 to 2 hours is required to develop a pit that is several 100 micrometers thick. The existing Cr/Au layer is then entirely removed and photolithography is used to deposit the metal con-

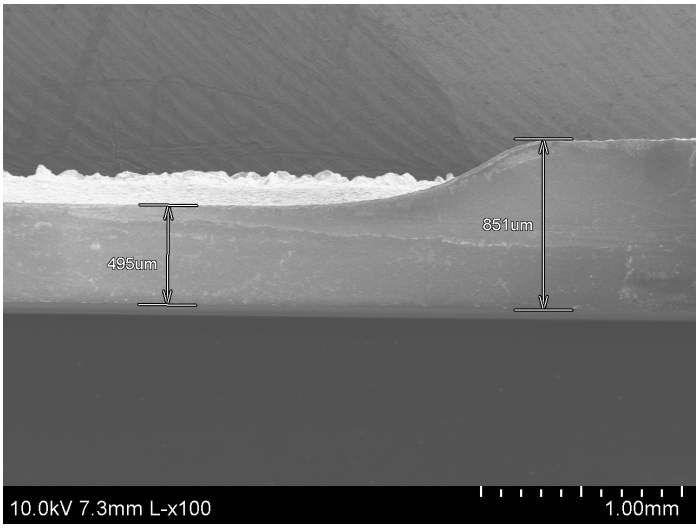

Figure B.5: Cross-sectional view of the glass-based substrate.

tacts on the bottom of the wells (note that the second photolithography process using PR is omitted in Fig. B.3).

Several fabricated substrates are shown in the Fig. B.4. The lines stretching horizontally and vertically are due to the dicing of the substrate. Blue colored tape is attached to the backside, before the substrate is diced. The glass wafer-based substrates were designed in a circular shape to make the spin-casting procedure more efficient. Fig. B.5 shows the cross-sectional view of the glass-based substrate taken with SEM. This image especially shows the well of $\sim$400 μm etched into the glass wafer. Due to the uneven etching rate of HF solution depending on the region, the depth of the glass-based substrate varied from ca. 300 μm to ca. 700 μm, which still can be characterized with micrometer before the NC assembly deposition. Now, in the way as explained in Chap. 3, the NC assembly can be grown on the fabricated substrate and a second metal electrode is evaporated on the top of the assembly in order to complete the device.

BIBLIOGRAPHY

BIBLIOGRAPHY

[1] M. Hammig, "Nanoscale methods to enhance the detection of ionizing radiation," *Current Topics in Ionizing Radiation Research*, 2012.

[2] N. J. Withers, B. A. Akins, A. C. Rivera, J. B. Plumley, G. A. Smolyakov, and M. Osiński, "Lead-iodide-based nanoscintillators for detection of ionizing radiation," *Proc. SPIE 7304, Chemical, Biological, Radiological, Nuclear, and Explosives (CBRNE) Sensing X*, p. 73041N, May 12 2009.

[3] S. Stange, *Nanocomposite Scintillators For Neutron Capture Measurements*. PhD thesis, University of Michigan, 2011.

[4] L. G. Jacobsohn, K. B. Sprinkle, S. A. Roberts, C. J. Kucera, T. L. James, E. G. Yukihara, T. A. DeVol, and J. Ballato, "Fluoride nanoscintillators," *Journal of Nanomaterials*, vol. 2011, pp. 42:1–42:6, Jan. 2011.

[5] N. Klassen, V. Kedrov, V. Kurlov, Y. Ossipyan, S. Shmurak, I. Shmyt'ko, G. Strukova, N. Kobelev, E. Kudrenko, O. Krivko, A. Kiselev, A. Bazhenov, and T. Fursova, "Advantages and problems of nanocrystalline scintillators," *Nuclear Science, IEEE Transactions on*, vol. 55, pp. 1536–1541, Jun. 2008.

[6] L. A. Padilha, W. K. Bae, and J. M. Pietryga, "Probing the gamma-scintillation process in semiconductor nanomaterials using ultrafast transient cathodoluminescence." Unpublished results.

[7] G. Kim, J. Huang, and M. Hammig, "An investigation of nanocrystalline semiconductor assemblies as a material basis for ionizing-radiation detectors," *Nuclear Science, IEEE Transactions on*, vol. 56, pp. 841–848, Jun. 2009.

[8] G. Kim and M. Hammig, "Development of lead chalcogenide nanocrystalline (NC) semiconductor ionizing radiation detectors," in *Nuclear Science Symposium Conference Record (NSS/MIC), 2009 IEEE*, pp. 1317–1320, Nov. 2009.

[9] V. I. Klimov, "Detailed-balance power conversion limits of nanocrystal-quantum-dot solar cells in the presence of carrier multiplication," *Applied Physics Letters*, vol. 89, no. 12, p. 123118, 2006.

[10] R. J. Ellingson, M. C. Beard, J. C. Johnson, P. Yu, O. I. Micic, A. J. Nozik, A. Shabaev, and A. L. Efros, "Highly efficient multiple exciton generation in colloidal PbSe and PbS quantum dots," *Nano Letters*, vol. 5, pp. 865–871, 2012/10/22 2005.

[11] J. B. Sambur, T. Novet, and B. A. Parkinson, "Multiple exciton collection in a sensitized photovoltaic system," *Science*, vol. 330, no. 6000, pp. 63–66, 2010.

[12] M. Beard and R. Ellingson, "Multiple exciton generation in semiconductor nanocrystals: Toward efficient solar energy conversion," *Laser & Photonics Reviews*, vol. 2, no. 5, pp. 377–399, 2008.

[13] O. E. Semonin, J. M. Luther, S. Choi, H.-Y. Chen, J. Gao, A. J. Nozik, and M. C. Beard, "Peak external photocurrent quantum efficiency exceeding 100 % via MEG in a quantum dot solar cell," *Science*, vol. 334, no. 6062, pp. 1530–1533, 2011.

[14] A. Nozik, "Quantum dot solar cells," *Physica E: Low-dimensional Systems and Nanostructures*, vol. 14, no. 1, pp. 115–120, 2002.

[15] M. C. Hanna and A. J. Nozik, "Solar conversion efficiency of photovoltaic and photoelectrolysis cells with carrier multiplication absorbers," *Journal of Applied Physics*, vol. 100, no. 7, p. 074510, 2006.

[16] E. Sargent, "Infrared photovoltaics made by solution processing," *Nature photonics*, vol. 3, no. 6, pp. 325–331, 2009.

[17] S. Mcdonald, G. Konstantatos, S. Zhang, P. Cyr, E. Klem, L. Levina, and E. Sargent, "Solution-processed PbS quantum dot infrared photodetectors and photovoltaics," *Nature materials*, vol. 4, no. 2, pp. 138–142, 2005.

[18] D. V. Talapin and C. B. Murray, "PbSe nanocrystal solids for n- and p-channel thin film field-effect transistors," *Science*, vol. 310, no. 5745, pp. 86–89, 2005.

[19] J. Kwak, W. K. Bae, M. Zorn, H. Woo, H. Yoon, J. Lim, S. W. Kang, S. Weber, H.-J. Butt, R. Zentel, S. Lee, K. Char, and C. Lee, "Characterization of quantum dot/conducting polymer hybrid films and their application to light-emitting diodes," *Advanced Materials*, vol. 21, no. 48, pp. 5022–5026, 2009.

[20] W. K. Bae, J. Kwak, J. Lim, D. Lee, M. K. Nam, K. Char, C. Lee, and S. Lee, "Multicolored light-emitting diodes based on all-quantum-dot multilayer films using layer-by-layer assembly method," *Nano Letters*, vol. 10, no. 7, pp. 2368–2373, 2010.

[21] M. Zorn, W. K. Bae, J. Kwak, H. Lee, C. Lee, R. Zentel, and K. Char, "Quantum dot–block copolymer hybrids with improved properties and their application to quantum dot light-emitting devices," *ACS Nano*, vol. 3, no. 5, pp. 1063–1068, 2009. PMID: 19845366.

[22] I. J. Kramer and E. H. Sargent, "Colloidal quantum dot photovoltaics: A path forward," *ACS Nano*, vol. 5, no. 11, pp. 8506–8514, 2011.

[23] G. Konstantatos and E. Sargent, "Nanostructured materials for photon detection," *Nature nanotechnology*, vol. 5, no. 6, pp. 391–400, 2010.

[24] R. Meerheim, B. Lussem, and K. Leo, "Efficiency and stability of p-i-n type organic light emitting diodes for display and lighting applications," *Proceedings of the IEEE*, vol. 97, pp. 1606–1626, Sept.. 2009.

[25] M. Punke, S. Valouch, S. Kettlitz, M. Gerken, and U. Lemmer, "Optical data link employing organic light-emitting diodes and organic photodiodes as opto-electronic components," *Journal of Lightwave Technology*, vol. 26, pp. 816–823, Apr. 2008.

[26] T. N. Ng, W. S. Wong, M. L. Chabinyc, S. Sambandan, and R. A. Street, "Flexible image sensor array with bulk heterojunction organic photodiode," *Applied Physics Letters*, vol. 92, May 26 2008.

[27] S. Gunes, H. Neugebauer, and N. Sariciftci, "Conjugated polymer-based organic solar cells," *Chemical Reviews-Columbus*, vol. 107, no. 4, pp. 1324–1338, 2007.

[28] D. Wöhrle and D. Meissner, "Organic solar cells," *Advanced Materials*, vol. 3, no. 3, pp. 129–138, 1991.

[29] C. J. Brabec, N. S. Sariciftci, J. C. Hummelen, *et al.*, "Plastic solar cells," *Advanced Functional Materials*, vol. 11, no. 1, pp. 15–26, 2001.

[30] M. Binda, D. Natali, M. Sampietro, T. Agostinelli, and L. Beverina, "Organic based photodetectors: Suitability for x-and γ-rays sensing application," *Nuclear Instruments and Methods in Physics Research Section A: Accelerators, Spectrometers, Detectors and Associated Equipment*, vol. 624, no. 2, pp. 443–448, 2010.

[31] R. D. Schaller and V. I. Klimov, "High efficiency carrier multiplication in PbSe nanocrystals: Implications for solar energy conversion," *Physical Review Letters*, vol. 92, p. 186601, May 2004.

[32] V. I. Klimov, "Mechanisms for photogeneration and recombination of multiexcitons in semiconductor nanocrystals: Implications for lasing and solar energy conversion," *The Journal of Physical Chemistry B*, vol. 110, pp. 16827–45, Aug 2006.

[33] V. I. Klimov, *Nanocrystal quantum dots*. Boca Raton: CRC Press, 2nd ed., 2010.

[34] M. Bawendi, M. Steigerwald, and L. Brus, "The quantum mechanics of larger semiconductor clusters ("quantum dots")," *Annual Review of Physical Chemistry*, vol. 41, no. 1, pp. 477–496, 1990.

[35] S. V. Gaponenko, *Optical Properties of Semiconductor Nanocrystals*. Cambridge Studies in Modern Optics, Cambridge University Press, 1998.

[36] D. J. Griffiths, *Introduction to Qauntum Mechanics*. Pearson Prentice Hall, 2nd ed. ed., 2005.

[37] Y. Nosaka, "Finite depth spherical well model for excited states of ultrasmall semiconductor particles: An application," *The Journal of Physical Chemistry*, vol. 95, no. 13, pp. 5054–5058, 1991.

[38] D. B. T. Thoai, Y. Z. Hu, and S. W. Koch, "Influence of the confinement potential on the electron-hole-pair states in semiconductor microcrystallites," *Physical Review B*, vol. 42, pp. 11261–11266, Dec 1990.

[39] C. Kittel, *Introduction to solid state physics*. Hoboken, NJ: Wiley, 8th ed ed., 2005.

[40] L. Brus, "Electronic wave functions in semiconductor clusters: Experiment and theory," *The Journal of Physical Chemistry*, vol. 90, no. 12, pp. 2555–2560, 1986.

[41] H. Schmidt and H. Weller, "Quantum size effects in semiconductor crystallites: Calculation of the energy spectrum for the confined exciton," *Chemical Physics Letters*, vol. 129, no. 6, pp. 615–618, 1986.

[42] Y. Kayanuma, "Wannier exciton in microcrystals," *Solid State Communications*, vol. 59, no. 6, pp. 405–408, 1986.

[43] W. W. Yu, L. Qu, W. Guo, and X. Peng, "Experimental determination of the extinction coefficient of CdTe, CdSe, and CdS nanocrystals," *Chemistry of Materials*, vol. 15, no. 14, pp. 2854–2860, 2003.

[44] J. E. Murphy, M. C. Beard, A. G. Norman, S. P. Ahrenkiel, J. C. Johnson, P. Yu, O. I. Mićić, R. J. Ellingson, and A. J. Nozik, "PbTe colloidal nanocrystals: synthesis, characterization, and multiple exciton generation," *Journal of the American Chemical Society*, vol. 128, no. 10, pp. 3241–3247, 2006. PMID: 16522105.

[45] Q. Dai, Y. Wang, X. Li, Y. Zhang, D. J. Pellegrino, M. Zhao, B. Zou, J. Seo, Y. Wang, and W. W. Yu, "Size-dependent composition and molar extinction coefficient of PbSe semiconductor nanocrystals," *ACS Nano*, vol. 3, no. 6, pp. 1518–1524, 2009. PMID: 19435305.

[46] MIT Bawendi Group Homepage, http://nanocluster.mit.edu/research.php.

[47] S. Nomura and T. Kobayashi, "Nonparabolicity of the conduction band in CdSe and CdS_xSe_{1-x} semiconductor microcrystallites," *Solid State Communications*, vol. 78, no. 8, pp. 677–680, 1991.

[48] M. V. R. Krishna and R. A. Friesner, "Quantum confinement effects in semiconductor clusters," *The Journal of Chemical Physics*, vol. 95, no. 11, pp. 8309–8322, 1991.

[49] W. Shockley and H. J. Queisser, "Detailed balance limit of efficiency of p-n junction solar cells," *Journal of Applied Physics*, vol. 32, no. 3, pp. 510–519, 1961.

[50] A. J. Nozik, "Spectroscopy and hot electron relaxation dynamics in semiconductor quantum wells and quantum dots," *Annual Review of Physical Chemistry*, vol. 52, pp. 193–231, 2001.

[51] R. D. Schaller, J. M. Pietryga, S. V. Goupalov, M. A. Petruska, S. A. Ivanov, and V. I. Klimov, "Breaking the phonon bottleneck in semiconductor nanocrystals via multiphonon emission induced by intrinsic nonadiabatic interactions," *Physical Review Letters*, vol. 95, p. 196401, Nov 2005.

[52] J. A. McGuire, J. Joo, J. M. Pietryga, R. D. Schaller, and V. I. Klimov, "New aspects of carrier multiplication in semiconductor nanocrystals," *Accounts of Chemical Research*, vol. 41, pp. 1810–9, Dec 2008.

[53] R. D. Schaller, J. M. Pietryga, and V. I. Klimov, "Carrier multiplication in InAs nanocrystal quantum dots with an onset defined by the energy conservation limit," *Nano Letters*, vol. 7, no. 11, pp. 3469–3476, 2007.

[54] A. Shabaev, A. L. Efros, and A. J. Nozik, "Multiexciton generation by a single photon in nanocrystals," *Nano Letters*, vol. 6, no. 12, pp. 2856–2863, 2006.

[55] M. C. Beard, K. P. Knutsen, P. Yu, J. M. Luther, Q. Song, W. K. Metzger, R. J. Ellingson, and A. J. Nozik, "Multiple exciton generation in colloidal silicon nanocrystals," *Nano Letters*, vol. 7, no. 8, pp. 2506–2512, 2007.

[56] R. D. Schaller, M. Sykora, J. M. Pietryga, and V. I. Klimov, "Seven excitons at a cost of one: Redefining the limits for conversion efficiency of photons into charge carriers," *Nano Letters*, vol. 6, pp. 424–9, Mar 2006.

[57] G. Nair, S. M. Geyer, L.-Y. Chang, and M. G. Bawendi, "Carrier multiplication yields in PbS and PbSe nanocrystals measured by transient photoluminescence," *Physical Review B*, vol. 78, p. 125325, Sep 2008.

[58] G. Nair and M. G. Bawendi, "Carrier multiplication yields of CdSe and CdTe nanocrystals by transient photoluminescence spectroscopy," *Physical Review B*, vol. 76, p. 081304, Aug 2007.

[59] J. A. McGuire, M. Sykora, J. Joo, J. M. Pietryga, and V. I. Klimov, "Apparent versus true carrier multiplication yields in semiconductor nanocrystals," *Nano Letters*, vol. 10, no. 6, pp. 2049–2057, 2010. PMID: 20459066.

[60] M. Ben-Lulu, D. Mocatta, M. Bonn, U. Banin, and S. Ruhman, "On the absence of detectable carrier multiplication in a transient absorption study of InAs/CdSe/ZnSe core/shell1/shell2 quantum dots," *Nano Letters*, vol. 8, no. 4, pp. 1207–1211, 2008. PMID: 18341299.

[61] J. T. Stewart, L. A. Padilha, M. M. Qazilbash, J. M. Pietryga, A. G. Midgett, J. M. Luther, M. C. Beard, A. J. Nozik, and V. I. Klimov, "Comparison of carrier multiplication yields in PbS and PbSe nanocrystals: The role of competing energy-loss processes," *Nano Letters*, vol. 12, no. 2, pp. 622–628, 2012.

[62] F. W. Wise, "Lead salt quantum dots: the limit of strong quantum confinement," *Accounts of Chemical Research*, vol. 33, no. 11, pp. 773–780, 2000. PMID: 11087314.

[63] R. Weissleder, "A clearer vision for in vivo imaging," *Nature Biotechnology*, vol. 19, pp. 316–7, Apr. 2001.

[64] I. Medintz, H. Uyeda, E. Goldman, and H. Mattoussi, "Quantum dot bioconjugates for imaging, labelling and sensing," *Nature materials*, vol. 4, no. 6, pp. 435–446, 2005.

[65] F. Gao, L. W. Campbell, R. Devanathan, Y. Xie, L. R. Corrales, A. J. Peurrung, and W. J. Weber, "Monte Carlo method for simulating γ-ray interaction with materials: A case study on Si," *Nuclear Instruments and Methods in Physics Research Section A: Accelerators, Spectrometers, Detectors and Associated Equipment*, vol. 579, no. 1, pp. 292–296, 2007. Proceedings of the 11th Symposium on Radiation Measurements and Applications.

[66] F. Scholze, H. Rabus, and G. Ulm, "Mean energy required to produce an electron-hole pair in silicon for photons of energies between 50 and 1500 ev," *Journal of applied physics*, vol. 84, no. 5, pp. 2926–2939, 1998.

[67] A. Owens and A. Peacock, "Compound semiconductor radiation detectors," *Nuclear Instruments and Methods in Physics Research Section A: Accelerators, Spectrometers, Detectors and Associated Equipment*, vol. 531, no. 1–2, pp. 18–37, 2004. Proceedings of the 5th International Workshop on Radiation Imaging Detectors.

[68] M. Hammig, D. Wehe, and J. Nees, "The measurement of sub-brownian lever deflections," *Nuclear Science, IEEE Transactions on*, vol. 52, no. 6, pp. 3005–3011, 2005.

[69] X-5 Monte Carlo Team, *Los Alamos National Laboratory Report LA-UR-03-1987*. Los Alamos National Laboratory, 2003.

[70] G. F. Knoll, *Radiation Detection and Measurement*. John Wiley & Sons, Inc., 4th ed. ed., 2010.

[71] J. F. Ziegler, J. P. Biersack, and M. D. Ziegler, *SRIM – The Stopping and Range of Ions in Matter*. Ion Implantation Press, 2008.

[72] J. Sempau, E. Acosta, J. Baro, J. Fernandez-Varea, and F. Salvat, "An algorithm for Monte Carlo simulation of coupled electron-photon transport," *Nuclear Instruments and Methods in Physics Research Section B: Beam Interactions with Materials and Atoms*, vol. 132, no. 3, pp. 377 – 390, 1997.

[73] F. Remacle, K. C. Beverly, J. R. Heath, and R. D. Levine, "Conductivity of 2-d ag quantum dot arrays: computational study of the role of size and packing disorder at low temperatures," *The Journal of Physical Chemistry B*, vol. 106, no. 16, pp. 4116–4126, 2002.

[74] D. Bimberg, M. Grundmann, and N. Ledentsov, "Growth, spectroscopy, and laser application of self-ordered III-V quantum dots," *MRS Bulletin*, vol. 23, pp. 31–34, Feb. 1998.

[75] P. Petroff and G. MedeirosRibeiro, "Three-dimensional carrier confinement in strain-induced self-assembled quantum dots," *MRS Bulletin*, vol. 21, pp. 50–54, Apr. 1996.

[76] A. D. Yoffe, "Semiconductor quantum dots and related systems: Electronic, optical, luminescence and related properties of low dimensional systems," *Advances in Physics*, vol. 50, no. 1, pp. 1–208, 2001.

[77] J. Hu, T. W. Odom, and C. M. Lieber, "Chemistry and physics in one dimension: synthesis and properties of nanowires and nanotubes," *Accounts of Chemical Research*, vol. 32, no. 5, pp. 435–445, 1999.

[78] L. Lauhon, M. Gudiksen, D. Wang, C. Lieber, *et al.*, "Epitaxial core-shell and core-multishell nanowire heterostructures," *Nature*, vol. 420, no. 6911, pp. 57–61, 2002.

[79] C. B. Murray, S. Sun, W. Gaschler, H. Doyle, T. A. Betley, and C. R. Kagan, "Colloidal synthesis of nanocrystals and nanocrystal superlattices," *IBM Journal of Research and Development*, vol. 45, pp. 47–56, jan. 2001.

[80] C. Murray, C. Kagan, and M. Bawendi, "Synthesis and characterization of monodisperse nanocrystals and close-packed nanocrystal assemblies," *Annual Review of Materials Science*, vol. 30, pp. 545–610, 2000.

[81] V. K. LaMer and R. H. Dinegar, "Theory, production and mechanism of formation of monodispersed hydrosols," *Journal of the American Chemical Society*, vol. 72, no. 11, pp. 4847–4854, 1950.

[82] A. L. Rogach, L. Katsikas, A. Kornowski, D. Su, A. Eychmüller, and H. Weller, "Synthesis and characterization of thiol-stabilized CdTe nanocrystals," *Berichte der Bunsengesellschaft für physikalische Chemie*, vol. 100, no. 11, pp. 1772–1778, 1996.

[83] C. B. Murray, D. J. Norris, and M. G. Bawendi, "Synthesis and characterization of nearly monodisperse CdE (E = sulfur, selenium, tellurium) semiconductor nanocrystallites," *Journal of the American Chemical Society*, vol. 115, no. 19, pp. 8706–8715, 1993.

[84] M. Hines and G. Scholes, "Colloidal PbS nanocrystals with size-tunable near-infrared emission: Observation of post-synthesis self-narrowing of the particle size distribution," *Advanced Materials*, vol. 15, no. 21, pp. 1844–1849, 2003.

[85] N. Gaponik, D. V. Talapin, A. L. Rogach, K. Hoppe, E. V. Shevchenko, A. Kornowski, A. Eychmüller, and H. Weller, "Thiol-capping of CdTe nanocrystals: an alternative to organometallic synthetic routes," *The Journal of Physical Chemistry B*, vol. 106, no. 29, pp. 7177–7185, 2002.

[86] M. Gao, S. Kirstein, H. Möhwald, A. L. Rogach, A. Kornowski, A. Eychmüller, and H. Weller, "Strongly photoluminescent CdTe nanocrystals by proper surface modification," *The Journal of Physical Chemistry B*, vol. 102, no. 43, pp. 8360–8363, 1998.

[87] A. L. Rogach, "Nanocrystalline CdTe and CdTe(S) particles: Wet chemical preparation, size-dependent optical properties and perspectives of optoelectronic applications," *Materials Science and Engineering: B*, vol. 69â"70, no. 0, pp. 435–440, 2000.

[88] A. L. Rogach, N. A. Kotov, D. S. Koktysh, A. S. Susha, and F. Caruso, "II–VI semiconductor nanocrystals in thin films and colloidal crystals," *Colloids and Surfaces A: Physicochemical and Engineering Aspects*, vol. 202, no. 2–3, pp. 135–144, 2002.

[89] B.-S. Kong, J. Geng, and H.-T. Jung, "Layer-by-layer assembly of graphene and gold nanoparticles by vacuum filtration and spontaneous reduction of gold ions," *Chemical Communications*, pp. 2174–2176, 2009.

[90] Y. Zhu, S. Murali, W. Cai, X. Li, J. Suk, J. Potts, and R. Ruoff, "Graphene and graphene oxide: Synthesis, properties, and applications," *Advanced materials*, vol. 22, no. 35, pp. 3906–3924, 2010.

[91] A. Cola and I. Farella, "The polarization mechanism in CdTe schottky detectors," *Applied Physics Letters*, vol. 94, no. 10, p. 102113, 2009.

[92] K. Okada, Y. Sakurai, and H. Suematsu, "Characteristics of both carriers with polarization in diode-type CdTe x-ray detectors," *Applied Physics Letters*, vol. 90, no. 6, p. 063504, 2007.

[93] H. Toyama, A. Higa, M. Yamazato, T. Maehama, R. Ohno, and M. Toguchi, "Quantitative analysis of polarization phenomena in CdTe radiation detectors," *Japanese Journal of Applied Physics*, vol. 45, no. 11, pp. 8842–8847, 2006.

[94] Z. Tang, N. A. Kotov, and M. Giersig, "Spontaneous organization of single CdTe nanoparticles into luminescent nanowires," *Science*, vol. 297, no. 5579, pp. 237–240, 2002.

[95] A. J. Houtepen, R. Koole, D. Vanmaekelbergh, J. Meeldijk, and S. G. Hickey, "The hidden role of acetate in the PbSe nanocrystal synthesis," *Journal of the American Chemical Society*, vol. 128, no. 21, pp. 6792–6793, 2006. PMID: 16719451.

[96] J. Joo, J. M. Pietryga, J. A. McGuire, S.-H. Jeon, D. J. Williams, H.-L. Wang, and V. I. Klimov, "A reduction pathway in the synthesis of PbSe nanocrystal quantum dots," *Journal of the American Chemical Society*, vol. 131, no. 30, pp. 10620–10628, 2009. PMID: 19569687.

[97] Q. Dai, Y. Wang, Y. Zhang, X. Li, R. Li, B. Zou, J. Seo, Y. Wang, M. Liu, and W. W. Yu, "Stability study of PbSe semiconductor nanocrystals over concentration, size, atmosphere, and light exposure," *Langmuir*, vol. 25, no. 20, pp. 12320–12324, 2009. PMID: 19522486.

[98] M. Sykora, A. Y. Koposov, J. A. McGuire, R. K. Schulze, O. Tretiak, J. M. Pietryga, and V. I. Klimov, "Effect of air exposure on surface properties, electronic structure, and carrier relaxation in PbSe nanocrystals," *ACS Nano*, vol. 4, no. 4, pp. 2021–2034, 2010. PMID: 20369900.

[99] S. A. Pozzi, E. Padovani, and M. Marseguerra, "MCNP-PoliMi: A Monte-Carlo code for correlation measurements," *Nuclear Instruments and Methods in Physics Research Section A: Accelerators, Spectrometers, Detectors and Associated Equipment*, vol. 513, no. 3, pp. 550–558, 2003.

[100] D. B. Williams and C. B. Carter, *Transmission Electron Microscopy*. Springer, 2nd ed., 2009.

[101] M. Law, J. M. Luther, Q. Song, B. K. Hughes, C. L. Perkins, and A. J. Nozik, "Structural, optical, and electrical properties of PbSe nanocrystal solids treated thermally or with simple amines," *Journal of the American Chemical Society*, vol. 130, no. 18, pp. 5974–5985, 2008. PMID: 18396872.

[102] J. M. Luther, M. Law, Q. Song, C. L. Perkins, M. C. Beard, and A. J. Nozik, "Structural, optical, and electrical properties of self-assembled films of PbSe nanocrystals treated with 1,2-ethanedithiol," *ACS Nano*, vol. 2, no. 2, pp. 271–280, 2008.

[103] J. J. Choi, J. Luria, B.-R. Hyun, A. C. Bartnik, L. Sun, Y.-F. Lim, J. A. Marohn, F. W. Wise, and T. Hanrath, "Photogenerated exciton dissociation in highly coupled lead salt nanocrystal assemblies," *Nano Letters*, vol. 10, no. 5, pp. 1805–1811, 2010.

[104] T. P. Osedach, N. Zhao, T. L. Andrew, P. R. Brown, D. D. Wanger, D. B. Strasfeld, L.-Y. Chang, M. G. Bawendi, and V. Bulović, "Bias-stress effect in 1,2-ethanedithiol-treated PbS quantum dot field-effect transistors," *ACS Nano*, vol. 6, no. 4, pp. 3121–3127, 2012.

[105] C.-Y. Kuo, M.-S. Su, C.-S. Ku, S.-M. Wang, H.-Y. Lee, and K.-H. Wei, "Ligands affect the crystal structure and photovoltaic performance of thin films of PbSe quantum dots," *Journal of Materials Chemistry*, vol. 21, pp. 11605–11612, 2011.

[106] F. A. Boroumand, P. W. Fry, and D. G. Lidzey, "Nanoscale conjugated-polymer light-emitting diodes," *Nano Letters*, vol. 5, no. 1, pp. 67–71, 2005.

[107] P. T. K. Chin, R. A. M. Hikmet, and R. A. J. Janssen, "Energy transfer in hybrid quantum dot light-emitting diodes," *Journal of Applied Physics*, vol. 104, no. 1, p. 013108, 2008.

[108] S. Coe, W. Woo, and V. Moungi Bawendi, "Electroluminescence from single monolayers of nanocrystals in molecular organic devices," *Nature*, vol. 420, no. 6917, pp. 800–803, 2002.

[109] T. A. Skotheim, ed., *Handbook of Conducting Polymers*. New York: Marcel Dekker Inc., 2 ed., 1998.

[110] S. Gilliland, J. González, H. S. Güder, A. Segura, I. Mora, and V. Muñoz, "Pressure and temperature dependence of the band-gap in CdTe," *physica status solidi (b)*, vol. 235, no. 2, pp. 441–445, 2003.

[111] A. H. Nethercot, "Prediction of fermi energies and photoelectric thresholds based on electronegativity concepts," *Phys. Rev. Lett.*, vol. 33, pp. 1088–1091, Oct 1974.

[112] D. S. Shang, Q. Wang, L. D. Chen, R. Dong, X. M. Li, and W. Q. Zhang, "Effect of carrier trapping on the hysteretic current-voltage characteristics in $Ag/La_{0.7}Ca_{0.3}MnO_3/Pt$ heterostructures," *Physical Review B*, vol. 73, p. 245427, Jun 2006.

[113] M. Egginger, S. Bauer, R. Schwödiauer, H. Neugebauer, and N. Sariciftci, "Current versus gate voltage hysteresis in organic field effect transistors," *Monatshefte für Chemie/Chemical Monthly*, vol. 140, no. 7, pp. 735–750, 2009.

[114] H.-C. Lin, C.-H. Hung, W.-C. Chen, Z.-M. Lin, H.-H. Hsu, and T.-Y. Hunag, "Origin of hysteresis in current-voltage characteristics of polycrystalline silicon thin-film transistors," *Journal of Applied Physics*, vol. 105, no. 5, p. 054502, 2009.

[115] M. Jeong, M. D. Hammig, and S. Ramadoss, "Optimizing the snr from a radiation detector with delay-line position-sensing electrodes," *Nuclear Instruments*

and Methods in Physics Research Section A: Accelerators, Spectrometers, Detectors and Associated Equipment, vol. 652, no. 1, pp. 427–434, 2011. Symposium on Radiation Measurements and Applications (SORMA) XII 2010.

[116] F. Zhang, C. Herman, Z. He, G. De Geronimo, E. Vernon, and J. Fried, "Characterization of the H3D ASIC readout system and 6.0 cm 3-D position sensitive CdZnTe detectors," *Nuclear Science, IEEE Transactions on*, vol. 59, pp. 236–242, feb. 2012.

[117] G. Konstantatos, L. Levina, J. Tang, and E. H. Sargent, "Sensitive solution-processed Bi_2S_3 nanocrystalline photodetectors," *Nano Letters*, vol. 8, no. 11, pp. 4002–4006, 2008. PMID: 18844425.

[118] A. K. Rath, M. Bernechea, L. Martinez, and G. Konstantatos, "Solution-processed heterojunction solar cells based on p-type PbS quantum dots and n-type Bi_2S_3 nanocrystals," *Advanced Materials*, vol. 23, no. 32, pp. 3712–3717, 2011.

[119] M. Hammig, T. Kang, and M. Jeong, "Suppression of interface-induced noise by control of the phonon-leaking characteristics of the contacts," *Nuclear Science, IEEE Transactions on*, Dec 2012 (Accepted).

[120] P. Luke, "Single-polarity charge sensing in ionization detectors using coplanar electrodes," *Applied Physics Letters*, vol. 65, no. 22, pp. 2884–2886, 1994.

[121] A. Kargar, A. Jones, W. McNeil, M. Harrison, and D. McGregor, "CdZnTe frisch collar detectors for γ-ray spectroscopy," *Nuclear Instruments and Methods in Physics Research Section A: Accelerators, Spectrometers, Detectors and Associated Equipment*, vol. 558, no. 2, pp. 497–503, 2006.